Università degli Studi di Modena e Reggio Emilia

Facoltà di Scienze Matematiche Fisiche e Naturali

Corso di Laurea Magistrale in Fisica

PRELIMINARY STUDY FOR A MEASUREMENT OF THE CKM ANGLE γ USING THE TREE $B^{\pm} \to D^{(*)0}K^{\pm}$ DECAYS WITH THE LHCb DETECTOR AT CERN

Analisi preliminari per la misura dell'angolo γ del meccanismo CKM dai decadimenti $B^{\pm} \to D^{(*)0}K^{\pm}$ con il rivelatore LHCb al CERN

The work has begun with a training period at LAPP (Laboratoire d'Annecy le Vieux de Physique des Particule) with the supervision of Vincent Tisserand

Relatore:
Prof. Andrea Bizzeti

Laureando:
Lucio Anderlini

Anno Accademico 2010/11

Secondo mio avviso si ha a distinguere primieramente queste cose:
che è quello che sempre è, e non ha generazione;
e che è quello che sempre si genera, e mai non è?

L'uno, è ciò che si comprende per intelletto e ragione,
siccome quello che è eternamente a un modo;
l'altro, per lo contrario, è ciò ch'è opinabile per opinione ed irrazionale senso,
generandosi esso e perendo sí, che mai non è veramente.

Tutto quello poi che si genera,
è necessità che generato sia da alcuna cagione;
senza quella non potendo cosa alcuna venire a generazione.
E quando l'artefice di qualsivoglia opera vagheggia quello che è medesimo eternalmente,
e giovandosene cosí come di esempio, l'idea e virtú di quello reca ad atto,
necessità è che faccia cosa bellissima;

per lo contrario, non bella, se in alcuna
generata cosa egli guarda, e di generato esempio si giova.

[...]

Se dunque, Socrate,
dopo le molte cose dette da molti intorno agl'Iddii e alla generazione dell'Universo,
non possiamo noi offerirti ragionamenti squisiti e concordi in ogni parte seco medesimi,
non ti maravigliare;

e se i miei non sono men verosimili che quelli di qualunque altro, sta' pure contento;
ricordandoti, che io che parlo, e voi, giudici miei, abbiamo umana natura;
in modo che su questo argomento ricevendo verosimili novelle, piú non conviene dimandare.

Timeo, Platone. 2350 anni fa.

First then, in my judgment, we must make a distinction and ask,
What is that which always is and has no becoming; and what is that which is always becoming and never is?

That which is apprehended by intelligence and reason,
since it is always in the same state;
but that which is conceived by opinion with the help of sensation and without reason,
is always in a process of becoming and perishing and never really is.

Now everything that becomes or is created must of necessity be created by some cause,
for without a cause nothing can be created.
The work of the artificer, whenever he looks to the unchangeable
and fashions the form and nature of his work after an unchangeable pattern,
must necessarily be made fair and perfect;

but when he looks to the created only, and uses a created pattern,
it is not fair or perfect.

[...]

If then, Socrates,
amid the many opinions about the gods and the generation of the universe,
we are not able to give notions which are altogether and in every respect exact and self consistent, do not be surprised.

Enough, if we adduce probabilities as likely as any others;
for we must remember that I who am the speaker, and you who are the judges, are only mortal men,
and we ought to accept the tale which is plausible and enquire no further.

Timaeus, Plato. 2350 years ago.

A Fabio e Biagio.

Contents

Abstract

The Large Hadron Collider (LHC) offers the possibility to collect hints of New Physics (NP) in proton-proton collisions at high energy. The LHC experiments' collaborations are exploring direct and indirect techniques to reveal the existence of NP. General purpose detectors, as ATLAS and CMS, search for the decay of predicted particles to complete the Standard Model or its extensions. ALICE is dedicated to sudies of a high density and high temperature environment, testing the theoretical predictions for quark gluon plasma state. LHCb tests the Standard Model (SM) in the sector of the Heavy Flavors and the global consistency of the description of the CP violation (CPV) phenomena. Since CPV manifestations involve in particular beauty mesons and because of the large $b\bar{b}$ production cross section at LHC, LHCb is already starting to contribute to world averages for B-meson physics and CPV parameters.

The measurement of the γ angle of the *bd* unitarity triangle of the Cabibbo-Kobayashi-Maskawa (CKM) matrix [1, 2] is a key test of the Standard Model (SM), as γ approximates the complex phase δ of the CKM matrix explaining CP violation within the quark sector of the SM. The measurement of the γ angle can be achieved through theoretically clean tree-only processes $B^{\pm} \to D^{(*)0}K^{\pm}$ [3], excluding any contribution from NP. A precise measurement of γ with tree transitions would set a very stable reference for the global consistency test of the CKM mechanism within the SM. A discrepancy between the measurement of γ achieved through tree-only decays and through processes involving loops would be evidence of NP virtual particles arising in the loops. Furthermore the world average for γ is less precise than that of the other angles of unitarity triangle (α and β). The test of the geometrical relation $\alpha + \beta + \gamma = \pi$ is a fundamental test for the three-generation quark model. The work presented here is a feasibility study for contributing to tree-processes γ measurement with the channel $B \to D^{*0}K$. The methods exploiting this decay are called GLW [4] and ADS [5] after the authors Gronau-London-Wyler and Awood-Dunietz-Soni, respectively. I conclude the theoretical introduction by reviewing the GLW and ADS methods for the $B^{\pm} \to D^0K^{\pm}$ channel and their extension to $B^{\pm} \to D^{*0}K^{\pm}$.

The LHC offers the world highest $b\bar{b}$-pairs production cross section, while the LHCb detector has been designed to efficiently measure B-mesons, achieving a high background rejection thanks to a powerful multi-level trigger.

The comparison of LHCb, TeVatron (CDF) and b-factories (BaBar and Belle) yields shows that the LHCb data sample is already competitive, and LHCb is expected to obtain the best γ measurement, based on 1 fb^{-1} (2 fb^{-1}) collected at the end of 2011 (2012). I describe the official LHCb analysis of $B^{\pm} \to D^0K^{\pm}$ decays that I have repeated during my training period, as well as the computing techniques used.

Finally I describe the first reconstruction attempts for $B^{\pm} \to D^{*0}h^{\pm}$ channels. The aim is to verify whether $B^{\pm} \to D^{*0}K^{\pm}$ channel can significantly improve LHCb γ measurement, contributing with a significant data sample. I have thus applied the same techniques used for the $B^{\pm} \to D^0h^{\pm}$ analyses to the $B^{\pm} \to D^{*0}\pi^{\pm}$, developing a C++ framework named *Leaf* which is parallel calculation oriented and usable for both analyses. Using *Leaf* and some additional utilities (as RooFit and *T*MVA), I achieved the first observation of $B^{\pm} \to D^{*0}\pi^{\pm} \to (D^0\gamma)\pi^{\pm}$ and $B^{\pm} \to D^{*0}\pi^{\pm} \to (D^0\pi^0)\pi^{\pm}$ at LHCb, with a statistical significance of 4.2 and 7.9 σ, respectively. As the current efficiencies are not sufficient to measure γ through D^{*0} channels, this result encourages to improve the reconstruction algorithms (of low energy photons) in order to increase the efficiency.

Capitolo 1

Riassunto in lingua italiana

1.1 Elementi di teoria e definizioni preliminari

1.1.1 Simmetrie discrete nel Modello Standard

In fisica, ed in particolare in teoria quantistica dei campi, il concetto di simmetria assume grande rilevanza poiché è strettamente legato a leggi di conservazione. Esistono due tipi di simmetrie: le simmetrie continue e le simmetrie discrete. Gli operatori matematici che permettono di passare da uno stato ad un altro correlato da una data simmetria, sono definiti da uno o più parametri reali nel caso di simmetrie continue, o da un indice discreto nel caso dell'omonima classe di simmetrie.

Le simmetrie sono spesso chiamate invarianze. Sono esempi l'invarianza traslazionale o rotazionale. Il teorema di Emmy Nöether, nell'ambito della teoria quantistica dei campi, stabilisce che a ciascuna simmetria continua corrisponda una grandezza fisica conservata nel tempo.

Le simmetrie discrete, sulle quali focalizzeremo l'interesse da qui in poi, correlano stati quantistici tramite a un insieme discreto di operatori. Sono un esempio la parità P, che correla stati che hanno il segno della componente spaziale $\mathbf{x}$ del quadrivettore relativistico $X^\mu \equiv (ct, \boldsymbol{x})$ opposto, la simmetria di coniugazione di carica C che correla due stati di cui il secondo contiene le antiparticelle del primo, e la simmetria di inversione temporale T, che correla due stati con componente temporale t opposta.

Si dice che una simmetria è violata se la fisica dei due stati correlati da tale simmetria non è la medesima. Nel Modello Standard, la teoria quantistica dei campi che oggi descrive tutte le particelle e le interazioni (ad eccezione della gravitazionale) osservate sperimentalmente, le simmetrie P e C sono violate dall'interazione nucleare debole, poiché essa non interviene che per la componente a chiralità sinistra (destra) dei fermioni (anti-fermioni), la quale diventa componente a chiralità destra (sinistra) sotto simmetria P. La misura sperimentale della violazione della parità P nel celebre esperimento sul decadimento di nuclei di ^{60}Co polarizzati, fu pubblicata da C. S. Wu *et al.* [6] nel 1957.

Le simmetrie elementari descritte possono essere combinate tra loro per ottenere operazioni di simmetria più complesse. Combinando le tre simmetrie discrete si ottiene la cosiddetta simmetria CPT, la cui invarianza (non violazione) discende da ipotesi fondamentali delle teorie quantistiche dei campi. Sperimentalmente non si è mai osservata violazione di CPT.

La violazione della simmetria CP è invece stata osservata in diverse esperienze, la prima pubblicazione risale al 1964 quando J.H. Christenson *et al.* [7] misurarono un effetto di violazione di CP nel mescolamento di kaoni neutri. Nel 2001, *BABAR* e Belle hanno infine messo in evidenza la violazione di CP nei mesoni B [8, 9].

La violazione della simmetria d'inversione temporale T è stata indirettamente osservata dall'esperimento CP-Lear al CERN [10] come differenza nel tasso di transizioni $K^0 \to \overline{K}^0$ e $\overline{K}^0 \to K^0$.

1.1.2 Mescolamento dei quark e matrice CKM

Nel 1963 Nicola Cabibbo [1] propose la teoria del mescolamento dei quark per preservare l'universalità dell'interazione debole di corrente carica. Secondo il modello di mescolamento, il vertice d'interazione debole di corrente carica accoppia i quark di tipo *up* (a carica elettrica $\pm\frac{2}{3}e$, il segno sottostante riguarda l'anti-quark) ad una sovrapposizione di quark di tipo *down* (a carica elettrica $\mp\frac{1}{3}e$). All'epoca in cui Cabibbo introdusse il concetto di mescolamento, erano noti solamente tre quark: i quark *up* (u) e *down* (d), che costituiscono i nucleoni della materia stabile, e un terzo quark chiamato *strange (s)* a carica elettrica $\mp\frac{1}{3}e$. Pertanto, l'ipotesi di mescolamento consisteva nell'assumere un vertice $\overline{u}Wd'$ dove d' risulta una sovrapposizione degli stati a sapore definito d ed s mescolati secondo l'angolo di Cabibbo θ_C. In termini algebrci

$$\begin{cases} d' = d\cos\theta_C + s\sin\theta_C \\ s' = -d\sin\theta_C + s\cos\theta_C \end{cases} \tag{1.1}$$

Nel 1974 fu scoperto il quark *charm* c con la scoperta dello stato charmonium J/ψ, contemporaneamente, al laboratorio dell'acceleratore lineare di Standford (SLAC), e ai laboratori nazionali di Brookhaven (BNL). Il quark c completa la rappresentazione del meccanismo di Cabibbo permettendo di determinare le quattro costanti di vertice g_{ud}, g_{uc}, g_{ud} e g_{cs} a partire dai soli parametri g_W (costante di vertice dell'interazione debole nel settore leptonico) e θ_C.

Quando nel 1964 Christenson *et al.* [7] osservarono la violazione della simmetria CP per la prima volta, i fisici teorici iniziarono a cercare un'estensione alla teoria che potesse spiegare la violazione di CP. Così nel 1973 Kobayashi e Maskawa [2] osservarono che il meccanismo di mescolamento dei quark introdotto da Cabibbo poteva spiegare la violazione di CP a patto di introdurre una terza famiglia di quark, che presero il nome di quark *top* di carica elettrica $\pm\frac{2}{3}e$ e quark *bottom* di carica $\mp\frac{1}{3}e$.

La matrice di mescolamento tra le tre famiglie prende il nome di matrice CKM (Cabibbo - Kobayashi - Maskawa), e la violazione di CP proviene da una fase della matrice che cambia di segno sotto coniugazione di CP del lagrangiano che descrive l'interazione elettro-debole. Fu proprio l'osservazione che un tale fattore di fase complesso non sia possibile in una matrice di mescolamento 2×2 che spinse Kobayashi e Maskawa a introdurre la terza famiglia. La previsione dei due quark mancanti, osservati negli anni successivi, è stata riconosciuta ai due fisici giapponesi con l'assegnazione del premio Nobel nel 2008. Gli elementi della matrice CKM non sono previsti dalla teoria, bensì sono riconducibili a quattro parametri liberi del Modello Standard, come le masse dei fermioni o i parametri del potenziale di Higgs. Come per tutti i parametri liberi del Modello Standard, c'è chi ipotizza che essi siano in realtà fissati da una teoria più generale, che ancora non conosciamo, della quale il Modello Standard costituisce un modello efficace a bassa energia.

La relazione tra gli stati d', s' e b' e gli autostati di massa risulta dunque essere

$$D' = \begin{pmatrix} d' \\ s' \\ b' \end{pmatrix} = \begin{pmatrix} V_{ud} & V_{us} & V_{ub} \\ V_{cd} & V_{cs} & V_{cb} \\ V_{td} & V_{ts} & V_{tb} \end{pmatrix} \begin{pmatrix} d \\ s \\ b \end{pmatrix} = V_{\mathrm{CKM}}\ D \tag{1.2}$$

In qualità di matrice di mescolamento, la matrice V_{CKM} è unitaria. Il vincolo di unitarietà impone

$$V_{\mathrm{CKM}}^{\dagger} V_{\mathrm{CKM}} = V_{\mathrm{CKM}} V_{\mathrm{CKM}}^{\dagger} = \mathbf{1} \tag{1.3}$$

La relazione matriciale 1.3 può essere separata in nove equazioni scalari di cui tre impongono l'uguaglianza tra la somma di tre termini complessi e l'unità; e le restanti sei impongono l'uguaglianza tra un'analoga somma di tre termini complessi e zero. Queste equazioni prendono il nome di relazioni di unitarietà, e risultano di grande importanza nello studio degli effetti della violazione di CP poiché impongono vincoli importanti tra moduli e fasi degli elementi della matrice CKM. Tra le relazioni di unitarietà, per ragioni che discuterò in seguito, assume particolare rilevanza la cosiddetta relazione *bd*, poiché riguarda relazioni tra gli elementi della matrice CKM relativi ai quark b e d.

$$V_{ud}V_{ub}^{*} + V_{cd}V_{cb}^{*} + V_{td}V_{tb^{*}} = 0 \tag{1.4}$$

Se rappresentata nel piano complesso, la somma 1.4 risulta un triangolo, i cui lati sono costituiti da vettori che rappresentano i tre addendi. Se la relazione di unitarietà è rispettata, il triangolo si chiude poiché la somma dei tre contributi è zero. Una prova sperimentale che il triangolo non si chiude sarebbe un indizio a favore di teorie oltre il modello standard che prevedono una quarta famiglia di quark. In questo caso il triangolo sarebbe in realtà un quadrilatero con un quarto lato inatteso nel Modello Standard.

Il triangolo di unitarietà viene solitamente rappresentato normalizzando i tre lati a $V_{cd}V_{cb}^*$, di modo che uno dei tre lati giaccia sull'asse reale e si estenda da zero a uno. La rappresentazione del triangolo di unitarietà è presentata in figura 1.1. L'apice del triangolo viene indicato con i parametri $\overline{\rho}$ ed $\overline{\eta}$, mentre gli angoli sono indicati con le lettere greche α, β e γ in occidente, e come ϕ_1, ϕ_2 e ϕ_3 in Giappone.

Le molte misure effettuate sui diversi parametri del triangolo di unitarietà sono state raccolte in un fit globale dal gruppo CKM fitter, secondo un approccio frequentista, e dal gruppo UTFit secondo un approccio bayesiano. I risultati ottenuti dai due gruppi sono compatibili. I differenti vincoli sui parametri della matrice CKM sono rappresentati in figura 1.1, le regioni colorate sono ammesse al 95% di livello di confidenza dalla combinazione dei risultati di diversi esperimenti relativi a ciascuna singola misura.

I valori attualmente accettati per la misura diretta angoli della matrice CKM sono riportati di seguito [11]:

$$\alpha = \arg\left[-\frac{V_{td}V_{tb}^*}{V_{ud}V_{ub}^*}\right] = \left(89.0^{+4.4}_{-4.2}\right)^\circ \qquad \beta = \arg\left[-\frac{V_{cd}V_{cb}^*}{V_{td}V_{tb}^*}\right] = \left(21.15^{+0.90}_{-0.88}\right)^\circ$$

$$\gamma = \arg\left[-\frac{V_{ud}V_{ub}^*}{V_{cd}V_{cb}^*}\right] = \left(71^{+21}_{-25}\right)^\circ$$

È immediato osservare che la misura dell'angolo γ è la meno precisa. La regione al 95% di livello di confidenza per la posizione dell'apice del triangolo di unitarietà ottenuta dalla misura diretta dell'angolo γ copre circa la metà del piano complesso, apportando un'informazione pressoché nulla al fit globale.

Esiste un'altra ragione per la quale la misura dell'angolo γ risulta di grande interesse. Gli angoli α e β sono fasi che coinvolgono il lato $V_{td}V_{tb}^*$ del triangolo di unitarietà, relativo al quark top. Fino ad ora, misure che riguardano parametri relativi al quark top hanno sempre richiesto l'utilizzo di decadimenti tramite diagrammi a *loop*, nei quali il quark top appare in stati virtuali intermedi tra lo stato iniziale e lo stato finale secondo la teoria perturbativa tempo-dipendente. In particolare si sfrutta l'oscillazione dei mesoni B *neutri*, che viene descritta nel modello standard da diagrammi di Feynman *a scatola*. Dal momento che eventuali particelle di massa elevata non descritte dal Modello Standard (ma piuttosto dalla cosiddetta *Nuova Fisica*) apparirebbero in prima istanza come stati virtuali nei *loop*, la misura degli angoli α e β potrebbe essere leggermente falsata da contributi di Nuova Fisica. Per di più, oltre al *loop* nell'oscillazione dei mesoni B neutri, i processi utilizzati nella misura degli angoli α e β sono soggetti alla, così chiamata, *penguin-pollution*, ossia inquinamento da diagrammi a pinguino, una particolare classe di diagrammi di Feynman, contenenti *loop*. Al decadimento, e dunque ai valori misurati per gli angoli α e β, contribuiscono così, oltre ai processi descritti da diagrammi di Feynman ad albero, ossia diagrammi che non contengono *loop*, anche processi descritti da diagrammi a pinguino. Ancora una volta la presenza dei *loop* potrebbe includere nel risultato finale un contributo dovuto alla presenza di Nuova Fisica, tale che la misura ottenuta per α e β non corrisponda alle fasi α e β del modello CKM.

Contrariamente ai processi (oscillazione seguita da decadimento di mesoni B) utilizzati per la misura delle fasi α e β, i processi considerati per misurare l'angolo γ possono essere scelti tra quelli descritti esclusivamente da diagrammi ad albero, per i quali non possano insorgere dubbi di contribuzione da parte di Nuova Fisica. Per questa ragione l'angolo γ risulta un punto di riferimento essenziale del meccanismo CKM nel quadro del Modello Standard. La discrepanza tra la misura dell'angolo γ in processi descritti da soli diagrammi ad albero[1] e la misura di γ con diagrammi

[1] il contributo dei diagrammi a *loop* è presente ma di ordine superiore, e quindi trascurabile, rispetto a quello dovuto a diagrammi ad albero.

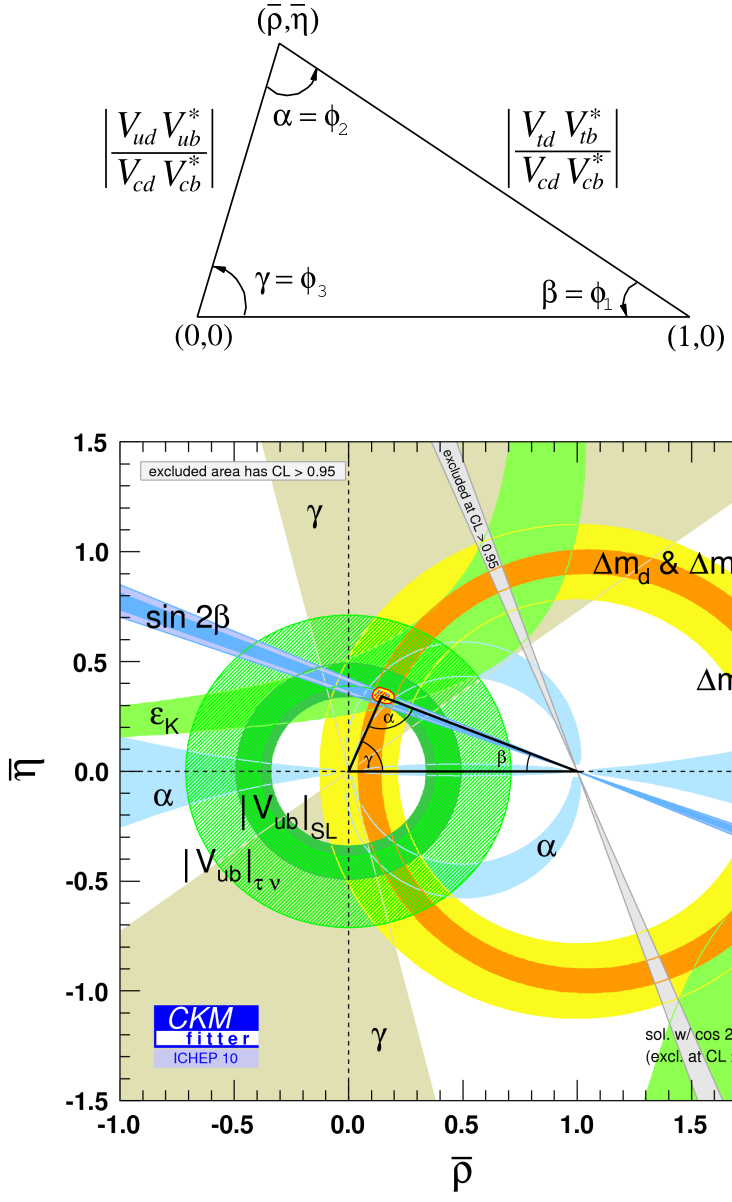

Figura 1.1: Rappresentazione del triangolo di unitarità nel piano complesso. Sotto, il triangolo di unitarietà è sovrapposto alla rappresentazione dei vincoli sperimentali sui parametri della matrice CKM raccolti da diverse esperienze e utilizzati dal gruppo CKM fitter per effettuare un fit globale. Le aree colorate rappresentano le regioni ammesse al 95 % di livello di confidenza secondo le diverse misure. Intorno all'apice del triangolo, l'area colorata rappresenta la regione al 95% di livello di confidenza secondo il fit globale.

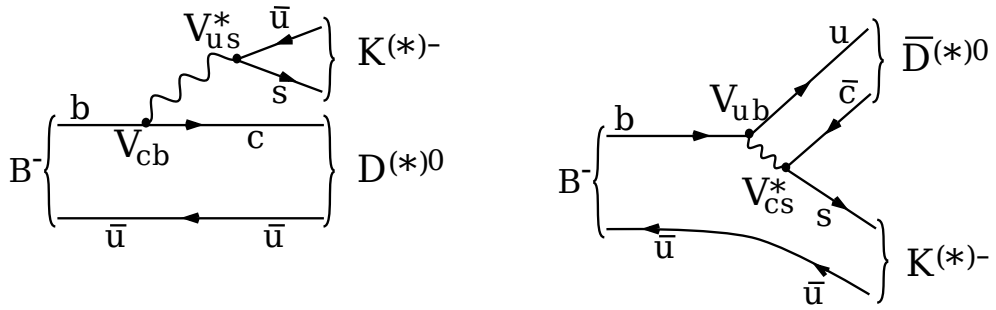

Figura 1.2: Diagrammi di Feynman dei decadimenti di mesoni B carichi utili alla misura dell'angolo γ. La differenza di fase tra le ampiezze corrispondenti ai due diagrammi, escludendo contributi dell'interazione forte nello stato finale, è in ottima approssimazione pari all'angolo γ. Il diagramma a sinistra è favorito rispetto a quello a destra di un fattore ~ 10.

contenenti *loop*, così come una violazione della relazione geometrica $\alpha + \beta + \gamma = \pi$, costituirebbero un indizio di Nuova Fisica, e rappresentano uno dei campi di maggiore interesse dell'odierna fisica dei sapori sperimentale.

1.2 Metodi sperimentali per la misura dell'angolo γ

Come anticipato esistono differenti metodi per la misura dell'angolo γ, utilizzando processi all'albero o altri contenenti *loop*. Questi ultimi sono oltre l'interesse di questa tesi.

La misura dell'angolo γ all'albero si basa sulla misura dell'interferenza tra due diagrammi di Feynman (figura 1.2) di ampiezza proporzionale agli elementi di matrice CKM coinvolti nella definizione dell'angolo γ. Per accedere alla fase degli elementi associati al quark b, si scelgono decadimenti di mesoni B. Laddove possibile, è sempre preferibile utilizzare mesoni B carichi per i quali distinguere mesoni di materia e antimateria è tanto semplice quanto distinguere mesoni di carica elettrica opposta, inoltre una misura effettuata con mesoni carichi non coinvolge il contributo dell'oscillazione dei mesoni. Questo tipo di violazione della simmetria CP, in assenza di oscillazione, prende il nome di *violazione di CP diretta* o nel decadimento e si osserva come una differenza nel tasso di decadimento tra mesoni CP coniugati (di carica opposta nel caso di mesoni carichi). Si distingue dalla *violazione di CP indiretta* o nel mescolamento, nella quale è l'evoluzione temporale (oscillazione) che modifica l'autostato di CP del mesone neutro. Esiste un terzo effetto di violazione di CP, che si manifesta nell'interferenza tra un decadimento avvenuto in assenza di oscillazione ed uno a seguito di un'oscillazione (*violazione di CP nell'interferenza*) .

Il rapporto tra le ampiezze dei diagrammi mostrati in figura 1.2 è indicato come r_B, mentre la *fase forte*, il contributo alla fase relativa tra le due ampiezze dovuto allo scambio di gluoni nello stato finale è indicato con δ_B; infine il contributo elettrodebole, con ottima approssimazione, è pari a γ. Mentre la fase forte resta costante sotto applicazione dell'operatore CP, la fase elettrodebole cambia di segno. È proprio questa differenza tra il decadimento di mesoni B^+ e B^- a generare gli effetti di violazione di CP. Riassumendo queste definizioni, si può scrivere

$$r_B = \left|\frac{\mathcal{A}(\text{soppresso})}{\mathcal{A}(\text{favorito})}\right| = (10.1 \pm 3.2)\% \qquad \arg\left[\mathcal{A}(\text{favorito})_{B^\pm}\right] \equiv 0 \quad \arg\left[\mathcal{A}(\text{soppresso})_{B^\pm}\right] = \delta_B \pm \gamma \tag{1.5}$$

Dove $\mathcal{A}$(favorito) rappresenta l'ampiezza di decadimento del diagramma con transizione $b \to c$, mentre $\mathcal{A}$(soppresso) è l'ampiezza del diagramma con transizione $b \to u$. Il valore di r_B sopra riportato è stato misurato con rivelatori precedenti ad LHCb: B-factories e CDF. Si può dimostrare che il segno della fase elettrodebole γ è positivo per il decadimento di mesoni B^+ e negativo per il decadimento di B^-.

Per misurare l'interferenza tra i due canali di decadimento, occorre scegliere un canale di decadimento comune per D^0 e $\overline{D}^0$. Con $\tilde{D}^0$ indicherò quella particolare sovrapposizione degli stati D^0 e $\bar{D}^0$ che decade nello stato finale, comune ai due, scelto. Le relazioni tra grandezze fisicamente

osservabili e i parametri r_B e δ_B, detti parametri di tedio (*nuisance* parameters), nonché con la fase elettrodebole γ, sono differenti a seconda del canale di decadimento comune scelto. Gli osservabili sperimentali sono il rapporto tra le larghezze di decadimento di mesoni B carichi attraverso stati $\tilde{D}^0$ e stati a sapore definito D^0 e $\overline{D}^0$.

$$\mathcal{R} = \frac{\Gamma(B^- \to \tilde{D}^0 K^-) + \Gamma(B^+ \to \tilde{D}^0 K^+)}{\Gamma(B^- \to D^0 K^-) + \Gamma(B^+ \to \overline{D}^0 K^+)} \tag{1.6}$$

L'asimmetria tra i decadimenti di mesoni B^+ e B^- è invece definita come

$$\mathcal{A} = \frac{\Gamma(B^- \to \tilde{D}^0 K^-) - \Gamma(B^+ \to \tilde{D}^0 K^+)}{\Gamma(B^- \to \tilde{D}^0 K^-) + \Gamma(B^+ \to \tilde{D}^0 K^+)} \tag{1.7}$$

I valori di questi osservabili dipendono dal processo di decadimento comune scelto che definisce lo stato $\tilde{D}^0$.

1.2.1 Metodo Gronau-London-Wyler (GLW)

Storicamente, il primo metodo per la misura dell'angolo γ fu introdotto da *Gronau, London* e *Wyler* [4] nel 1991. Il canale di decadimento comune scelto è il decadimento di un D^0 in un autostato di CP. I canali di decadimento considerati per ricostruire un D^0 in un autostato pari di CP sono $D^0_{CP+} \to K^+K^-$ oppure $D^0_{CP-} \to \pi^+\pi^-$. L'autostato di CP dispari viene ricostruito tramite il decadimento in un K^0_s e un altro mesone neutro. Ossia $D^0_{CP-} \to K^0_s\{\pi^0,\ \eta,\ \eta',\ \omega,\ \phi\}$.

La definizione del rapporto $\mathcal{R}$ viene leggermente modificata. Il rapporto GLW è definito come

$$\mathcal{R}_{CP\pm} = \frac{\Gamma(B^- \to D^0_{CP\pm} K^-) + \Gamma(B^+ \to D^0_{CP\pm} K^+)}{\frac{1}{2}\{\Gamma(B^- \to D^0 K^-) + \Gamma(B^+ \to \overline{D}^0 K^+)\}} \tag{1.8}$$

mentre l'asimetria GLW è definita secondo la definizione 1.7 come

$$\mathcal{A}_{CP\pm} = \frac{\Gamma(B^- \to D^0_{CP\pm} K^-) - \Gamma(B^+ \to D^0_{CP\pm} K^+)}{\Gamma(B^- \to D^0_{CP\pm} K^-) + \Gamma(B^+ \to D^0_{CP\pm} K^+)} \tag{1.9}$$

Non è difficile mostrare che le relazioni tra tali osservabili, γ e i parametri di tedio sono

$$\mathcal{A}_{\mathcal{CP}\pm} = \frac{\pm 2 r_B \sin\delta_B \sin\gamma}{1 + r_B^2 \pm 2 r_B \cos\delta_B \cos\gamma} \qquad R_{CP\pm} = 1 + r_B^2 \pm 2 r_B \cos\delta_B \cos\gamma \tag{1.10}$$

Il metodo GLW risulta difficilmente applicabile sperimentalmente, in parte a causa dei piccoli rapporti di diramazione (*branching ratios*), che per l'intera catena di decadimenti sono dell'ordine di 10^{-5}, ma soprattutto poiché l'accesso al parametro r_B è dato in forma di una piccola deviazione di $R_{CP\pm}$ dal valore unitario. Anche l'accesso a γ è difficile poiché il denominatore della frazione che compare nella definizione di $\mathcal{A}_{\mathcal{CP}}$ è di un ordine di grandezza più grande del numeratore.

1.2.2 Metodo Atwood-Dunietz-Soni

Per risolvere i problemi del metodo GLW è stato proposta una tecnica alternativa e complementare da Atwood, Dunietz e Soni [5]. Al fine di rafforzare il contributo del decadimento del mesone B soppresso $B^- \to \bar{D}^0 K^-$ (e CP-coniugato) rispetto al più favorito $B^- \to D^0 K^-$, e di conseguenza l'interferenza tra i due, si sceglie di far seguire il decadimento del B favorito da un decadimento del mesone D soppresso, ed il decadimento del B soppresso da un decadimento del D favorito.

I diagrammi di Feynman dei processi di decadimento dei mesoni B e D favoriti e soppressi, coinvolti nella misura, sono presentati in figura 1.3. Gli stati finali cercati sono $B^\pm \to K^\pm(K^\mp\pi^\pm)_D$. Dove per la coppia di mesoni tra parentesi, si richiede che la massa invariante sia compatibile con la massa di un mesone D. Poiché la carica dei kaoni nello stato finale è opposta, si parla di *eventi dal segno opposto* (*Wrong Sign events*), distinguendoli dagli eventi di decadimento in stati specifici

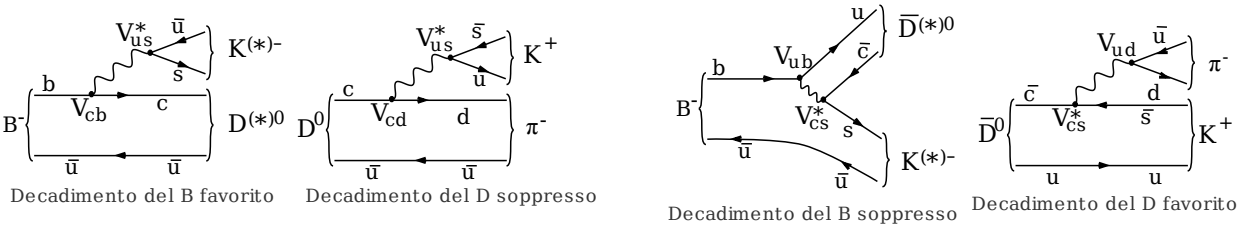

Figura 1.3: Diagrammi di Feynman dei processi scelti per la misura dell'angolo γ tramite metodo ADS.

di sapore con due kaoni della medesima carica nello stato finale, chiamati *eventi dallo stesso segno* (*Right Sign events*).

Le definizioni del rapporto e dell'asimmetria ADS seguono le definizioni generali 1.6 e 1.7. Ossia

$$\mathcal{R}_{ADS} = \frac{\Gamma(B^- \to (K^+\pi^-)_D K^-) + \Gamma(B^+ \to (K^-\pi^+)_D K^+)}{\Gamma(B^- \to (K^-\pi^+)_D K^-) + \Gamma(B^+ \to (K^+\pi^-)_D K^+)} \tag{1.11}$$

$$\mathcal{A}_{ADS} = \frac{\Gamma(B^- \to (K^+\pi^-)_D K^-) - \Gamma(B^+ \to (K^-\pi^+)_D K^+)}{\Gamma(B^- \to (K^+\pi^-)_D K^-) + \Gamma(B^+ \to (K^-\pi^+)_D K^+)} \tag{1.12}$$

La relazione con i parametri r_B e δ_B, nonché con l'angolo γ sono riportate di seguito.

$$R_{ADS} = r_B^2 + r_D^2 + r_B r_D \cos\gamma \cos(\delta_B + \delta_D) \qquad A_{ADS} = \frac{2 r_B r_D \sin(\delta_B + \delta_D)\sin\gamma}{r_B^2 + r_D^2 + 2 r_B r_D \cos\gamma\cos(\delta_B + \delta_D)} \tag{1.13}$$

È importante osservare che l'addendo unitario presente nella relazione GLW 1.10 non è presente nelle relazioni ADS. Ciò comporta che il parametro r_B contribuisca in modo più importante al rapporto R_{ADS}, per ragioni analoghe l'asimmetria ADS può raggiungere valori molto più elevati rispetto all'asimmetria GLW. Esperimenti precedenti a LHCb hanno misurato valori superiori al 30%. Il grave limite di questa tecnica è rappresentato dai piccolissimi rapporti di diramazione delle catene di decadimenti considerate, che sono di circa due ordini di grandezza inferiori ai valori, già ridotti, per il metodo GLW.

1.3 L'acceleratore LHC ed il rivelatore LHCb al CERN

Il *Large Hadron Collider* (LHC, grande collisore di adroni) è un collisore di 27 chilometri di circonferenza posto al confine Franco-Svizzero. L'innovativa struttura dei magneti di deflessione dei fasci di particelle permette di far circolare nel medesimo tunnel due fasci di protoni (o ioni pesanti) in direzioni opposte. Grazie a questa particolarità, la luminosità di LHC ha potuto superare di due ordini di grandezza la luminosità del TeVatron, il precedente acceleratore protone-antiprotone sviluppato al Fermilab. Infatti il maggiore ostacolo al raggiungimento di un'elevata luminosità presso l'acceleratore statunitense era costituito dal ridotto ritmo di produzione di anti-protoni, ostacolo aggirato da LHC facendo collidere due fasci di protoni. I fasci di protoni sono strutturati in pacchetti (*bunches*) che vengono accelerati con cavità risonanti. I pacchetti si incrociano con una separazione temporale di 25 ns o multipli. Attualmente gli anelli di accumulazione contengono 1092 pacchetti separati temporalmente di 50 ns. LHC opera ad un'energia nel centro di massa $\sqrt{s} = 7$ TeV, ma il progetto prevede di portare l'energia a 14 TeV dopo l'arresto tecnico del 2013.

La sezione d'urto di produzione di coppie $b\bar{b}$ ad un'energia nel centro di massa di 7 TeV è di $\sim$ 300 μb, il che ha permesso di produrre $\sim 10^{10}$ coppie con i primi 37 pb^{-1}, laddove Belle e Babar nell'intero periodo di acquisizione dati, con 1.5 ab^{-1}, hanno prodotto 1.5 $\times 10^9$ coppie $b\bar{b}$. Tuttavia, l'efficienza di ricostruzione presso le B-factories è notevolmente più elevata di quanto non possa essere in ambiente adronico. Per questa ragione, i rivelatori generici, quali CMS ed ATLAS, non sono considerati sufficienti per lo studio della ricca fisica dei mesoni B, alla quale è stato dedicato LHCb [12]. Poiché ad LHC la produzione di mesoni contenenti quark *bottom* è concentrata nelle regioni a piccolo angolo rispetto ai fasci, come mostrato in figura 1.4 in una

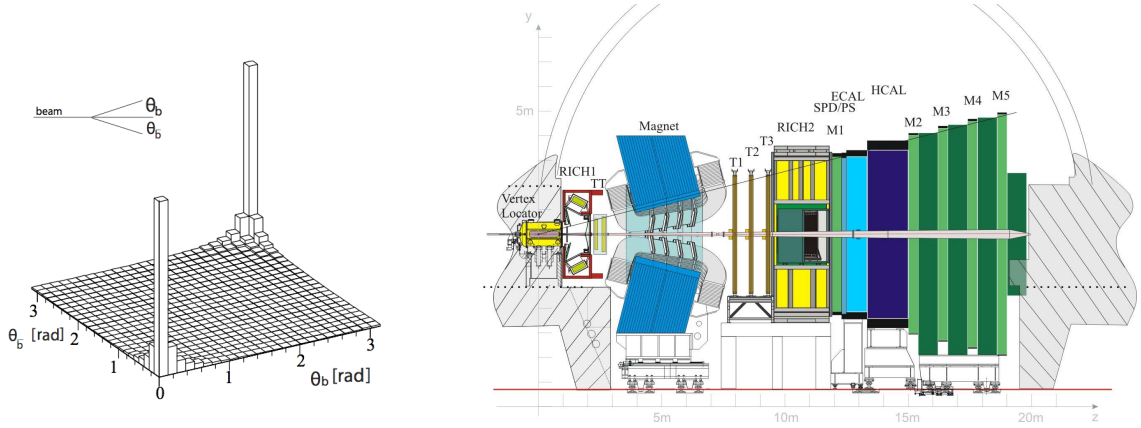

Figura 1.4: A sinistra, distribuzione rispetto all'angolo polare della produzione di adroni contenenti quark b (θ_b) e $\overline{b}$ ($\theta_{\overline{b}}$) ottenuta con simulation Monte Carlo. La distribuzione risulta concentrata nelle direzioni a basso angolo rispetto alla direzione del fascio, inoltre è evidente l'elevata correlazione tra la direzione degli adroni contenenti b e $\overline{b}$ in uno stesso evento. A destra, una rappresentazione schematica del piano verticale di LHCb. Il piano è detto Non-Bending Plane indicando che il campo magnetico deflette le particelle in un piano ortogonale a quello rappresentato.

simulazione ottenuta con il generatore PYTHIA, la sfida di un rivelatore dedicato alla fisica del b consiste nell'estendere l'accettanza geometrica alle regioni più prossime ai fasci, senza perdere la capacità di gestire i più elevati ritmi di conteggio che caratterizzano tali regioni. Inoltre il cosiddetto b-tagging, ovvero la procedura d'identificazione di un adrone contenente un quark b, è basato sulla distanza percorsa in volo dal mesone prima di decadere: tale distanza, percorsa alle energie di LHC, nell'accettanza geometrica di LHCb (dato importante data l'elevata dipendenza dall'angolo polare θ), è relativamente elevata (7 mm in media), ma richiede comunque un elevata risoluzione del sistema di tracciamento tanto sulla posizione quanto sulla quantità di moto delle particelle. Uno dei problemi da considerare nella progettazione di un sistema di tracciamento è la possibilità di scattering multiplo delle particelle tracciate, per ridurre questo problema si tenta di ridurre la quantità di materiale nella regione di tracciamento (prima dei calorimetri). Queste considerazioni hanno spinto i progettisti di LHCb ad adottare una struttura per il rivelatore a *single-arm* (braccio singolo), che si contrappone alle scelte adoperate dalle altre tre grandi collaborazioni di LHC (ATLAS, CMS ed ALICE), che preferiscono rivelatori che ricoprano quasi l'intero angolo solido. L'accettanza geometrica di LHCb si estende su un intervallo di pseudorapidità[2] $1.9 < \eta < 4.9$.

La scelta di una struttura a braccio singolo permette di allocare le infrastrutture necessarie all'esperimento fuori dall'accettanza geometrica, in modo da ridurre la quantità di materiale nella regione di tracciamento a meno di una lunghezza di radiazione X_0. Data la distribuzione angolare degli adroni contenenti quark b, inoltre, tale scelta riduce l'accettanza geometrica di un fattore 2 rispetto ad una struttura simmetrica a doppio braccio, ma riduce di un fattore assai più elevato i costi.

1.3.1 Il sistema di tracciamento

Il sistema di tracciamento è costituito dal localizzatore di vertice (VELO, VErtex LOcator) e da cinque stazioni di tracciamento al silicio. La misura della quantità di moto è ottenuta misurando la deflessione in un campo magnetico di 1.1 T generato da un magnete dipolare. Il VELO è un insieme di 25 stazioni di tracciamento al silicio, molto prossimo al punto di interazione. È progettato in modo da poter misurare le coordinate r (definita come la distanza dall'asse del fascio) e ϕ (ossia l'angolo azimutale attorno all'asse del fascio) grazie all'opportuna segmentazione sulle due facce di ciascun rivelatore, inoltre le stazioni sono dimensionate in modo tale che ciascuna particella nell'accettanza geometrica attraversi almeno tre stazioni.

[2] La pseudorapidità è definita come $\eta = -\ln\left[\tan\frac{\theta}{2}\right]$, dove θ è l'angolo polare tra l'asse del fascio e la direzione di volo della particella.

Lo studio dei molti decadimenti adronici dei mesoni e barioni contenenti un quark b richiede un apparato di identificazione delle particelle (*particle identification*) affidabile. LHCb è dunque equipaggiato con due rivelatori ad anello Cherenkov (RICH, *Ring Image CHerenkov*) con tre radiatori, che permettono di misurare la velocità $\beta = v/c$ delle particelle dall'ampiezza del cono di luce Cherenkov emessa al passaggio della particella nel materiale radiatore. L'utilizzo di tre differenti materiali per i tre radiatori (aerogel al silicio e C_4F_{10} nel RICH 1, CF_4 nel RICH 2) permette di ottenere un'accettanza estesa su un ampio intervallo in termini di quantità di moto ($\sim 1 \div 150$ GeV/c) e angolo polare θ. L'informazione sulla velocità viene combinata con l'informazione sulla quantità di moto ottenuta dalla misura della deflessione in campo magnetico, o eventualmente con l'energia depositata nei calorimetri per assegnare a ciascuna particella una cosiddetta *likelihood*, una probabilità non normalizzata, per ciascuna ipotesi di massa.

1.3.2 I calorimetri

Per il lavoro qui presentato è inoltre di fondamentale importanza la presenza di un calorimetro elettromagnetico, seguito da un calorimetro adronico. Il calorimetro elettromagnetico (ECAL, *Electromagnetic CALorimeter*) è un dispositivo a campionamento in cui si alternano strati di piombo e scintillatore plastico in una struttura chiamata *shashlik*. Lo scintillatore è letto attraverso fibre ottiche collegate a tubi fotomoltiplicatori posizionati esternamente e protetti dall'intenso campo magnetico. Il calorimetro elettromagnetico è segmentato lateralmente in celle quadrate con dimensione variabile: nella regione più interna le celle hanno un lato di 4 cm, nella regione intermedia il lato misura 6 cm mentre nella regione più esterna è di 12 cm. Uno strato di scintillatore a segmentazione fine (SPD, *Scintillator Pad Detector*) è posto davanti al calorimetro in modo da distinguere particelle cariche da particelle neutre prima che la cascata elettromagnetica abbia inizio. Dopo uno spessore di 2.5 X_0 è posto un secondo strato di scintillatore del tutto analogo, con lo scopo di distinguere due cascate elettromagnetiche molto prossime, tramite una misura di posizione precisa quando le cascate sovrapposte sono ancora poco sviluppate in termini di dimensione trasversale, e dunque ancora distinguibili. Questo secondo scintillatore viene indicato col nome di *Pre-Shower* (PS).

Il calorimetro adronico (HCAL, *Hadronic CALorimeter*) ha lo scopo di misurare l'energia degli adroni che superano il calorimetro elettromagnetico grazie al maggiore potere di penetrazione. Mentre nel calorimetro elettromagnetico le interazioni che causano la cascata sono prevalentmenete elettromagnetiche, nel calorimetro adronico si aggiunge l'interazione nucleare forte, con lo scambio di gluoni virtuali tra gli adroni incidenti e i nuclei degli atomi nel calorimetro. Il calorimetro adronico è un dispositivo a campionamento composto da strati di ferro e scintillatore. Diversamente dal calorimetro elettromagnetico, l'orientazione degli strati è parallela all'asse del fascio. Lo spessore del calorimetro adronico è di 5.6 lunghezze d'interazione nucleare.

1.3.3 Sistema di rilevazione muoni

Le sole particelle che possono attraversare entrambi i calorimetri sono muoni e neutrini. Mentre per i neutrini si rinuncia alla misura, adottando algoritmi detti di energia trasversa mancante nella ricostruzione dei decadimenti, i muoni vengono rivelati tramite quattro stazioni (M2, ..., M5) di camere proporzionali a fili allocate dietro i calorimetri. Per migliorare la misura della direzione di volo dei muoni, una quinta camera chiamata M1 è anteposta ai calorimetri, con lo scopo di registrare la posizione di attraversamento del muone, prima dell'attraversamento dei calorimetri che può causare una deflessione a causa del fenomeno dello scattering multiplo. Le particelle registrate in M1 non sono esclusivamente muoni, pertanto questa stazione non viene usata nel processo di identificazione delle particelle. Inoltre, nella regione centrale, la stazione M1 è investita da un flusso di particelle cariche molto elevato. Il ritmo di conteggio è tale che le camere proporzionali a filo non sono sufficienti, per questa ragione si sono adottate camere GEM (*Gas Electron Multiplier*) in grado di sostenere ritmi di conteggio assai più elevati.

Metodo GLW

	BELLE [13] (2006)	BABAR [14] (2010)	CDF [15] (2009)	Combination
N_{CP+}	149	477	91	-
R_{CP+}	$1.13 \pm 0.16 \pm 0.08$	$1.18 \pm 0.09 \pm 0.05$	$1.30 \pm 0.24 \pm 0.12$	1.18 ± 0.08
A_{CP+}	$0.06 \pm 0.14 \pm 0.05$	$0.25 \pm 0.06 \pm 0.02$	$0.39 \pm 0.17 \pm 0.04$	0.24 ± 0.06
$\int \mathcal{L} dt$	-	-	5 fb^{-1}	
$N_{b\bar{b}}$	275 milioni	467 milioni		

Metodo ADS

	BELLE [16] (2011)	BABAR [17] (2010)	CDF [18] (2010)	Combination
$N_{RS}(B \to D\pi)$	49000	24000	17700	90700
N_{WS}	35	19	34	88
R_{ADS}	$0.0163^{+0.0044\ +0.0007}_{-0.0041\ -0.0013}$	$-0.011 \pm 0.006 \pm 0.002$	$0.0225 \pm 0.0084 \pm 0.0079$	-0.0153 ± 0.034
A_{ADS}	$-0.39^{+0.26+0.04}_{-0.28-0.03}$	$-0.86 \pm 0.47^{+0.12}_{-0.16}$	$-0.63 \pm 0.40 \pm 0.23$	-0.53 ± 0.21
$\int \mathcal{L} dt$	-	-	1 fb^{-1}	
$N_{b\bar{b}}$	722 milioni	467 milioni		

Tabella 1.1: Numero di eventi per i diversi canali considerati nelle analisi GLW ed ADS effettuate a Babar, Belle e CDF. Riferimento: [19]

1.3.4 Trigger

LHCb è dotato di un trigger di alto livello versatile, che possa essere adattato alle esigenze della collaborazione in continua evoluzione. L'obiettivo del trigger è la riduzione drastica del numero di eventi da registrare su nastro rispetto all'elevato numero eventi generati da LHC ma di scarso interesse. I trigger a più basso livello hanno lo scopo di ridurre il numero di eventi per unità di tempo ad una frequenza sufficientemente bassa da rendere possibile la progressiva ricostruzione di ciascun evento, e quindi l'applicazione del trigger di più alto livello che decreta se l'evento deve essere registrato o meno. Sebbene LHCb fosse progettato per far fronte ad un numero di collisioni medio per *bunch crossing* (incrocio tra i pacchetti di protoni) μ pari a 0.4, al fine di aumentare la luminosità nel primo periodo di funzionamento di LHC μ è stato aumentato fino a 2.5. Ad oggi, risulta prossimo a 1.8 interazioni per *bunch crossing*. Il trigger è strutturato in tre livelli, il livello 0 (L0) è un trigger hardware a latenza fissa (4 μs) che utilizza informazioni provenienti da calorimetri, rivelatore per muoni e sistema di tracciamento, e il numero di collisioni protone-protone nel singolo evento. L'obiettivo è passare da una frequenza di collisioni di 40 MHz ad un ritmo di eventi di 1 MHz da inviare al trigger di livello 1 (HLT 1). Quest'ultimo ha lo scopo si confermare o smentire le selezioni di L0, con algoritmi più complessi. Una volta che la selezione è confermata, si stima che il ritmo di eventi sia di circa 30 kHz, a questo punto è possibile una ricostruzione globale dell'evento che permette al successivo HLT2 disporre di tutte le informazioni provenienti dal rivelatore e di ridurre il ritmo a 3 kHz. La registrazione degli eventi risulta allora possibile. Si osservi che entrambi i livelli dell'HLT sono implementati come algoritmi C++ eseguiti su una PC-farm con più di 20 000 processori.

1.4 Elementi dell'analisi GLW con canali $B^{\pm} \to D^0 K^{\pm}$

Come descritto nella sezione d'introduzione alla teoria, i decadimenti $B^{\pm} \to D^0 K^{\pm}$ rappresentano il canale preferenziale per la misura dell'angolo γ con i metodi GLW ed ADS. In questa sezione descrivo brevemente i risultati ottenuti da *BABAR*, Belle e CDF, quindi illustro i primi passi mossi da LHCb. Utilizzando i criteri di selezione individuati dalla collaborazione, ho ripetuto l'analisi scrivendo i programmi necessari per la selezione dei candidati e l'esecuzione di un algoritmo di fit sulla distribuzione della massa invariante ricostruita per il decadimento dei mesoni B.

1.4.1 Risultati da B-factories e CDF

Le B-factories ricostruiscono i mesoni D tanto negli autostati di CP pari quanto nei dispari, mentre CDF ha riportato studi relativi ai soli autostati di CP pari. Per gli stati di CP pari sono stati considerate sia coppie di kaoni carichi K^+K^- sia le coppie pioni carichi $\pi^+\pi^-$, mentre gli autostati

di CP dispari vengono ricostruiti in $K_s^0\{\pi^0,\ \phi,\ \omega\}$. Gli autostati di CP dispari sono più difficili da ricostruire, così che non sono stati inclusi nella prima analisi di LHCb. Il numero di eventi osservati, nonché il valore per gli osservabili (asimmetria e rapporto GLW) sono riportati in tabella 1.1. È importante osservare che la precisione sugli osservabili migliora con l'aumentare del numero di eventi misurati. Per questa ragione, una più elevata statistica implica una migliore precisione nella determinazione degli osservabili, e dunque di γ. Babar ha osservato violazione diretta di CP con il metodo GLW con un significato statistico di 3.6 σ, utilizzando la più elevata statistica finora analizzata in cerca di decadimenti $B^{\pm} \to D^0 K^{\pm}$ con successivo decadimento del D^0 in autostati di CP.

Come discusso nel seguito, LHCb afferma di aver selezionato un centinaio di eventi nel primo anno di acquisizione, dato che, se estrapolato alla luminosità attesa per la fine di quest'anno (1 fb^{-1}) mostra che il contributo dell'esperimento LHCb alla misura dell'angolo γ è già competitivo.

Anche il metodo ADS è stato utilizzato da B-factories e CDF. I tre esperimenti hanno misurato valori molto differenti per A_{ADS}, ma il segno è lo stesso per i tre risultati. In particolare, Belle, che ha la statistica più elevata, ha ottenuto una asimmetria ADS diversa da zero con un significato statistico di oltre 4 σ. Come anticipato, il valore dell'asimmetria A_{ADS} è piuttosto elevato (39%). L'accesso ai parametri r_B e δ_B, nonché all'angolo γ è dunque favorito.

1.4.2 L'analisi preliminare di LHCb

È sempre difficile simulare correttamente le condizioni sperimentali di un ambiente soggetto a rapide e frequenti variazioni. Anche con una descrizione precisa della distribuzione dei materiali e della risposta dei sistemi di rivelazione di un esperimento ad alta efficienza, la simulazione non è mai perfetta. Per tutta la durata del 2010, l'acceleratore LHC ha subito importanti modifiche alle condizioni di funzionamento così come il trigger di LHCb. Di conseguenza le simulazioni Monte Carlo (MC) sono considerate spesso come potenzialmente inaffidabili ed il loro uso nelle analisi è sconsigliato. Ciononostante, comparare i campioni ottenuti da simulazioni Monte Carlo e campioni di dati realmente acquisiti è spesso di grande utilità nel processo di comprensione e studio dell'apparato sperimentale. Per questa ragione, la cosiddetta *Monte Carlo Validation* (conferma del Monte Carlo) rispetto a dati reali è un punto di partenza comune a molte analisi.

Il secondo passo consiste solitamente nello studio dell'influenza che ha il trigger sul segnale cercato. Questo studio è condotto utilizzando il campione Monte Carlo il cui livello di affidabilità è stato valutato al punto precedente.

Dopodiché si selezionano le variabili discriminanti tra segnale e fondo e si ottimizzano i tagli sulle selezioni basandosi su un campione puro di segnale ottenuto con Monte Carlo e campioni di fondo ottenuti con simulazioni Monte Carlo, oppure da dati reali selezionati in modo opportuno. Infine si valuta il numero di eventi di segnale, o contando il numero di eventi nella regione del segnale e sottraendo il numero di eventi di fondo attesi, o tramite un fit i cui parametri liberi sono i coefficienti di normalizzazione delle differenti funzioni di distribuzione di probabilità, precedentemente stimate con campioni Monte Carlo o, dove possibile, con dati reali. Questo secondo metodo fa maggiore affidamento sul Monte Carlo, ma permette una più raffinata descrizione del fondo e di conseguenza una maggiore affidabilità sul numero di eventi di segnale stimato.

Dal momento che la larghezza di decadimento Γ è proporzionale al numero di eventi, gli osservabili (asimmetria e rapporto) possono essere dedotti direttamente dal numero di eventi di segnale misurati. Nella versione definitiva delle analisi l'architettura dell'algoritmo di fit è tale che i parametri liberi sono gli osservabili stessi. Il vantaggio è duplice: da un lato ottenere l'osservabile da un singolo fit su un singolo grafico garantisce che il trattamento dei dati è il medesimo per tutti i parametri che entrano nella definizione dell'osservabile, garanzia assente se le singole larghezze di decadimento vengono misurate tramite fit su grafici differenti. In secondo luogo, si incarica così lo stesso algoritmo di fit del trattamento statistico che permette di passare dal numero di eventi all'osservabile, complicato dalla correlazione esistente tra i vari parametri.

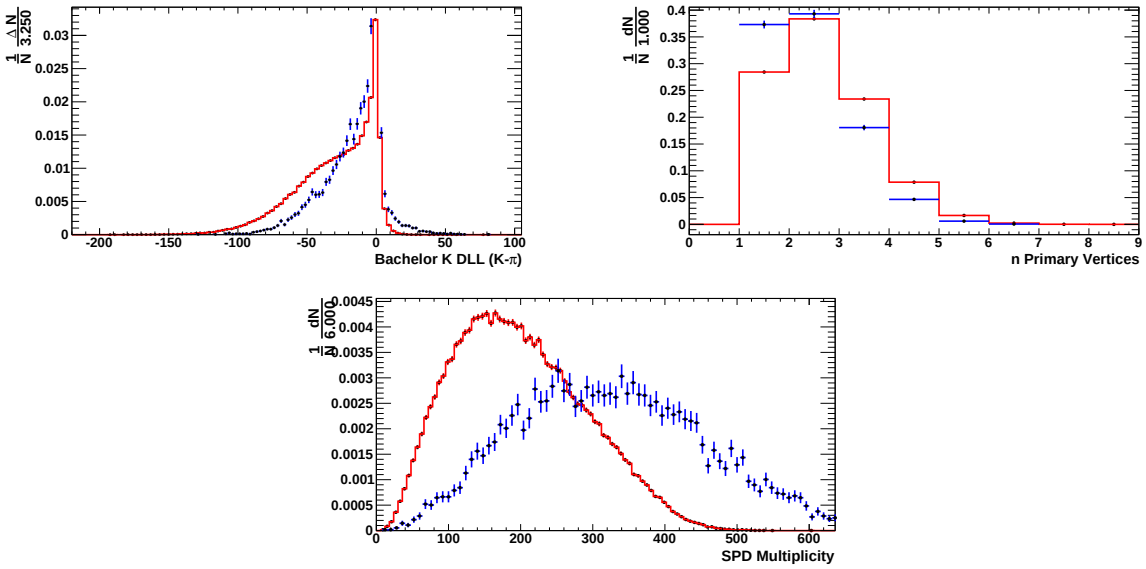

Figura 1.5: Confronto tra la funzione di distribuzione di probabilità normalizzata per un campione di decadimenti $B^{\pm} \to D^0\pi^{\pm} \to (K^{\pm}\pi^{\mp})\pi^{\pm}$. Il Monte Carlo è rappresentato come una linea rossa continua, i dati come punti blu. Le variabili che sono state considerate sono, da sinistra a destra: la *likelihood* di identificazione come kaone della traccia nubile (*bachelor track*, la traccia del pione o kaone proveniente dal vertice di decadimento del mesone B), il numero di vertici primari ricostruiti nel VELO ed il numero di conteggi dello *Scintillator Pad Detector (SPD)*.

1.4.3 Conferma del Monte Carlo

Confermare la simulazione Monte Carlo significa confrontare le distribuzioni delle variabili discriminanti o coinvolte nella selezione degli eventi di segnale, per il Monte Carlo e per i dati reali. Le distribuzioni considerate mostrano un accordo abbastanza buono tra Monte Carlo e dati reali, tranne per quanto riguarda le variabili associate a:

- Identificazione delle particelle tramite rivelatore RICH, rappresentata a sinistra in figura 4.1
- la molteplicità dell'evento, ovvero il numero di collisioni o di tracce in uno stesso evento, al centro e a destra di figura 4.1.

Il problema sull'identificazione di particella è probabilmente legato ad una cattiva simulazione del radiatore ad aerogel del RICH 1. Studi degli esperti sono in corso. Anche il problema sulla molteplicità è studiato, e si ritiene che sia principalmente dovuto alle molte variazioni delle condizioni di funzionamento dell'apparato sperimentale reale, laddove i dati simulati sono stati ottenuti con un set di parametri fisso.

Le analisi definitive devono affrontare il problema ricalibrando il Monte Carlo. Per le analisi preliminari qui presentate la procedura di ricalibrazione non è stata considerata essenziale, a patto di ricordare che l'affidabilità del Monte Carlo non è eccellente.

1.4.4 Considerazioni sul trigger

Una conoscenza almeno superficiale della struttura del trigger è necessaria per la comprensione delle efficienza di selezione dei vari algoritmi. Per identificare la configurazione del trigger una chiave unica di identificazione (TCK, *Trigger Configuration Key*) è assegnata a ciascun set di parametri di configurazione. Lo studio dell'efficienza di selezione tramite analisi Monte Carlo per i diversi TCK utilizzati nel 2010 ha permesso di concludere che l'efficienza di selezione è sostanzialmente indipendente dalla chiave di configurazione.

Due categorie di algoritmi di trigger sono considerate: linee fisiche e linee topologiche. Le prime sono basate sull'identificazione di specifici canali d'interesse, le linee topologiche cercano

invece decadimenti adronici di mesoni B in due, tre o quattro particelle cariche. L'efficienza risulta leggermente più elevata per le linee fisiche ($\sim 18.5\%$) che per le linee topologiche (~ 17.5 %).

Lo studio di eventuali distorsioni delle funzioni di distribuzione di probabilità introdotte dal trigger può essere affrontato grazie alle categorie TIS e TOS. Gli eventi appartenenti alla categoria dei selezionati in base al segnale (*Trigger On Signal*, TOS) vengono selezionati dal trigger perché viene riconosciuto il segnale richiesto dall'analisi, gli eventi selezionati indipendentemente dal segnale (*Trigger Independent Signal*, TIS), vengono invece selezionati per caso e in numero molto più ridotto da linee di trigger che cercano altri eventi e possono essere confrontati con gli eventi TOS per valutare le distorsioni introdotte selezionando gli eventi in base al segnale.

1.4.5 Selezione off-line

Il processo di selezione di eventi di segnale a partire dagli eventi preselezionati dal trigger è preceduto dalla ricostruzione globale e si divide in due stadi consecutivi. La ricostruzione globale off-line dell'evento viene effettuata con maggiore precisione rispetto a quanto fatto a livello di trigger. Il processo di ricostruzione, gestito dalla collaborazione, viene eseguito una sola volta per tutte le analisi, le quali partono dalla ricostruzione globable per selezionare eventi o raffinare la ricostruzione di poche variabili d'interesse.

Dopo la ricostruzione globale si procede con il primo passo di selezione, chiamato *stripping*, una classificazione degli eventi in base a categorie piuttosto ampie, ad esempio per questa analisi si è utilizzata la linea di stripping *StrippingB2DXWithD2hhLine* che applica tagli poco severi per selezionare eventi $B \to DX$ con il mesone $D \to hh$, con X qualsiasi insieme di particelle ed h qualsiasi adrone carico che ha raggiunto i rivelatori. Oltre che dalla linea di stripping, un campione di dati è caratterizzato dalla versione del software di ricostruzione nonché di stripping utilizzata. L'analisi qui presentata è stata ottenuta con la versione *Reco08Stripping12* e corrisponde ad una luminosità integrata di 37 pb^{-1}.

Il secondo passo consiste in una selezione ottimizzata per ciascuna diversa analisi.

Nel caso dei canali $B^{\pm} \to D^0 h^{\pm} \to (h^+h^-)h^{\pm}$, le selezioni applicate si dividono in tre categorie:

- Selezioni sulle tracce cariche
  - Quantità di moto trasversa (p_T), la componente ortogonale all'asse dei fasci della quantità di moto della particella. Questa selezione permette selezionare mesoni prodotti dal decadimento di una particella pesante.
  - χ^2 di separazione dal punto d'interazione. Imponendo che la separazione sia superiore ad una data soglia, si escludono gli adroni prodotti direttamente nell'interazione protone-protone.
  - Likelihood di identificazione come kaone. Una particella identificata come un adrone, e con una bassa likelihood come kaone, viene considerata un pione. Si taglia su questa variabile imponendo soglie superiori o inferiori a seconda che si cerchi un pione o un kaone, rispettivamente.
- Selezioni sul candidato D^0
  - Distanza di massimo avvicinamento delle tracce figlie (*Distance Of Closest Approach*, DOCA). Imporre che la distanza di massimo avvicinamento tra le tracce figlie sia più piccola di una data soglia permette di escludere coppie di tracce che non si avvicinano a sufficienza da poterle considerare come provenienti dal decadimento della stessa particella.
  - χ^2 tra il vertice di decadimento del B e quello di decadimento del D (distanza di volo). Tramite questo test si considera l'ipotesi che le tre particelle provengano dallo stesso vertice di decadimento del B e si tenta di scartare quest'eventualità imponendo che il χ^2 del fit ottenuto forzando questa ipotesi sia superiore ad una data soglia.

Charged tracks	D^0 **candidate**	$B^\pm$ **candidate**
$p_T > 330$ MeV/c	DOCA < 0.3	Punto d'interazione $\chi^2 < 9$
χ^2 di separazione dal P.I. > 21	χ^2 distanza di volo > 252	DOCA < 0.1
PID K-likelihood traccia celibe (kaone) > 3	DIRA > 0.992	Distanza di volo $\chi^2 > 72$
PID K-likelihood traccia celibe (pione) $<$ -2	χ^2 / N_{dof} di vertice < 6	DIRA > 0.99995
PID-K likelihood traccia figlia (D) (kaone) > 0	Finestra di massa: {-40, +30} MeV/c^2	
PID-K likelihood traccia figlia (D) (pione) < 10		

Tabella 1.2: Elenco delle soglie per le selezioni applicate all'analisi del canale $B^\pm \to D^0(hh)h$. La definizione e la spiegazione delle selezioni sono nel testo.

  - Angolo θ_D tra la la direzione della quantità di moto del mesone D e il segmento che congiunge il vertice di decadimento del D e il vertice primario. Dal momento che la massa del D è molto superiore alla massa del kaone o pione prodotto nel decadimento del B, la quantità di moto del mesone D è allineata con la quantità di moto del mesone B, di conseguenza l'angolo θ_D è molto piccolo.
  - Qualità della ricostruzione del vertice di decadimento (χ^2 per grado di libertà).
  - Massa ricostruita in un intorno del valore noto della massa del mesone D.

- Selezioni sul candidato $B^\pm$
  - χ^2 di separazione dal punto di interazione. In questo caso s'impone che le traccia ricostruita per il B sia compatibile con l'ipotesi di generazione dal punto d'interazione.
  - Distanza di massimo avvicinamento delle tracce figlie (DOCA).
  - χ^2 di separazione tra vertice di decadimento del B e il vertice primario (distanza di volo).
  - Angolo tra la quantità di moto del B e il segmento che unisce il vertice di decadimento del B e il vertice primario. Questo angolo è idealmente nullo, ma a seguito degli errori nella ricostruzione della traccia o della quantità di moto, può risultare leggermente diverso da zero. Comunque, i tagli su questa variabile sono sempre molto severi.

I valori delle soglie, riportati in tabella 1.2, sono stati ottimizzati utilizzando campioni Monte Carlo per il segnale, e per il fondo dati con la massa ricostruita per la coppia di mesoni provenienti dal D non compatibile con la massa nominale del D. Questa regione prende il nome di banda laterale nella massa del D (D-mass sideband). La definizione di banda laterale è rappresentata in figura 1.6. I campioni ottenuti dalle bande laterali possono rappresentare correttamente il contributo combinatorio al fondo, ma esistono altre sorgenti di fondo dovute al decadimento di mesoni D reali non provenienti da decadimenti del B. In questo caso la massa ricostruita per il D è compatibile con la massa nominale, ma la massa ricostruita per il B non lo è. In particolare canali di questo tipo danno origine ad una massa ricostruita per il B inferiore al valore nominale, in quanto sono solitamente generati da decadimenti del mesone B in più di due corpi con perdita di una particella, la quale non può così contribuire al calcolo della massa invariante. Canali di questo tipo vengono indicati con il nome di *fondo di massa inferiore* (*Low Mass Background*), e sono dominati da decadimenti $B^\pm \to D^* h \to (D^0\gamma)h^\pm$ oppure $(D^0\pi)h^\pm$ nei quali viene perso il fotone o il pione lento π. A causa della struttura di elicità di questo decadimento (il mesone D^* è vettoriale, tutti gli altri mesoni sono pseudo-scalari, il fotone è vettoriale) la massa invariante dei prodotti del decadimento calcolata escludendo il contributo della particella perduta (un pione o un fotone) assume una struttura a doppio picco.

1.4.6 Scelta delle funzioni di distribuzione di probabilità per i diversi contributi e fit

Per prendere in considerazione il problema del fondo di massa inferiore, si sceglie di utilizzare un fit che abbia per parametri liberi i coefficienti di normalizzazione delle funzioni di distribuzione di probabilità delle diverse componenti precedentemente studiate tramite un Monte Carlo. Laddove

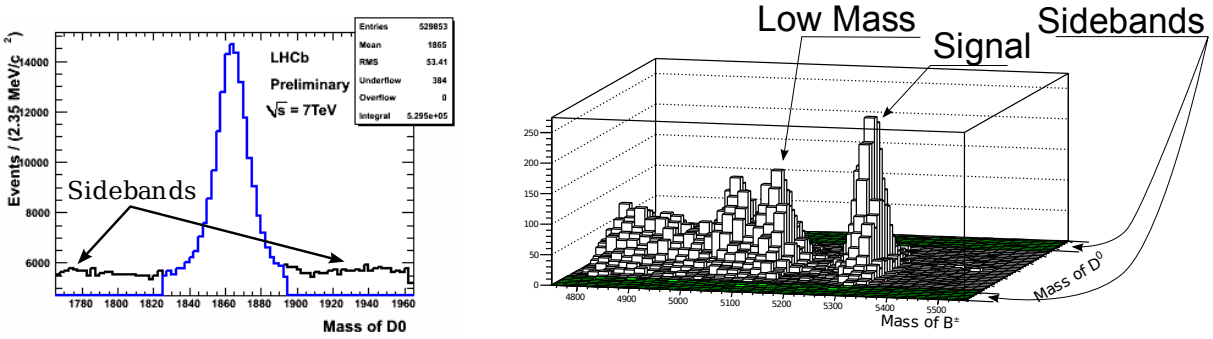

Figura 1.6: A sinistra, distribuzione della massa ricostruita per le tracce figlie del mesone D^0, in blu è evidenziata la porzione selezionata dalla finestra di massa che esclude le bande laterali (in nero). Le soglie della finestra di massa sono scelte in modo tale da escludere il segnale e costituire un campione di fondo combinatorio.

Canale	**N^o eventi**
$B^\pm \to D^0\pi^\pm$ con $D^0 \to K^\pm\pi^\mp$	5091$\pm$ 86
$B^\pm \to D^0\pi^\pm$ con $D^0 \to K^+K^-$	286 $\pm$ 20
$B^\pm \to D^0\pi^\pm$ con $D^0 \to \pi^+\pi^-$	121 $\pm$ 14
$B^\pm \to D^0K^\pm$ con $D^0 \to K^\pm\pi^\mp$	377 $\pm$ 26
$B^\pm \to D^0K^\pm$ con $D^0 \to K^+K^-$	36 $\pm$ 8
$B^\pm \to D^0K^\pm$ con $D^0 \to \pi^+\pi^-$	10 $\pm$ 7

Tabella 1.3: Numero di eventi ottenuto dal fit per ciascuno dei sei canali analizzati. La luminosità integrata utilizzata è di 37 pb^{-1}e l'incertezza è solamente statistica.

possibile, è preferibile scegliere funzioni di distribuzione parametriche, in modo da utilizzare lo studio MC per inizializzare i parametri del fit, lasciandoli però liberi di variare in un determinato intervallo. Esistono tuttavia funzioni eccessivamente complesse per essere descritte con un numero ragionevole di parametri, in questi casi si preferisce utilizzare una funzione di distribuzione di probabilità non parametrica.

È stato possibile utilizzare funzioni parametriche per il picco del segnale e per il fondo di bassissima massa (rappresentato in verde in figura 1.7), le altre funzioni di distribuzione sono non parametriche [20] e sono state ottenute a partire da campioni MC per ciascuno dei canali di fondo considerati. Si è osservato che, per quanto riguarda i fondi di bassa massa, esiste uno scostamento di circa 4 MeV/c^2 tra la distribuzione degli eventi nel campione Monte Carlo e dati reali. Questa differenza è stata corretta traslando opportunamente le funzioni di distribuzione del MC in modo che rappresentino correttamente i dati. Come per i fondi di bassa massa, anche la contaminazione da $B \to DK$ con il kaone identificato come un pione, o inversamente $B \to D\pi$ con i pione identificato in un kaone, è stata rappresentata con funzioni non parametriche.

Il fit è basato su RooFit [21] ed utilizza un algoritmo basato sulla massimizzazione di una likelihood che ignora la ripartizione in *bin* dell'istogramma (*unbinned likelihood fit*). I parametri liberi del fit sono la posizione e la larghezza del picco del segnale, e la normalizzazione di ciascuna funzione di distribuzione (numero di eventi). I rapporti relativi tra le componenti del fondo di bassa massa sono stati fissati considerando l'efficienza Monte Carlo e il numero di eventi attesi.

Il fit per i canali di decadimento soppressi, con D verso autostati di CP, non possono contare sulla simulazione Monte Carlo dei canali di fondo (bassa massa). Essi sono pertanto limitati alla regione del segnale, utilizzando come fondo il solo contributo dalle bande laterali.

I risultati sono riportati in tabella 1.3.

1.4.7 Conclusioni sull'analisi $B^\pm \to D^0h^\pm$

L'accordo tra la funzione di fit e i dati è buono, tuttavia ci sono regioni dello spettro in cui non è perfetto. La scelta arbitraria della funzione di distribuzione per la regione di bassissima massa

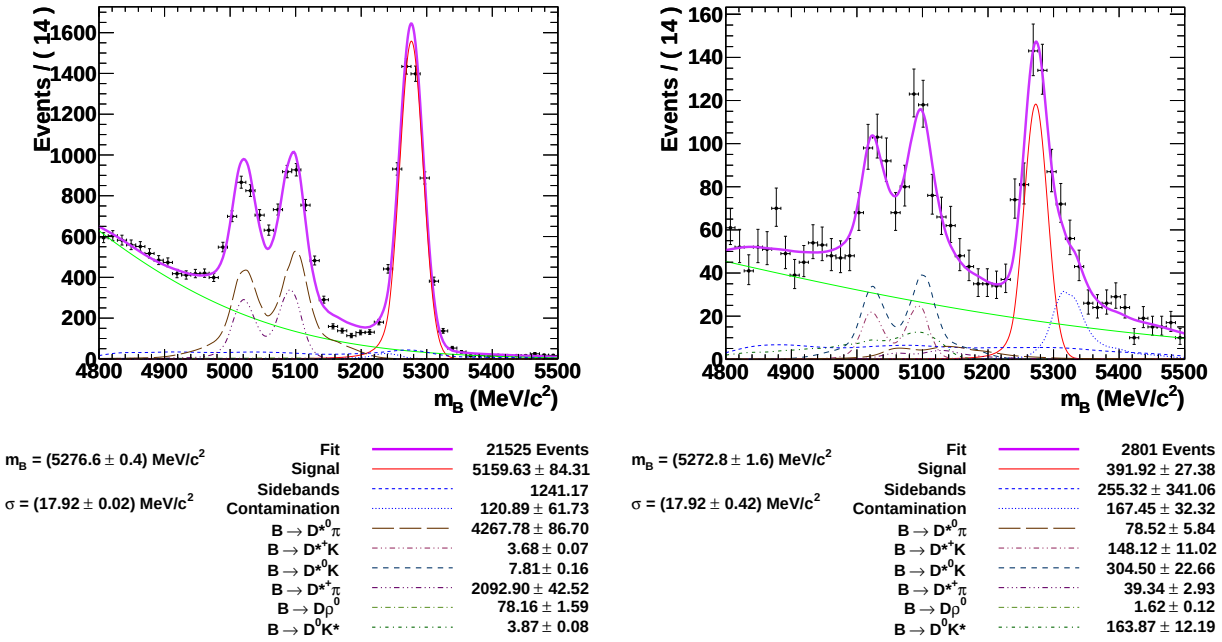

Figura 1.7: A sinistra, spettro della massa ricostruita per il mesone B nel canale $B^{\pm} \to D^0\pi \to (K^{\pm}\pi^{\mp})\pi$. A destra l'analogo per il canale $B^{\pm} \to D^0K^{\pm} \to (K^{\pm}\pi^{\mp})K^{\pm}$. Il fondo rappresentato con una linea continua verde, è il fondo di bassissima massa ed è la sola funzione parametrica oltre al segnale (linea continua rossa).

può essere causa del problema. Tra le varie scelte possibili, questa è la più conservativa, poiché introduce un maggior numero di eventi di fondo sotto il picco del segnale.

Inoltre ci sono diversi fattori fuori controllo: la massa ricostruita per il B nel canale DK è traslata di circa 4 MeV verso valori negativi rispetto al canale $D\pi$, il che può essere sintomatico di una cattiva rappresentazione della contaminazione da errata identificazione della traccia nubile.

Le efficienze di ricostruzione per Monte Carlo e dati reali sono troppo differenti, anche questo è sintomo di una insufficiente comprensione dei diversi passaggi dell'analisi, dal trigger alla selezione offline. Infine le selezioni non sono sufficientemente ottimizzate per rendere la misura dei canali soppressi sufficientemente precisa, tentativi di analisi multivariabile (discriminanti di Fisher, reti neurali e *Boosted Decision Tree*) hanno mostrato che è possibile aumentare l'efficienza in modo significativo.

Estrapolando i 46 eventi CP-pari misurati ad una luminosità di 1 fb^{-1} attesa per la fine del 2011, si prevede di disporre di un campione di $\sim$ 1300 eventi. Con questo campione statistico pari a circa 2.8 volte la statistica di *BaBar* (447 eventi), si potrebbe ottenere una precisione quasi raddoppiata sugli osservabili $\mathcal{A}_{CP+}$ ed $\mathcal{R}_{CP-}$. In ogni caso, l'obiettivo delle analisi preliminari non è ottenere il massimo della statistica possibile, ma piuttosto comprendere ogni livello della complessa catena di analisi. Una volta compresa meglio la struttura sarà possibile operare con analisi multivariabile e solo allora le tecniche di trattamento dei dati saranno comparabili a quelle utilizzate dalle B-factories, e i numeri di eventi davvero confrontabili, in quanto ottenuti con tecniche analoghe.

1.5 Analisi preliminari sul canale $B^{\pm} \to D^{*0}h^{\pm}$

Il mesone D^{*0} è uno stato vettoriale eccitato del mesone D^0 e decade in $D^0\gamma$ nel 38% dei casi e in $D^0\pi^0$ con una probabilità del 62%. La massa del D^{*0} è di 2007 MeV/c^2, solamente 42 MeV/c^2 più pesante del D^0 (massa di 1865 MeV/c^2), di conseguenza la particella neutra e leggera che proviene dal decadimento del D^* è di bassa energia. Il pione neutro decade piuttosto rapidamente in due fotoni, anch'essi di bassa energia. Di conseguenza, per studiare questo canale risulta di essenziale importanza l'utilizzo del calorimetro elettromagnetico per ricostruire fotoni di bassa energia. Questa peculiarità rende il canale piuttosto difficile perché il calorimetro elettromagnetico

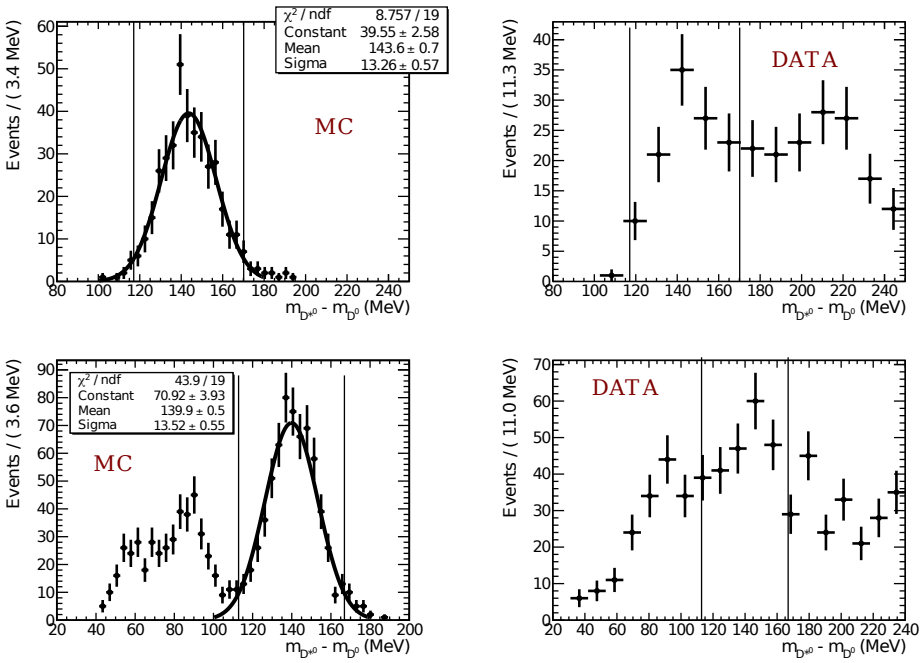

Figura 1.8: Distribuzione di probabilità della differenza tra le masse ricostruite per il D^* ed il D^0 provenienti da uno stesso decadimento del B. In alto il canale con $D^{*0} \to D^0\pi^0$, in basso il canale con $D^{*0} \to D^0\gamma$. A sinistra un campione Monte Carlo, a destra il campione di dati reali. La larghezza è dovuta alla risoluzione energetica del calorimetro.

è stato progettato e calibrato con maggiore interesse per i fotoni di alta energia, come ad esempio i fotoni provenienti dai decadimenti radiativi $B \to K^*\gamma$, e di conseguenza l'utilizzo per la misura di questo canale è considerato oltre il proposito del rivelatore.

Nonostante le difficoltà, il canale $B^\pm \to D^{*0}h$ è molto promettente per la misura dell'angolo γ in quanto, se da un lato la statistica sull'angolo γ presso le B-factories è costituità per circa metà da canali contenenti un D^*, dall'altro la produzione di questi canali presso LHCb è abbondante ed essi sono selezionati dal trigger e dallo stripping con buona efficienza, come è evidente osservando il contributo di questi canali alla regione di bassa massa in figura 1.7.

Lo studio di questo canale, al fine di valutare la possibilità di utilizzarlo per incrementare statistica e precisione sulla misura dell'angolo γ, costituisce il contributo originale di questo lavoro di tesi.

1.5.1 Variabili discriminanti

Principalmente due variabili discriminanti sono state considerate nello studio di questi canali. La qualità della ricostruzione del D^* viene valutata misurando la differenza tra le masse ricostruite per il D^* e per il D^0 provenienti dalla medesima catena di decadimenti ($B^\pm \to D^{*0}\pi^\pm \to (D^0\gamma)\pi^\pm$ e $B^\pm \to D^{*0}\pi^\pm \to (D^0\pi^0)\pi^\pm$).

La distribuzione in questa variabile è riportata in figura 1.8. Nell'istogramma relativo al campione Monte Carlo analizzato in cerca del decadimento contenente $D^{*0} \to D^0\gamma$, è evidente un picco sulla sinistra dovuto al *cross-feeding* proveniente dal decadimento di $D^{*0} \to D^0\pi^0$ con $\pi^0 \to \gamma\gamma$ e la perdita di un fotone. In questo caso mancando l'energia di un fotone, la massa invariante ricostruita viene spinta verso valori inferiori.

Un'altra variabile discriminante è offerta dalla particolare struttura di elicità dei decadimenti del D^{*0}. Nel sistema di riferimento del D^*, la geometria del decadimento $B^\pm \to D^{*0}h^\pm$ è tale che il momento angolare di spin risulta ortogonale alla direzione di volo del mesone B. Scegliendo quest'ultima come asse z si può affermare che il D^{*0} è polarizzato rispetto all'asse z e che la componente z del suo spin è nulla. È allora possibile descrivere la cinematica del decadimento del D^{*0} in termini di armoniche sferiche e mostrare che la probabilità di decadimento dipende

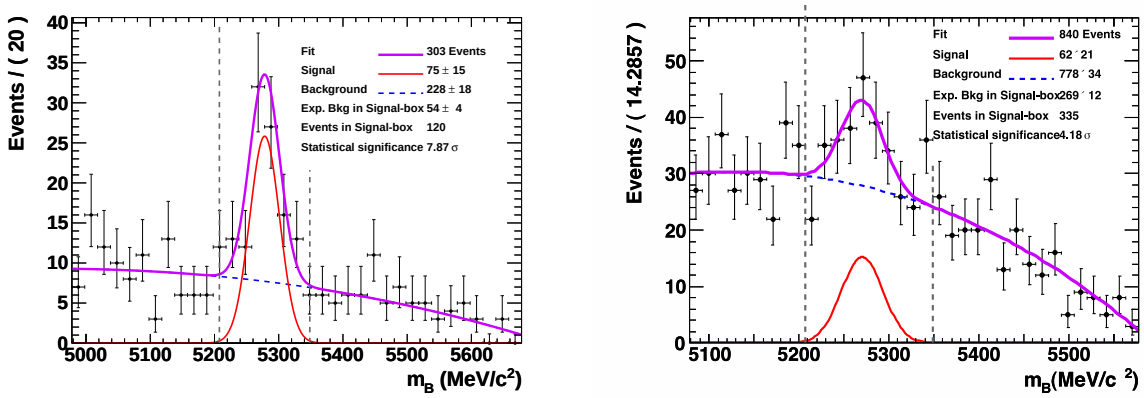

Figura 1.9: Funzione distribuzione della massa ricostruita per il mesone B nel canale $B^{\pm} \to D^{*0}\pi^{\pm}$ con $D^{*0} \to D^0\pi^0$ (sinistra) e $D^{*0} \to D^0\gamma$ (destra). Il D^0 è ricostruito in entrambi i casi come $D^0 \to K^{\pm}\pi^{\mp}$.

	LHCb — 37 pb^{-1} (2010)			**LHCb — 2 fb^{-1} (2012)**		
	$N_{RS}\ (D\pi)$	$N_{RS}(DK)$	N_{CP+}	$N_{RS}\ (D\pi)$	$N_{RS}\ (DK)$	N_{CP+}
D^0	5091	422	46	275k	23k	2484
$D^0\gamma$	62	5.1	0.6	3348	275	32.4
$D^0\pi^0$	75	6.3	0.7	4050	340	37.8

Tabella 1.4: Estrapolazione del numero di eventi attesi a fine 2012 per i canali utili alla misura GLW tramite i canali con e senza D^0. L'estrapolazione a fine 2012 (2 fb^{-1}) mostra che con le condizioni attuali i canali contenenti D^{*0} non potranno contribuire significativamente alla misura dell'angolo γ.

dall'angolo polare θ, tra la direzione di volo del mesone D^0 e l'asse z nel sistema di riferimento del D^{*0}, secondo la relazione

$$\begin{cases} P(\theta) \propto \cos^2\theta & \text{per } D^{*0} \to D^0\pi^0 \\ P(\theta) \propto \sin^2\theta & \text{per } D^{*0} \to D^0\gamma \end{cases} \tag{1.14}$$

La variabile $\cos\theta$ è più discriminante nel caso del decadimento in $D^0\pi^0$ che nel caso di $D^0\gamma$, il che rende la reiezione del fondo di questo secondo canale più difficile.

Il risultato delle selezioni per i decadimenti $B^{\pm} \to D^{*0}\pi^{\pm}$ è presentato in figura 1.9, a sinistra per $D^{*0} \to D^0\pi^0$ e a destra per $D^{*0} \to D^0\gamma$. Il numero di eventi di segnale ottenuto dal fit è di 75 ± 14 per il canale con $D^{*0} \to D^0\pi^0$, e di 62 ± 21 eventi per il γ, per il canale con $D^{*0} \to D^0\gamma$.

1.5.2 Conclusioni sull'analisi $B^{\pm} \to D^{*0}\pi^{\pm}$

I risultati descritti nel paragrafo precedente indicano che le attuali condizioni del rivelatore LHCb e del software di analisi non sono sufficienti ad includere il canale contenente un D^{*0} nell'analisi ADS, né a contribuire significativamente all'analisi GLW. Il numero di eventi raccolti per i decadimenti considerati è di circa quaranta volte inferiore a quello ottenuto per il canale equivalente ($B^{\pm} \to D^0K^{\pm}$) che non contiene D^* (vedi tabella 1.3).

L'estrapolazione del canale soppresso con un D^0 ricostruito in autostati pari di CP è riportato in tabella 1.4. Con poco più di una trentina di eventi attesi per fine 2012 in ciascuno dei canali di decadimento del D^*, la misura di un'asimmetria tra decadimenti di mesoni B^+ e B^- risulta impraticabile. Tecniche di analisi alternative devono essere considerate, ad esempio la ricostruzione dei fotoni convertiti nel materiale del sistema di tracciamento potrebbe fornire una valida alternativa al calorimetro nella misura dei fotoni di bassa energia coinvolti nel processo.

Ciononostante, la ricostruzione del canale di decadimento, seppure con bassa efficienza, e l'osservazione che trigger e *stripping* selezionano correttamente eventi di decadimento attraverso una risonanza D^{*0} come fondo del canale a tracce cariche, sono ottimi presupposti che incoraggiano lo studio di decadimenti in grado di aggiungere vincoli supplementari alla misura dell'angolo γ.

1.6 Prospettive e conclusioni

La misura dell'angolo γ del triangolo di unitarietà permette di fissare un punto di riferimento sperimentale per una descrizione del meccanismo CKM in assenza di Nuova Fisica. Tuttavia i rapporti di diramazione dei decadimenti utilizzabili per effettuare la misura sono talmente ridotti che la precisione sulla misura dell'angolo γ è di gran lunga inferiore a quella sugli altri angoli del triangolo di unitarietà.

Il grande collisore di adroni (LHC) permette di produrre una grande quantità di coppie $b\bar{b}$ grazie ad un'elevata sezione d'urto di produzione. Il rivelatore LHCb è stato progettato appositamente per massimizzare l'efficienza di ricostruzione dei decadimenti dei mesoni e barioni contenenti b, con attenzione particolare alla reiezione dei fondi.

Nel 2010 sono stati raccolti 37 pb^{-1}di dati per i quali è disponibile lo *stripping*, l'organizzazione degli eventi registrati in diverse categorie a seconda del tipo canale di decadimento ricostruito in quel dato evento. Sul campione costituito dalla categoria di *stripping* associata a decadimenti inclusivi di mesoni B in un mesone D, a sua volta decaduto in due adroni carichi, sono state applicate selezioni via via più severe fino ad ottenere uno spettro per la massa ricostruita nei decadimenti $B^{\pm} \to D^0 h^{\pm}$ con $D^0 \to h^{\pm}h^{\mp}$ contenente il segnale e canali di fondi specifici che possono essere studiati singolarmente. Un fit sullo spettro di massa ha permesso di stimare il numero di eventi per il segnale e per ciascuno dei canali di fondo considerati. L'estrapolazione dei risultati alla luminosità integrata di 1 fb^{-1} prevista per la fine dell'anno 2011 indica che, anche fissando le attuali condizioni non ottimali di analisi preliminare, LHCb disporrà di una statistica di circa 3 volte superiore rispetto alla collaborazione BaBar, autrice dell'attuale misura GLW di maggiore precisione. Inoltre studi preliminari indicano che l'utilizzo di analisi multivariabile permetterà di guadagnare un fattore 1.3 sulle efficienze di selezione, e di conseguenza sulla statistica.

Lo studio del canale a tracce cariche $B^{\pm} \to D^0 h^{\pm}$ con $D^0 \to h^{\pm}h^{\mp}$ è estendibile al canale $B^{\pm} \to D^{*0} h^{\pm}$ con $D^{*0} \to D^0\{\gamma,\ \pi^0\}$ e $D^0 \to h^{\pm}h^{\mp}$, il quale, oltre ad aggiungere vincoli teorici sull'angolo γ, ha permesso alle B-factories di incrementare significativamente la statistica utilizzata. La difficoltà dello studio di questi canali è la ricostruzione di fotoni a bassa energia, per la quale il calorimetro elettromagnetico di LHCb non è ottimizzato. Ciononostante è stato possibile mettere in evidenza questi canali di decadimento nello spettro di massa invariante per i prodotti di decadimento di candidati B, con un significato statistico superiore a 4σ per il canale con $D^{*0} \to D^0\gamma$ e di quasi 8σ per il canale contenente un π^0. Tale osservazione costituisce l'apporto originale di questo lavoro di tesi alla collaborazione LHCb.

Nonostante l'osservazione del decadimento sia risultata un successo, l'efficienza di ricostruzione è talmente ridotta che anche estrapolando il numero di eventi ricostruiti alla luminosità di 2 fb^{-1} attesa per la fine del 2012, prima dell'arresto tecnico di LHC, il numero di eventi risulta troppo basso per poter ottenere una misura sufficientemente precisa di un'asimmetria di carica, e di conseguenza dell'angolo γ. Pertanto occorre uno sforzo al fine di migliorare l'efficienza di ricostruzione del calorimetro per fotoni di bassa energia, oppure la ricerca di strategie alternative, come ad esempio la ricostruzione di fotoni di bassa energia dalla conversione in e^+e^- nel materiale di tracciamento.

Chapter 2

From the Standard Model to the measurement of γ

The Standard Model (SM) is the quantum field theory which describes all the known particles and interactions (except for gravitation). The SM description of physics is based on Lorentz and gauge symmetries, in particular it is possible to describe the three interactions (nuclear strong, nuclear weak and electromagnetic) assuming gauge symmetries. However, such a description would impose a null mass for the weak interaction gauge bosons, which experimentally is known to be higher than 80 GeV/c^2. To accommodate this observation in the Standard Model, the Higgs mechanism has been introduced: a spontaneous symmetry breaking which explains the boson masses introducing the interaction with an additional field (*Higgs field*). The evidence of such a field would be given by the discovery of the Higgs boson, one of the main aims of the Large Hadron Collider (LHC).

The coupling of the Higgs field with fermions is described introducing additional parameters related to the fermion masses. These parameters are fixed by the Nature and a theoretical expectation for them does not exist. Furthermore, they are organized in matrices which are not diagonal in the basis preserving the electroweak universality. The transformation matrix which makes them diagonal, thus corresponds to the transformation matrix between the electroweak flavor basis and the mass basis. This is the formal approach to the Cabibbo-Kobayashi-Maskawa (CKM) mechanism, which describes the quark mixing of d-type quarks only, introducing the d', s' and b' states and fixing states u, c and t as both mass and weak flavor eigenstates.

The CKM matrix is the quark mixing matrix and, therefore, it is unitary. The unitarity constraint can be exploited to construct six *unitary triangles* in the complex plane. As described below, one of these triangles is particularly relevant for b physics. Its angles are called α, β and γ in Europe and USA, and ϕ_1, ϕ_2 and ϕ_3 in Japan.

The unitarity triangles are closed polygons in the SM, but the experimental test of the geometrical relation $\alpha + \beta + \gamma = \pi$ could put in evidence New Physics effects. The measurement of α and β has been performed at B factories with an excellent precision, nonetheless unexpected contribution from New Physics in the measured values are possible, while γ can be measured in theoretically cleaner processes and sets a pure Standard Model reference in the CKM mechanism. Unfortunately the measurement of γ is difficult to achieve because of the small branching ratios of the decays involved. To improve the precision on γ one tries both to increase the statistical sample and to find new methods and channels which can increment statistics and add additional constraints on γ.

There are mainly three methods to measure the angle γ using theoretically clean processes: the first one to be proposed was the Gronau-London-Wyler (GLW) [4] method, based on charmed decays of the B charged meson to D^0K, with the D^0 in a CP eigenstate. The alternative is given by the Atwood-Dunietz-Soni (ADS) [5] method using favored and doubly Cabibbo suppressed D decays and looking for *Wrong Sign* events $B^{\pm} \to (K^{\mp}\pi^{\pm})_D K^{\pm}$, where the meson pair in parenthesis has an invariant mass consistent with the D^0 nominal mass. Finally the Giri-Grossman-Soffer-Zupa (GGSZ) [22] method has offered the most precise technique at B-factories analyzing the Dalitz plot of three-body D decays. At LHCb this method is not equally promising because of a more

structured hadronic background which makes the phase analysis more difficult.

2.1 The Standard Model

2.1.1 Symmetries

Modern theoretical physics exploits the symmetry concept to derive physical and observable effects from very general assumptions about the nature of the space-time. For example, momentum conservation is considered to be a consequence of the translational invariance of the space-time. Analogous invariances are exploited to state conservation of energy, angular moment and so on.

In Quantum Field Theory (QFT) it is usual to distinguish between continuous and discrete symmetries. Continuous symmetries involve operators defined by one or more parameters which can vary continuously, as for example time evolution, position translations, and rotations, whereas discrete symmetries are related to a numerable and finite set of operators. The Emmy Noëther's theorem states that any continuous symmetry corresponds to a physical quantity conserved in the evolution of the system, justifying the strong interest of modern physics in symmetries.

The SM discrete symmetries are C, P and T. C is the charge conjugation symmetry, and relates two states, the second containing the antiparticles of the first. The states related by the P symmetry, or parity, have opposite signs for the position vector $\mathbf{x}$. Both C and P operators have two eigenvalues: $+1$ and -1. Finally the T symmetry or Time-Reverse parity is a symmetry between states differing for the sign of the temporal component: the two states have opposite time-evolution directions. There are other discrete symmetries, as the isospin-related G-parity and supersymmetric symmetry R, which are well beyond the purpose of this document.

Symmetries can be combined to derive other relations between states. For example, the CP symmetry is the combination of charge conjugation and parity symmetry. The interest of this combination arises from the experimental evidence that C and P symmetries are violated by the nuclear weak interaction, *i.e.* weak processes behave differently for the two states related by C (or P) symmetry. The violation of the CP symmetry is less evident, but still present. The CPT symmetry is often considered not to be violated, because it constitutes a fundamental property of any Quantum Field Theory, so that renouncing to CPT invariance means to renounce to QFT, which has given remarkable results in the latest century.

Even if the first observations of CP violation in the leptonic sector have been recorded as differences in neutrino and anti-neutrino oscillations, CP violation in quark sector is sensibly easier to measure because of neutrinos evanescence. In the quark sector, CP violation is strongly related to the quark mixing described with the Cabibbo-Kobayashi-Maskawa (CKM) matrix, as described in the following.

Experimentally the violation of P was first observed in 1956 by C. S. Wu *et al.* [6] in the β decays of ^{60}Co nuclei. In 1964, CP violation was first observed by J.H. Christenson *et al.* [7] in the neutral kaon system. It is only in the year 2001 that *BABAR* and Belle experiments both observed CP violation also in the neutral B meson system [8, 9].

The importance of the CP violation

The study of CP violation effects has an important link with cosmology. One of the main aims in cosmology is to obtain the Universe composition finding a model describing the generation of matter. Combining the primordial nucleosynthesis (the dynamic generation of nuclei during the first period after the Big Bang) and stellar nucleosynthesis (the production of heavier nuclei in stars and supernovae) the consistency between the expected relative abundances and the measured data is excellent, in particular for lighter nuclei. However, the measured baryon density in the Universe requires a CP violation orders of magnitudes larger than theoretical expectations based on the CKM mechanism.

This huge discrepancy between cosmological observed baryonic asymmetry and that expected by the measured CP violation, hints that there are other CP violation sources not known today. Hence, more precise measurements on the CP violation in the quark sector, in strong connection

with quark mixing, have to be achieved in next years, in order to find or exclude contribution of New Physics to CP violation effects and asymmetry between matter and anti-matter.

2.1.2 Standard Model sectors

In Quantum Field Theory, it is usual to describe an interaction as the exchange of virtual particles which are represented as quantum excitations of a field. For example, the well known electromagnetic interaction can be described as the exchange of photons, a quantum excitation of the electromagnetic field. As a consequence we distinguish elementary particles between matter particles, as electrons or quarks constituting atoms, and interaction mediating particles, as, for example, the photon.

Fermions: leptons and quarks

Matter particles follow the Fermi-Dirac statistics and have spin $\frac{1}{2}$. A further distinction separates strongly interacting (by nuclear strong interaction) elementary fermions, called *quarks* and composing hadrons (baryons and mesons), and elementary fermions blind to strong interaction, called *leptons*.

Both quarks and leptons are ranged in three generations, each quark generation has the same quantum numbers according to the symmetry group $SU(3)_C \times SU(2)_T \times U(1)_Y$, and similarly for lepton generations. Quantum numbers are obviously different for quarks and leptons.

Quarks are named *up* (u), *down* (d), *charm* (c), *strange* (s), *top* (t) and *bottom* (b). They are organized in the following three generations:

$$\begin{pmatrix} u \\ d \end{pmatrix} \quad \begin{pmatrix} c \\ s \end{pmatrix} \quad \begin{pmatrix} t \\ b \end{pmatrix} \tag{2.1}$$

quarks in the first row are called *up*-type quarks and have electric charge $+\frac{2}{3}e$, while the lower row quarks are referred to as *down*-type quarks and have electric charge $-\frac{1}{3}e$.

Considering the weak-isospin T, related to the symmetry $SU(2)_T$, the left-chiral component of each pair of up- and down-type quarks, with the proper mixing between the three generations (see section 2.2), constitute a weak-isospin doublet (third component of weak-isospin $T_3 = \frac{1}{2}$ or $-\frac{1}{2}$), while right-handed components of quark wave-function are not coupled with charged-current weak interaction. They are weak-isospin singlets with $T_3 = 0$. Here, as in all the following discussion, chirality states are named according to the matter particle helicity, it is worth to remark that, since CP symmetry is with excellent approximation conserved, but C and P individually are violated, passing from particle to antiparticle (C symmetry) also require to exchange the chirality from right- to left-handed and vice-versa, to describe a system following the same physical laws (neglecting CP violation).

The weak hyper-charge Y, the quantum numbers associated to $U(1)_Y$, is calculated with the Gell-Mann–Nishijima [23] expression relating electric charge Q, hyper-charge Y and the third component of the electroweak isospin T_3.

$$Q = T_3 + \frac{Y}{2} \tag{2.2}$$

One can conclude that $Y = +1/3$ for left-handed up- and down-type quarks. For right-handed quarks the hyper-charge is $Y = -2/3$ for up-type quark and $Y = +4/3$ for down-type quarks.

Quarks also have a color charge involved in the $SU(3)_C$ symmetry and described by Quantum Chromo-Dynamics (QCD). The color charges are called *red*, *green* and *blue*.

Leptons are classified in charged leptons and neutral leptons or neutrinos. Charged leptons are the electron e^-, the muon μ^-, and the lepton τ^-. Neutrinos are indicated as ν_e, ν_μ and ν_τ according to the charged lepton in their own generation.

$$\begin{pmatrix} \nu_e \\ e^- \end{pmatrix} \quad \begin{pmatrix} \nu_\mu \\ \mu^- \end{pmatrix} \quad \begin{pmatrix} \nu_\tau \\ \tau^- \end{pmatrix} \tag{2.3}$$

	Massive leptons		Neutrinos		Up-type quarks		Down-type quarks	
Chirality	left	right	left	right	left	right	left	right
Charge (Q)	$-e$	$-e$	0	0	$\frac{2}{3}e$	$\frac{2}{3}e$	$-\frac{1}{3}e$	$-\frac{1}{3}e$
Weak Isospin (T)	$-\frac{1}{2}$	0	$+\frac{1}{2}$	0	$+\frac{1}{2}$	0	$-\frac{1}{2}$	0
Weak hypercharge (Y)	-1	-2	-1	0	$+\frac{1}{3}$	$-\frac{2}{3}$	$+\frac{1}{3}$	$\frac{4}{3}$

Table 2.1: Summary table of electro-weak related quantum numbers for fermions in the Standard Model.

Neutrinos are light particles ($m_\nu < 2$ eV/c^2), while charged lepton masses span from ~ 0.5 MeV/c^2 for the electron, to 1.776 GeV/c^2 for the lepton τ.

As for quarks, weak interaction only couples with the left-handed chiral component of lepton wave-function. Because of their low mass, neutrinos are considered to be pure left-handed states, while for massive leptons (and quarks), the chirality operator does not commute with the Hamiltonian, so that the chirality changes during time-evolution. For ultra-relativistic states ($v \sim c$), the mass of the particle becomes negligible when compared to its energy and the chirality state can nearly be treated as a motion invariant.

The weak hyper-charge is –1 for all left-handed leptons, –2 for right-handed charged leptons and 0 for (non-interacting) right-handed neutrinos. These values have been obtained using the Gell-Mann–Nishijima relation 2.2, considering that a charged left-handed lepton with its neutrino compose a weak-isospin doublet. Electroweak related quantum number are summarized in table 2.1.

Besides quarks and leptons, also anti-quarks and anti-leptons are described in the Standard Model. If compared to its particle, each anti-particle has opposite internal quantum numbers (Y, T, ...), including charge.

Vector bosons: the interactions

As anticipated, interactions are described as an exchange of spin-1 virtual particles following the Bose-Einstein statistic and called *gauge vector bosons*. The strong interaction is mediated by the exchange of *gluons*, massless, electrically neutral particles which transport a color charge composed of a color and an anti-color, for a total of 8 linearly independent combinations. For example, a red quark can emit a red-antigreen gluon and become a green quark respecting color conservation. Carrying a color charge, gluons can interact with each-others, a characteristic which makes the calculations in QCD harder than those performed in QED (Quantum Electro-Dynamics).

The particles mediating the charged-current interaction are $W^\pm$ bosons. The coupling of W is null with right-handed fermions or left-handed anti-fermions. The electro-weak neutral current is described through the exchange of photons (γ) and Z^0 bosons. While the photon is massless, which allows the well known long-range propagation of the electromagnetic interaction, weak bosons are massive (~ 80 GeV/c^2 and ~ 91 GeV/c^2 for $W^\pm$ and Z^0 bosons respectively), which imposes a finite and short range for the weak interaction.

The electroweak theory describes the neutral gauge bosons γ and Z^0 as the mixing of the two neutral bosons of the $SU(2) \times U(1)$ group, called W^0 and B^0. The mixing angle is called Wienberg angle θ_W and has been determined from the measured ratio between neutral- and charged-current cross sections in neutrino interactions.

The scalar boson: the Higgs boson

To justify the mass of $W^\pm$ and Z^0 bosons (which would explicitly break the gauge asymmetry with mass terms in the Lagrangian) a complex mechanism of spontaneous symmetry breaking, called Higgs Mechanism, has been introduced in the Standard Model. Even if broadly accepted, being the easiest way to explain the W and Z^0 boson masses, the Higgs mechanism is still questionable. Actually, introducing such a spontaneous symmetry breaking has given excellent results, relating the mass of gauge bosons to the weak-interaction coupling constants. Indeed the theoretical relation

between the boson masses and on the Weinberg angle

$$\frac{m_{W^\pm}}{m_{Z^0}} = \cos\theta_W \tag{2.4}$$

is obtained using the Higgs mechanism and the experimental consistency between the measurement of θ_W from charged- and neutral-current interactions and the from the ratio between W and Z masses is quite good[1]

However introducing the Higgs mechanism causes many problems to the Standard Model including re-normalization and fine-tuning questions which has brought physicists to introduce Super-Symmetric models and then String Supersymmetric Theory. Furthermore, NuTeV, after the latest measure of θ_W, claims a disagreement in equation 2.4 with a statistical significance of $\sim 3\,\sigma$. Many discussions about the reliability of the result have been advanced in the latest years, but the interesting point is that even if we have based a whole theory, the Standard Model, on the Higgs mechanism, we already know that such a mechanism is just an excellent effective theory, based on something of more fundamental. The upper energy limit for the effectivity of the Standard Model depends on the Higgs mass.

2.1.3 Standard Model Lagrangian

The Standard Model is a Lagrangian Quantum Field Theory, based on a symmetry group $SU(3)_C \times SU(2)_T \times U(1)_Y$ describing the strong interaction (QCD) as a color symmetry $SU(3)$ and the electroweak interaction through the group $SU(2)_T \times U(1)_Y$ acting on the weak isospin T and the weak hyper-charge Y.

Here we are revising the Standard Model to discuss CP violation which is an electroweak effect. Strong interaction CP violation is *a priori* meaningful, but studying the neutron dipole momentum, it has been shown that the CP violation amplitude in strong interaction is so small (if not null) that its influence if compared to electroweak effects is negligible. For this reason here we limit the discussion to the electroweak sector of the Standard Model.

The Standard Model Lagrangian density for the electroweak sector can be written as a sum of contributions

$$\mathcal{L}_{EW} = \mathcal{L}_f + \mathcal{L}_G + \mathcal{L}_{Higgs} + \mathcal{L}_{Yukawa} \tag{2.5}$$

the first term of equation 2.5 represents the fermion Lagrangian

$$\mathcal{L}_f = \sum_f \left(\overline{f}_L (i \not{D}) f_L + \overline{f}_R (i \not{D}) f_R \right) \tag{2.6}$$

where L and R indicate the chiral states of the generic fermion f. The sum runs over all the fermions in Standard Model. $\not{D}$ is the Dirac covariant derivative defined as

$$\not{D} = \gamma_\mu D^\mu = \gamma_\mu \left(\partial_\mu + igW_a^\mu T_a - ig' \frac{Y}{2} B^\mu \right) \tag{2.7}$$

which contains the coupling constants g and g' for W and B fields, for $SU(2)_T$ and $U(1)_Y$ symmetry groups, respectively, whose neutral mesons (B^0 and W^0) are mixed through the Weinberg angle to produce photon and Z^0 boson. T_a is the a-th $SU(2)_T$ generator, the $U(1)_Y$ generator has been defined as $Y/2$ to write the Gell-Mann–Nishijima relation in the form 2.2, to be specular to the hadronic spectroscopy relation between hadronic charge, hypercharge and isospin. Over-lined Dirac spinors are defined following the usual convention $\overline{A} = A^\dagger \gamma^0$.

$\mathcal{L}_G$ represents the gauge boson Lagrangian and is defined as

$$\mathcal{L}_G = -\frac{1}{4} \left(W_{i,\,\mu\nu} W_i^{\mu\nu} + B_{\mu\nu} B^{\mu\nu} \right) + \mathcal{L}_{FP} + \mathcal{L}_{GF} \tag{2.8}$$

where $\mathcal{L}_{FP}$ is the Faddeev-Popov Lagrangian and the $\mathcal{L}_{GF}$ describes a gauge fixing term, both contributions are intended to cancel unphysical degrees of freedom from the Lagrangian description

[1] The equation 2.4 is found at the leading order. Corrections due to successive orders introduce slight modifications depending on the model (renormalization scheme) used to describe such orders.

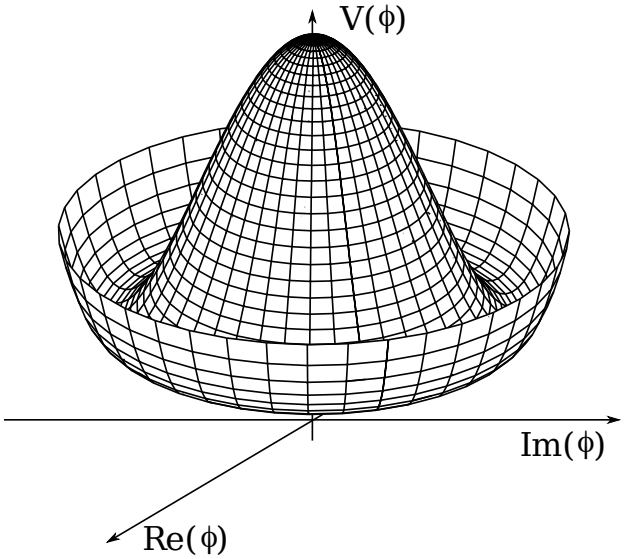

Figure 2.1: Mexican hat potential, an example in $U(1)$ for the concept of symmetry breaking. The more complex $SU(2)$ analogous potential is considered to be the Higgs potential allowing spontaneous symmetry breaking and originating particle masses in the Standard Model.

of the field. $W_i^{\mu\nu}$ and $B^{\mu\nu}$ are the four (3+1) strength tensors related to the four generators describing the $SU(2)_T \times U(1)_Y$ group. They are defined as

$$W_i^{\mu\nu} = \partial^\mu W_i^\nu - \partial^\nu W_i^\mu + g\epsilon^{ijk} W_j^\mu W_k^\nu \tag{2.9}$$

$$B^{\mu\nu} = \partial^\mu B^\nu - \partial^\nu B^\mu \tag{2.10}$$

where ϵ^{ijk} is the Levi-Civita Tensor, and appears in the expression since $\left[W_j^\mu,\ W_k^\mu\right] = i\epsilon^{ijk} W_i^\mu$.

As anticipated, the gauge boson mass is explained through the interaction of these bosons with a Higgs Field, an SU(2) field described by the doublet

$$\Phi = \begin{pmatrix} \phi^+ \\ \phi^0 \end{pmatrix} \tag{2.11}$$

This interaction is described by the Higgs Lagrangian

$$\mathcal{L}_{Higgs} = (D_\mu \Phi)^\dagger (D^\mu \Phi) + \mu^2 \Phi^\dagger \Phi - \lambda (\Phi^\dagger \Phi)^2 \tag{2.12}$$

where λ and μ are the Higgs potential parameters fixed by Nature and still unknown. The aim of such a potential is to achieve the so called spontaneous symmetry breaking. Even if the Higgs Lagrangian is symmetric under $SU(2)$ complex rotations of the Φ state, it is possible to imagine a potential for the Higgs boson, with the minimum energy for values different from the origin, *i.e.* for $\Phi \neq 0$. The potential usually offered as an example is the *mexican hat* potential presented in figure 2.1, an example in $U(1)$ which helps understanding the principle. There is an infinity of minimum energy states for non-null values of the field. The vacuum state, *a priori*, is not defined, one only knows that it is on the circumference of minimum potential, but the polar angle in unknown and can be selected arbitrarily and spontaneously by Nature, breaking the symmetry in the vacuum state whereas it is respected in the Lagrangian. The vacuum state can be described without loosing generality by the Higgs doublet

$$\Phi_0 = \frac{1}{\sqrt{2}} \begin{pmatrix} 0 \\ v \end{pmatrix} \tag{2.13}$$

where $\frac{v}{\sqrt{2}}$ can be seen as the $SU(2)$ equivalent for the radius of the minimum potential circumference in $U(1)$.

Finally, looking at equation 2.6, one can notice that there is not a mass term for fermions, whereas fermion mass is something important in the Standard Model, constituting the main difference between charged leptons, or between quarks of the same charge (up- or down-type). The

Higgs mechanism explains why bosons and fermions can have a mass. A boson mass term in the Lagrangian would break the gauge invariance of the theory. As discussed before, left-handed and right-handed fermions have different description in the electroweak theory. Since an explicit Lagrangian mass term mixes left- and right-handed terms, it can not be gauge invariant. Without the Higgs mechanism we would therefore expect all SM fermions to be massless.

Hence, the fermion mass is represented in the SM through the interaction of fermions with the Higgs field. This interaction is described by the Yukawa Lagrangian

$$\mathcal{L}_{Yukawa} = -\sum_{i,j=1}^{n_g} [Y_{ij}^{D}(\overline{Q_{Li}}\Phi)D_{Rj} + iY_{ij}^{U}(\overline{Q_{Li}}\sigma_2\Phi)U_{Rj} + Y_{ij}^{\ell}(\overline{E_{Li}}\Phi)\ell_{Rj} + h.c.] \tag{2.14}$$

where n_g represents the number of generations and equals three in the SM, σ_2 is the Pauli matrix. U_{Rj} is the j-th generation up-type right-handed quark wave-function, and analogously D_{Rj} (down-type quarks) and ℓ_{Rj} (charged leptons). Left-handed quark and lepton wave-functions are grouped in SU(2) weak doublets

$$Q_{Li} = \begin{pmatrix} U_{Li} \\ D_{Li} \end{pmatrix} \qquad E_{Li} = \begin{pmatrix} \nu_{\ell_i L} \\ \ell_{iL} \end{pmatrix} \qquad i = 1, 2, 3 \tag{2.15}$$

Y_{ij}^{D}, Y_{ij}^{U} and Y_{ij}^{ℓ}, are 3×3 matrices ranging physical parameters related to quark and charged lepton masses.

When the SM was born, neutrinos were considered to be massless particles. Today we know that neutrino masses cannot be zero because that would forbid neutrino oscillation, phenomenon well measured and broadly accepted. However, because of the small neutrino mass, the Lagrangian formulation of the Standard Model still considers neutrino masses to be negligible. Massless neutrinos (antineutrinos) would be pure left-handed (right-handed) states. Under the assumption of pure chiral states, the Higgs Lagrangian terms for neutrino-Higgs coupling would always be null because ν_R would not exist and would not appear in the Yukawa Lagrangian (2.14) and then the neutrino mass would be null. At the same time, since no neutrino can be created in a right-chirality state (they are blind to any interaction), under the assumption of mass less neutrino, chirality would commute with the Hamiltonian, freezing the chirality state. No left-hanfed neutrino could therefore exist.

One concludes that the massless property of a neutrino can be considered equivalent to the chiral purity of its quantum state. This observation is important because massless neutrino would exclude CP violation from the leptonic sector as shown below.

Standard Model interactions

The interaction Lagrangians are included in the Lagrangian 2.5, but can be written explicitly to make the interpretation easier. Writing an interaction Lagrangian means to write explicitly the covariant derivative 2.7 and to calculate terms coupling fermion and boson fields. For the electroweak interaction one gets

$$\mathcal{L}_{int} = \mathcal{L}_{cc} + \mathcal{L}_{nc} \tag{2.16}$$

where $\mathcal{L}_{cc}$ is the Lagrangian describing the charged current interaction, and $\mathcal{L}_{nc}$ describes neutral current interactions (photon an Z^0 exchange).

The charged current interaction Lagrangian is found to be

$$\mathcal{L}_{cc} = \frac{g}{\sqrt{2}}\left(J_{\mu}^{+}W^{\mu+} + J_{\mu}^{-}W^{\mu-}\right) \tag{2.17}$$

where W^+ and W^- are the two charged states in the adjoint representation of the $SU(2)_T$ diagonalizing the charge operator. The neutral current interaction Lagrangian is

$$\mathcal{L}_{nc} = eJ_{\mu}^{em}A^{\mu} + \frac{g}{\cos\theta_W}\left(J_{\mu}^{3} - \sin^2\theta_W J_{\mu}^{em}\right)Z^{\mu} \tag{2.18}$$

where A^μ is the electromagnetic quadri-potential and Z^μ is the quadri-vector describing the Z^0 field. e is the elementary charge, related to the electroweak coupling constants by

$$e = \sin\theta_W \cos\theta_W \sqrt{g^2 + g'^2} \tag{2.19}$$

The various current terms J used in in equation 2.17 and 2.18 are defined below.

$$J^+_\mu = \bar{U}_L \gamma_\mu D_L + \bar{\nu}_L \gamma_\mu \ell_L \tag{2.20}$$

$$J^-_\mu = J^{+\dagger} = \bar{D}_L \gamma_\mu U_L + \bar{\ell}_L \gamma_\mu \nu_L \tag{2.21}$$

$$J^3_\mu = \frac{1}{2}\left(\bar{U}_L \gamma_\mu U_L - \bar{D}_L \gamma_\mu D_L + \bar{\nu}_L \gamma_\mu \nu_L - \bar{\ell}_L \gamma_\mu \ell_L\right) \tag{2.22}$$

$$J^{em}_\mu = \frac{2}{3}(\bar{U}_L \gamma_\mu U_L + \bar{U}_R \gamma_\mu U_R) - \frac{1}{3}(\bar{D}_L \gamma_\mu D_L + \bar{D}_R \gamma_\mu D_R) - (\bar{\ell}_L \gamma_\mu \ell_L + \bar{\ell}_R \gamma_\mu \ell_R) \tag{2.23}$$

$J^\pm$ describe the quantum currents coupled to $W^\pm$ bosons, J^3 describes the current coupled to W^0, to get the Z^0 current the combination of J^3 and J^{em} (the electromagnetic current) is used in equation 2.18. $J^\pm$ expression will be used in the next section to define quark mixing in charged current weak interactions.

2.2 The Cabibbo-Kobayashi-Maskawa (CKM) matrix

In the previous section I have summarized some aspects of the Standard Model, in this section I introduce the quark mixing matrix, known as Cabibbo-Kobayashi-Maskawa (CKM) matrix within the Standard Model formalism.

2.2.1 Definition

Considering the Yukawa Lagrangian, and factorizing the Φ term one can write equation 2.14 in the form

$$\mathcal{L}_{Yukawa} = -\sum_{i,j=1}^{n_g} [Y^D_{ij}(\overline{Q_{Li}})D_{Rj} + iY^U_{ij}(\overline{Q_{Li}}\sigma_2)U_{Rj} + Y^\ell_{ij}(\overline{E_{Li}})\ell_{Rj} + h.c.]\Phi \tag{2.24}$$

Considering the Higgs excitation as a perturbation h with respect to the vacuum state Φ_0 defined in equation 2.13, one can write the Higgs doublet in the form

$$\Phi = \Phi_0 + \mathbf{h} = \frac{1}{\sqrt{2}} \begin{pmatrix} 0 \\ v + h \end{pmatrix} \tag{2.25}$$

where v and h are both real. Indeed, the generic perturbation $\mathbf{h}$ can be represented as a scalar perturbation of v, neglecting an $SU(2)$ transformation which leaves the Lagrangian invariant.

Hence, the Yukawa Lagrangian in Weyl representation becomes

$$\mathcal{L}_{Yukawa} = -\sum_{i,j=1}^{n_g} \left[Y^D_{ij}(0,\ D^\dagger_i) \begin{pmatrix} 0 \\ D_j \end{pmatrix} + Y^U_{ij}(0, U^\dagger_i) \begin{pmatrix} 0 \\ U_j \end{pmatrix} + Y^\ell_{ij}(0, \ell^\dagger_i) \begin{pmatrix} 0 \\ \ell_j \end{pmatrix} \right] (v + h) \tag{2.26}$$

where vectors represents Dirac spinors and the following γ^0 explicit form has been used

$$\gamma^0 = \begin{pmatrix} 0 & \mathbf{1} \\ \mathbf{1} & 0 \end{pmatrix} \tag{2.27}$$

which is valid in Weyl representation only.

One can observe that, since fermion masses are described in QFT by terms $-\bar{\psi} m \psi$ in the Dirac Lagrangian, the diagonal elements of Y matrices reproduce masses in the Standard Model. However, whether the Y matrices were not diagonal there would be a difference between the mass

and the weak-interaction bases, introducing terms between quarks of the same electric charge, but belonging to different generations. The mass matrices are defined as

$$M^U_{jk} \equiv -\frac{v}{\sqrt{2}} Y^U_{jk} \quad , \quad M^D_{jk} \equiv -\frac{v}{\sqrt{2}} Y^D_{jk} \quad \text{and} \quad M^l_{jk} \equiv -\frac{v}{\sqrt{2}} Y^l_{jk} \tag{2.28}$$

To avoid these ambiguous terms one prefers the mass basis, choosing, for charged leptons and each quark type, the basis where the respective M matrix is diagonal. Let V^U_L be the basis-changing matrix for left-handed up-type quarks from weak-interaction to mass basis, V^D_R for right-handed down-type quarks and so on.

$$U^m_L = V^U_L U_L \quad U^m_R = V^U_R U_R \qquad D^m_L = V^D_L D_L \quad D^m_R = V^D_R D_R \tag{2.29}$$

where the index m indicates that the mass basis is used. The diagonal form of the M matrix can thus be written as

$$M^a_{diag} = V^{a\dagger}_L M^a V^a_R \qquad \text{with } a = U,\ D \tag{2.30}$$

In order to adopt in the Lagrangian formalism the same definition of quark flavor used in hadronic spectroscopy, the weak interaction charged current, as defined in equations 2.20 and 2.21, can be written in mass basis as

$$J^+_\mu = \bar{U}^m_L V^U_L \gamma_\mu V^{D\dagger}_L D^m_L + \bar{\nu}_L \gamma_\mu \ell_L \tag{2.31}$$

$$J^-_\mu = J^{+\dagger} = \bar{D}^m_L V^D_L \gamma_\mu V^{L\dagger}_U U^m_L + \bar{\ell}_L \gamma_\mu \nu_L \tag{2.32}$$

where I used the unitarity property of V matrices to replace the inverse matrix by the hermitian conjugate.

The same operation would be impossible for massless neutrinos, for which the mass basis is meaningless. However in the hypothesis of massive neutrinos the same reasoning can be repeated giving raise to the Pontecorvo-Maki-Nakagawa-Sakata (PMNS) matrix, beyond the purpose of this thesis.

Since V and γ matrices act on different spaces, their commutator is null and it is therefore meaningful to define the matrix $V_{\text{CKM}} = V^D_L V^{U\dagger}_L$. Hence,

$$J^+_\mu = \bar{U}^m_L \gamma_\mu V_{\text{CKM}} D^m_L + \bar{\nu}_L \gamma_\mu \ell_L = \bar{U}^m_L \gamma_\mu {D'}^m_L + \bar{\nu}_L \gamma_\mu \ell_L \tag{2.33}$$

where D' represents a vector of mixed down-type quarks interacting with the corresponding up-type quark and the W-boson with the same coupling constant g as leptons.

It is important to notice that, by definition, the CKM matrix is unitary, indeed

$$V^\dagger_{\text{CKM}} V_{\text{CKM}} = \{V^U_L V^{D\dagger}_L\}^\dagger V^U_L V^{D\dagger}_L = V^D_L V^{U\dagger}_L V^U_L V^{D\dagger}_L = \mathbf{1} \tag{2.34}$$

because of V matrices unitarity.

This mechanism was introduced firstly by Cabibbo [1] in 1963 when only three quarks were known. After the observation of CP violation in 1964 by Christenson *et al.* [7], Kobyashi and Maskawa [2] extended the mechanism to explain CP violation. This is why the matrix is called after the authors Cabibbo-Kobayashi-Maskawa (CMK) matrix.

2.2.2 CKM matrix and CP violation

In the previous section I have shown that the CKM matrix is defined as an unitary $n_g \times n_g$ matrix, with n_g the number of quark generations (three in the Standard Model).

A priori, the CKM matrix is complex which means that it can be parametrized with $2n_g^2$ real parameters. However these parameters are not independent. From the definition of the CKM matrix it is evident that it is unitary, which introduces a constraint for each column and for each row, *i.e.* n_g^2 constraints. Redefining the quark wave-function phases, it is possible to eliminate other $(2n_g - 1)$ parameters from the CKM matrix. From the group theory, it is known that the real group $SO(n_g)$ can be parametrized with $n_g(n_g - 1)/2$ real parameters (Euler angles), one for

each generator. Since $SO(n)$ completely spans the vectorial space of unitary real matrices $n \times n$, an unitary matrix $n_g \times n_g$ described by a number of parameters exceeding $n_g(n_g-1)/2$ cannot be reduced to a purely real matrix[2]. As a consequence the number of generations must be larger than two: the three-families Standard Model is the easiest solution, but not the only to be allowed.

The complex nature of the CKM matrix is of particular interest because it can explicitly break the CP invariance and, as a consequence of the CPT theorem, the Time Reversal symmetry, too.

Two parameterizations of the Standard Model CKM matrix have to be quoted. The PDG [24] describes the CKM matrix with three mixing angles between the three generations and a complex phase factor.

Considering the unitarity of the CKM matrix we can write it as

$$V_{CKM} = \begin{pmatrix} V_{ud} & V_{us} & V_{ub} \\ V_{cd} & V_{cs} & V_{cb} \\ V_{td} & V_{ts} & V_{tb} \end{pmatrix} = \begin{pmatrix} c_{12} & s_{12} & 0 \\ -s_{12} & c_{12} & 0 \\ 0 & 0 & 1 \end{pmatrix} \begin{pmatrix} 1 & 0 & 0 \\ 0 & c_{23} & s_{23} \\ 0 & -s_{23} & c_{23} \end{pmatrix} \begin{pmatrix} c_{13} & 0 & s_{13}e^{-i\delta} \\ 0 & 1 & 0 \\ -s_{13}e^{i\delta} & 0 & c_{13} \end{pmatrix} \tag{2.35}$$

$$= \begin{pmatrix} c_{12}c_{13} & s_{12}c_{13} & s_{13}e^{-i\delta} \\ -s_{12}c_{23} - c_{12}s_{23}e^{i\delta} & c_{12}c_{23}s_{13}e^{i\delta} & s_{23}c_{13} \\ s_{12}s_{23}s_{13}e^{i\delta} & -c_{12}s_{23} - s_{12}c_{23}e^{i\delta} & c_{23}c_{13} \end{pmatrix} \tag{2.36}$$

where $s_{ij} = \sin\theta_{ij}$, $c_{ij} = \cos\theta_{ij}$ and θ_{ij} is the mixing angle between the i-th and the j-th generations. Considering that $\theta_{13} << \theta_{23} << \theta_{12} << 1$, it is useful to introduce the Wolfenstein parameterization, a series expansion around the identity matrix. The sinus of the Cabibbo angle (θ_{12}) named λ (~ 0.23) is used to evaluate the order of any correction to the identity matrix. Considering that the correction associated to θ_{23} is expected to be about an order of magnitude smaller, $\sin\theta_{23}$ should be of the order λ^2. The proportionality coefficient is called A. An analogous consideration leads to define the proportionality coefficient between $s_{13}e^{i\delta}$ and λ^3 as $A(\rho + i\eta)$.

It is also usual to introduce the complex parameter $(\overline{\rho} + i\overline{\eta}) = -\frac{V_{ud}V_{ub}^*}{V_{cd}V_{cb}^*}$, related to $(\rho + i\eta)$ by the expression

$$\rho + i\eta = \frac{\sqrt{1 - A^2\lambda^4}(\overline{\rho} + i\overline{\eta})}{\sqrt{1-\lambda^2}(1 - A\lambda(\overline{\rho} + i\overline{\eta}))} \qquad \text{with} \quad \lambda^2 = \frac{|V_{us}|^2}{|V_{ud}|^2 + |V_{us}|^2} \quad \text{and} \quad A^2\lambda^4 = \frac{|V_{cb}|^2}{|V_{ud}|^2 + |V_{us}|^2} \tag{2.37}$$

The Wolfenstein parameterization of the CKM matrix is given below. Replacing $(\overline{\rho} + i\overline{\eta})$ to $(\rho + i\eta)$, and using λ and A as defined before, the approximated expression of the Wolfenstein representation, given below, becomes unitary to all orders in λ. [25, 26, 11].

$$V_{CKM} = \begin{pmatrix} 1 - \frac{1}{2}\lambda^2 & \lambda & A\lambda^3(\rho - i\eta) \\ \lambda & 1 - \frac{1}{2}\lambda^2 & A\lambda^2 \\ A\lambda^3(1 - (\rho + i\eta)) & A\lambda^2 & 1 \end{pmatrix} + \mathcal{O}(\lambda^4) \tag{2.38}$$

Unitarity triangles

The unitarity propriety can be exploited to write

$$[V_{CKM}^\dagger V_{CKM}]_{ik} = \sum_{j=1}^{n_g} V_{ij}^\dagger V_{jk} = \sum_{j=1}^{n_g} V_{ji}^* V_{jk} = \delta_{ik} \quad ; \quad [V_{CKM}V_{CKM}^\dagger]_{ik} = \sum_{j=1}^{n_g} V_{ij}V_{kj}^* = \delta_{ik} \tag{2.39}$$

Pointing the interest on relations with $i \neq j$, we find $n_g(n_g-1)$ complex relations which state that the sum of n_g complex numbers is zero. If represented on the complex plane $\rho \perp \eta$ (or more usally $\overline{\rho} \perp \overline{\eta}$) these relations are $n_g(n_g-1)$ polygons. The polygons (in the SM, triangles) are called

[2]This doesn't mean that the CKM matrix cannot be real: an opportune tuning of parameters can impose it to be real. As a vector (x, y, z) in R^3 can belong to the plane xy if $z = 0$.

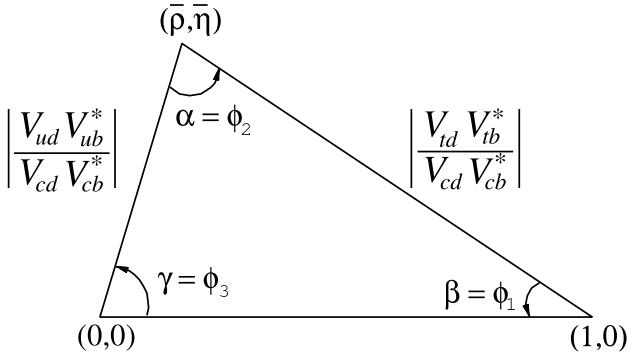

Figure 2.2: The unitarity triangle in its normalized representation.

unitarity triangles and are indexed by generation indices i and k defining the generating complex sum. In the three-generations SM there are six triangles, namely: ds, uc, sb, ct, bd and tu.

Considering that a zero-area triangle (a segment) could be represented as a purely real quantity with a simple rotation in the complex plane, it is clear that the entity of the CP violation is somehow related to the unitarity triangle area. Less naively, the importance of the CP violation is considered to be well represented by the Jarlskog invariant J, which is indeed proportional to the area of the triangles. J is a phase-convention-independent measurement of the CP-violation defined by

$$\mathrm{Im}[V_{ij}V_{kl}V_{il}^*V_{kj}^*] = J\sum_{mn}\varepsilon_{ikm}\varepsilon_{jln} \tag{2.40}$$

where ε is the Levi-Civita tensor. Even if all the triangle areas are equal ($\mathcal{O}(\lambda^6)$), the angles, and therefore the physical phases in the associated processes, are strongly different. The ds and uc triangles have two sides of order λ and one of order λ^5, they are something really near to a segment, which explains the small CP violation in kaon and D^0 systems. The sb and ct triangles have a side of order λ^4 and the other two of order λ^2, the CP violation is expected to be larger than for K and D systems, but it is experimentally difficult to measure CP violation in B_s mesons and impossible for mesons containing the top quark (they don't exist). The experimental program of LHCb aims to perform a precise measurement of CP violation in B_s oscillation, because promising results come from CDF and D$\emptyset$ analyses. Finally, the triangles bd and tu have the three sides of the same order of magnitude λ^3. While it is impossible to study the tu triangle experimentally, the bd triangle can be studied in B^0 and $B^\pm$ meson systems.

Since the importance of the bd unitarity triangle, it is usually called "the unitarity triangle". Its angles are called either α, β and γ, or ϕ_1, ϕ_2 and ϕ_3. The definition relations are

$$\alpha = \phi_2 = \arg\left[-\frac{V_{td}V_{tb}^*}{V_{ud}V_{ub}^*}\right] \qquad \beta = \phi_1 = \arg\left[-\frac{V_{cd}V_{cb}^*}{V_{td}V_{tb}^*}\right] \qquad \gamma = \phi_3 = \arg\left[-\frac{V_{ud}V_{ub}^*}{V_{cd}V_{cb}^*}\right] \tag{2.41}$$

One can notice that by definition γ is related to the complex phase δ of the CKM matrix, cause of CP violation in the SM.

In figure 2.2 the unitarity triangle is represented dividing the three sides by $V_{cd}V_{cb}^*$, in order to make one of the sides a unitary segment laying on the real axis. The triangle apex has coordinates $(\bar{\rho} + i\bar{\eta})$.

2.2.3 CP violation effects

In this section I briefly summarize the main aspects of CP violation effect in meson decays. A more detailed review can be found in [24]. For simplicity, I have chosen to limit the discussion to B mesons, but the formalism is very general and can be applied without significant modifications to K and D mesons.

Before starting to classify CP violation effects, let me introduce some formalism that will be useful below. Considering a generic decay of an initial state $|i\rangle$ to a final state $|f\rangle$ I introduce the

transition amplitude as

$$A = \langle f|\hat{H}|i\rangle \tag{2.42}$$

where H is a generic Hamiltonian operator which describes the decay. Considering $|f\rangle$ and $|i\rangle$ CP-conjugate states $|\bar{f}\rangle$ and $|\bar{i}\rangle$, I also define

$$A_{\bar{f}} = \langle \bar{f}|H|i\rangle \quad ; \quad \bar{A}_f = \langle f|H|\bar{i}\rangle \quad ; \quad \bar{A}_{\bar{f}} = \langle \bar{f}|H|\bar{i}\rangle \tag{2.43}$$

Direct CP violation or CP violation in the decay

CP violation in the decay is defined by

$$\frac{\bar{A}_{\bar{f}}}{A_f} \neq 1 \tag{2.44}$$

This means that the decay rate of a meson to a final state f is different from the decay rate of its CP-conjugate meson towards the CP-conjugate final state $\bar{f}$. Direct CP violation is the best example of difference between the behavior of matter and antimatter. Even if it an effect harder to measure than other effects, it is the only to be possible in charged B mesons, which can not oscillate (see below). Limiting the interest to charged mesons, such a difference between CP-conjugate mesons can be studied as a decay width charge asymmetry, defining the CP asymmetry:

$$\mathcal{A}_{f^\pm} = \frac{\Gamma(B^- \to f^-) - \Gamma(B^+ \to f^+)}{\Gamma(B^- \to f^-) + \Gamma(B^+ \to f^+)} \tag{2.45}$$

Indirect CP violation or CP violation in mixing

Considering now a neutral B meson system, I define the CP eigenstates as

$$|B^0_{CP+}\rangle = \frac{1}{\sqrt{2}}\left(|B^0\rangle + |\bar{B}^0\rangle\right) \quad ; \quad |B^0_{CP-}\rangle = \frac{1}{\sqrt{2}}\left(|B^0\rangle - |\bar{B}^0\rangle\right) \tag{2.46}$$

where $|\bar{B}^0\rangle \equiv CP|B^0\rangle$. Mass eigenstates are given by

$$|B^0_L\rangle = \frac{1}{\sqrt{p^2+q^2}}\left(p|B^0\rangle + q|\bar{B}^0\rangle\right) \quad ; \quad |B^0_H\rangle = \frac{1}{\sqrt{p^2+q^2}}\left(p|B^0\rangle - q|\bar{B}^0\rangle\right) \tag{2.47}$$

where p and q are parameters fixed by Nature and are strongly related to the mass difference between heavier and lighter mass eigenstates and to the difference between their decay widths.

An evidence for CP violation in mixing requires

$$\left|\frac{p}{q}\right| \neq 1 \tag{2.48}$$

In such a case, the mass eigenstates $|B^0_L\rangle$ and $|B^0_H\rangle$ differ from CP eigenstates $|B^0_{CP+}\rangle$ and $|B^0_{CP-}\rangle$. Hence it is possible time evolution modifies the state in the CP eigenstate basis, so that without any external interaction, CP conservation is violated. It is possible to show that given a p/q ratio with absolute value different from one, the transitions $B^0 \to \bar{B}^0$ and $\bar{B}^0 \to B^0$ have different widths. This means that also T symmetry is violated.

CP violation in the interference

It is possible to measure CP violation effects in the interference between a decay $B^0 \to f$ ($\bar{B}^0 \to f$) and a decay $\bar{B}^0 \to B^0 \to f$ ($B^0 \to \bar{B}^0 \to f$). This effect only occurs if B^0 and $\bar{B}^0$ share a common decay channel. Decays to CP eigenstates are typical examples.

CP violation in the interference occurs if

$$\Im\mathrm{m}\left(\frac{q}{p}\frac{\overline{A}_f}{A_f}\right) \neq 0 \tag{2.49}$$

The physical observable is the time-dependent CP asymmetry, defined as

$$\mathcal{A}_{CP}(t) = \frac{\Gamma(B^0(t) \to f) - \Gamma(\bar{B}^0(t) \to f)}{\Gamma(B^0(t) \to f) + \Gamma(\bar{B}^0(t) \to f)} \tag{2.50}$$

where $B^0(t)$ and $\bar{B}^0(t)$ represent neutral B states decaying to f a time t after they have been tagged as pure B^0 and $\bar{B}^0$ states, respectively. Studying this time dependence it is possible to extract the interference term between the two decays. This method is the most precise to measure α and β angles of the bd unitarity triangle.

The difficulty of this kind of studies is the B tagging, as the chosen decay channel does not allow to determine if the decaying meson was a B^0 or a $\bar{B}^0$ meson. However, this information is required to evaluate the CP asymmetry. Indicating with $\tilde{b}$ a b or $\bar{b}$ quark, in order to tag the B meson decaying to the measurement channel, the other $\tilde{b}$ quark produced in the originating $b\bar{b}$ pair is studied. Once the first $\tilde{b}$ quark from a $b\bar{b}$ pair decays, for example to a final state identifying the originating $\tilde{b}$ quark as a b rather than a $\bar{b}$, the quantum entanglement forces the other $\tilde{b}$ to be a pure $\bar{b}$ state. The oscillation chronometer starts there. After a time t, its decay to a final state identifying it as a $\bar{b}$ quark is an evidence for oscillation.

2.2.4 Measurement of CKM parameters

Before considering CP violation effects, I briefly describe the techniques used to measure CKM matrix parameters. There are many methods to measure each CKM parameter so that it is impossible to cover the whole topic in a few lines, but a short summary is necessary to show the importance of the measurement of the angle γ, subject of this thesis.

Measurement of parameter absolute values

The super-favored nuclear β decays $0^+ \to 0^+$ allows to obtain the best experimental resolution on $|V_{ud}|$, nonetheless there are important theoretical uncertainties, due to radiative corrections depending on the nuclear structure of the considered system. The neutron β decay $n \to pe\bar{\nu}_e$ allows a better theoretical environment because no nuclear effect is involved. However, the neutron lifetime is an input parameter for the $|V_{ud}|$ measurement and there are currently sizable disagreement between results from different experiments. Finally the $\pi^+ \to \pi^0 e^+ \nu_e(\gamma)$ offers the cleanest theoretical scenario, but the tiny branching ratio ($\mathcal{O}(10^{-8})$) causes the statistical uncertitude to dominate.

Semi-leptonic decays offer the possibility of accessing to various CKM parameters. Kaon decays $K \to \pi\ell\nu$ give access to $|V_{us}|$; the measurement of $|V_{cs}|$ and $|V_{cd}|$ can be achieved through $D \to K\ell\nu$ and $D \to \pi\ell\nu$. $|V_{cb}|$ and $|V_{ub}|$ are measured studying B meson decays through $b \to c\ell\nu$ and $b \to u\ell\nu$ transitions, respectively.

Measurement of unitarity triangle angles

Evaluating the angles of the unitarity triangle means measuring the interference between channels with a relative phase depending on the angle. To choose the measurement channels two requirements are fundamental: the decay amplitudes should depend on CKM parameters composing the angle definition (see relations 2.41); and a common final state is necessary to make the two channels interfere.

To choose the decay channel for each angle these considerations can be useful: to measure an angle having as adjacent side $V_{tb}V_{td}^*$, one should use B^0 oscillation to access top-quark related CKM parameters. Since top quark is much more accessible in loops, using meson oscillation through box diagrams allows to include in the phase budget terms depending on V_{tb} and V_{td}. In these cases one looks for CP violation in the interference. To measure an angle adjacent to $V_{cb}V_{cd}^*$ charmed B decays have to be considered. Finally the measure of angles adjacent to the $V_{ub}V_{ud}^*$ side requires $b \to u$ transitions.

To be more precise, the angle β and the angle γ can be measured using B decays to charmonium states (for β) or open-charmed states (for γ). These methods are theoretically clean, while the

determination on α requires stronger theoretical hypotheses. Furthermore the measurement of α, as well as the measurement of γ, requires decays including $b \to u$ transition which is suppressed with respect to $b \to c$ one, so that branching ratios of these decays are usually small. For this reason the measurement of α and γ requires a higher statistics (in terms of produced $b\bar{b}$) than the one needed for a β measurement achieving the same precision.

Hence, the measurement of β is the most precise, using $b \to c\bar{c}s$ transitions theoretically clean and with higher branching ratio. The *golden channel* is $B^0 \to J/\psi K_s^0$, a CP-odd eigenstate that can be used to access $\sin(2\beta)$ studying the CP violation in the interference.

Nowadays, the world average on β through direct measurements is [11]

$$\beta = \left(21.15^{+4.4}_{-4.2}\right)^\circ \tag{2.51}$$

The measurement of α is based on the analysis of charmless B mesons decays. There are different channels used to measure α, the one giving the most precise result has been $B^0 \to \rho^+\rho^-$. As for the angle β the technique is to measure the time-dependent interference between direct $B^0 \to \rho^+\rho^-$ decays and $B^0 \to \bar{B}^0 \to \rho^+\rho^-$ one. The measurement of α requires an isospin analysis of the decay, even if the $SU(2)_F$ isospin symmetry is well known, the symmetry breaking due to the mass difference between u and d quarks introduces theoretical uncertainties in the calculation. Combining all the measurements from different channels, one finds the value [11]

$$\alpha = \left(89.0^{+4.4}_{-4.2}\right)^\circ \tag{2.52}$$

The measurement of γ will be detailed in the next section. The current accepted value is [11]

$$\gamma = \left(71^{+21}_{-25}\right)^\circ \tag{2.53}$$

Both α and β measurement decays suffer from *penguin pollution*: a contribution from penguin Feynman diagrams (containing loops) to the final state. Penguin contribution can be modeled and taken into account in the phase budget with excellent precision. Nonetheless, in New Physics scenarios, new very massive particles would arise in loops before being directly measured. These massive particles could include unpredictable phases in the measurement, shifting the angle measurement by a New Physics contribution. To put in evidence such an effect, one should look for inconsistencies in the CPV description of the CKM model assuming no New Physics effect. Hence, a global fit of all the constraints collected by different experiments has been published by the group CKMfitter [11] with frequentist approach and by UTFit [27] with Bayesian approach. The two results are consistent.

The constraints considered by CKMfitter are summarized in figure 2.3, the colored areas represent the region at 95% of confidence level for the various constraints. It can be seen that the agreement is quite good. The only tension in the triangle is between V_{ub} from $B^- \to \tau^-\nu_\tau$ decays and $\sin(2\beta)$, the discrepancy is of 2.8 σ. Furthermore, we note that the measurement on γ is not enough precise to constrain the summit of the unitary triangle yet, but potentially could add important information to the global fit as I discuss in the next sections. There are different models beyond the SM which precision measurement of the CKM parameters could disprove, from SUSY contributions in loops, to the four generation Standard Model (SM4), which could add a fourth side to the unitarity triangle. Many theoretical papers have been published to suggest explanations to the tiny discrepancy of the CKM model with the experimental results. Another active domain tries to squeeze Lattice QCD input to the CKM constraints to refine the global fit and searches for possible discrepancies.

2.2.5 Cosmological consideration on CP violation.

As mentioned in paragraph 2.1.1, there are cosmological observations which lead to the "conventional wisdom" that CKM CP violation is not sufficient to explain the baryon-antibaryon asymmetry observed in the Universe.

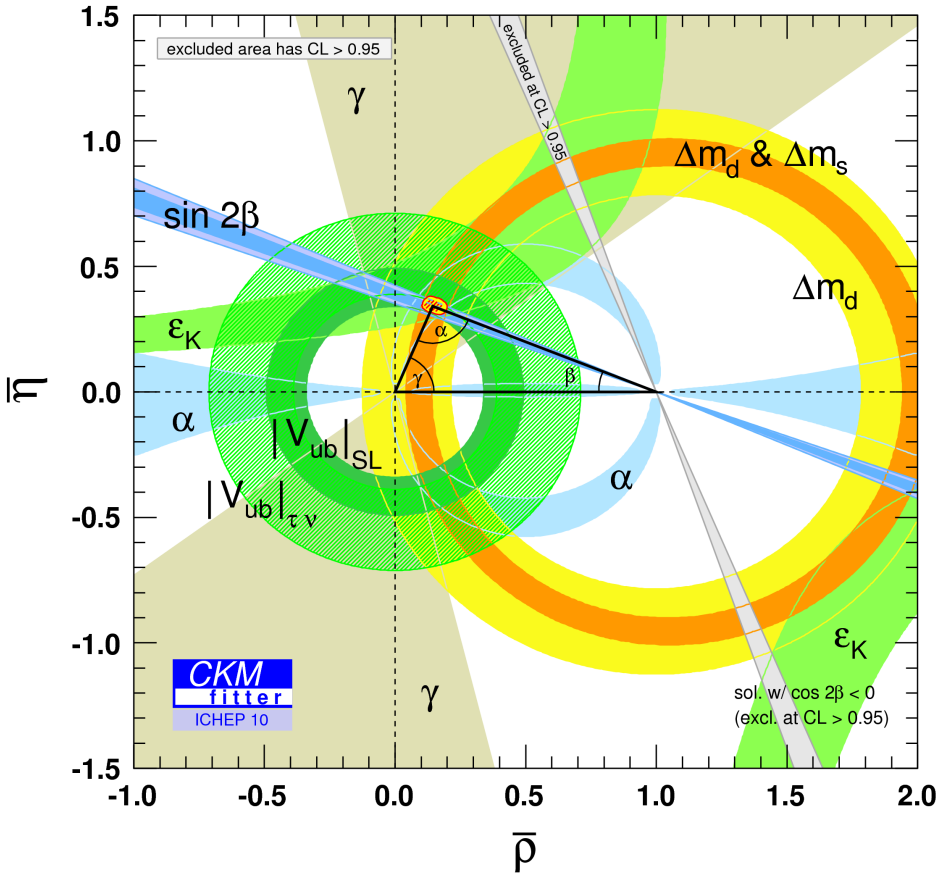

Figure 2.3: The CKMfitter global fit with experimental constraints available in October 2010. The left picture has been taken from [24], the $\overline{\rho} \perp \overline{\eta}$ plane from [11, 25]

In this section I try motivating such a statement by a simplified version of a more sophisticated treatment [28].

Defining the baryonic density in the Universe as the difference between the the number of baryons and anti-baryons per volume unit ($\Delta n_{Baryons} \equiv n_B - n_{\overline{B}}$) and the photon density n_γ as that of the diffuse cosmological background, one observes a ratio

$$\frac{\Delta n_{Baryon}}{n_\gamma} \sim 3 \times 10^{-10} \tag{2.54}$$

with baryons dominating on anti-baryons ($n_B \gg n_{\bar{B}}$).

The energy scale kT during the primordial baryogenesis was much higher than the quark and lepton masses, one can thus assume that all masses are negligible in the process. One would thus expect an equilibrium in the reaction $q\bar{q} \leftrightarrow \gamma\gamma$, which can be reached when the relation

$$\frac{n_B n_{\bar{B}}}{n_\gamma^2} \sim 1 \tag{2.55}$$

is satisfied. One expects a primordial Universe with comparable baryon and anti-baryon abundances, both of the order of the photon density. Since $n_{\bar{B}}$ is now negligible if compared to n_B, one can read equation 2.54 as $\frac{n_B}{n_\gamma} \sim 3 \times 10^{-10}$, which is well below the primordial ratio (~ 1), but not zero. Excluding fine tuning solutions, with primordial baryon and anti-baryon abundances purposely tuned to produce the baryon asymmetry observed today, one has to admit a time evolution of the Universe favoring matter over antimatter, at least in our Universe region.

Experimentally, γ-telescopes like *Hess* try to measure bright γ sources at the boundary between matter and anti-matter universe regions, due to barion–anti-barion annihilation, furthermore the

search for anti-baryonic cosmic rays looks for anti-nuclei from stellar nucleosynthesis processes and measures the antiproton flux. At the time of writing no significative anti-nucleon has been detected in cosmic rays, nor any excess of anti-protons[3] has been measured. Hence, one can expect that the number of baryons is higher than the anti-baryon number in the whole Universe.

The most likely hypothesis is a modification of the $\Delta n_{Baryons}$ density during the Universe evolution. This requires the three assumptions by *Sakharov* (*Sakharov conditions*):

- Violation of Baryon Number, which is conserved in the Standard Model;
- C and CP violation;
- In the Universe evolution there have been interactions out of thermal equilibrium.

The second conditions allows the number of baryon to anti-baryon transitions to be smaller than the anti-baryon to baryon one. The third condition imposes an expansion sufficiently fast to avoid particle and its antiparticle to achieve thermal equilibrium allowing a time-reverse violation.

However the CP violation described in the CKM mechanism is not sufficient to explain the large baryonic asymmetry in the Universe.

If either mass matrix M^D or M^U had two or more degenerate eigenstates, or if one or more CKM mixing angles vanished then with a physically unobservable change of the quark fields phase, the CKM matrix would be made purely real, so that no CP violation would be admitted. In other words, if the combination

$$d_{CP} = \sin\theta_{12}\sin\theta_{23}\sin\theta_{13}\sin\theta_{\delta_{CP}}(m_t^2 - m_c^2)(m_t^2 - m_u^2)(m_c^2 - m_u^2)(m_b^2 - m_s^2)(m_b^2 - m_d^2)(m_s^2 - m_d^2) \tag{2.56}$$

vanished, then no CP violation would be possible. It is thus possible to argue that expression 2.56 is someway an estimation of CP violation magnitude. Quoting [28], "the 'conventional wisdom' that CP violation originating from the CKM phase is too small to be relevant to the observed baryonic asymmetry, results from arguing that the only natural scale for the baryogenesis problem is the temperature of the electroweak phase transition, $T \sim 100$ GeV. One might think that at this temperature the Yukawa interaction can be treated as a perturbation, because [light] quark masses are small compared with the temperature." Besides, below the electroweak phase transition temperature, the barionic number is known to be conserved. "Then, since the baryon asymmetry is a dimensionless number the quantity 2.56 should be divided by something with the dimension of $(\text{mass})^{12}$. The natural mass parameter at high temperatures seems to be the temperature itself, so that the asymmetry is argued to be at most"

$$\frac{n_B}{n_\gamma} \lesssim \frac{d_{CP}}{T^{12}} \sim 10^{-17} \tag{2.57}$$

"This reasoning is widely accepted, but, as it has been the case, with many 'no-go' theorems, it proves not to be watertight when examined carefully."

One can conclude that CKM mechanism CP violation is likely to be insufficient to explain baryogenesis.

2.3 Measuring the angle γ

The measurement of the γ angle is difficult because of the small branching fraction of the processes involved. However it is of fundamental importance in order to exclude any contribution from NP in the CKM model [3]. Since NP is expected to appear in loops as virtual particles if the energy is not high enough to produce real particles, the possibility of measuring γ in processes which do not involve loops (or *penguins*) assure that γ measured considering only processes completely described within the Standard Model, setting a very robust (theoretically speaking) reference for the global

[3]The observed $\bar{p}$ flux is consistent with their origin as products of cosmic rays proton-proton reactions with interstellar gas.

coherence test of the CKM mechanism within the Standard Model. At the same time, it is possible to measure γ in processes containing loops. New Physics would appear in a discrepancy between γ "with trees" (measured using tree-only processes) and γ measured in processes with loops, or in a discrepancy between γ with trees and its expected value $\pi-\alpha-\beta$. The latter would mean that NP contributions appear in the measurement of α and/or β which cannot exclude loop contributions in the decays.

Charmless two-body decays used to test γ with loops are beyond the interest of this report, an introductory overview can be found in [29].

There are mainly four methods to measure the angle γ with purely tree Feynman diagrams, without any contribution from loops: the Gronau-London-Wyler (GLW) [4] method uses $B^{\pm}$ meson decays to an open-charm final state $D^{(*)0}K$ with D^0 decaying to a CP eigenstate. The Atwood-Dunietz-Soni (ADS) method is based on the measurement of $B^{\pm}$ decays to $(K^{\mp}\pi^{\pm})_D K^{\pm}$ called *wrong sign* events because they are Doubly Cabibbo Suppressed. The branching ratio of these channels is even smaller, but the access to γ is better. The ADS method is complementary to the GLW analysis, adding additional constraints to the same parameters. Finally, the most modern method to measure γ in $B^{\pm} \to D^0 K^{\pm}$ decays is the Giri-Grossman-Soffer-Zupan (GGSZ) [22] method. It is often considered a generalization of ADS and GLW methods, but it studies three-body D decays on the Dalitz plot. At B-factories it provided the most precise measurement of γ, but at hadronic collider a more structured hadronic background is expected to make the measurement of γ harder than for other methods.

There is a fourth method to measure γ with trees, the time-dependent analysis of open charmed decays $B^0 \to D^{*\pm}\pi^{\mp}$ decays. This is also called indirect measurement of γ because the oscillation introduces a contribution from the β angle, so that the measured physical quantity is $\sin(2\beta+\gamma)$. Since the precision on β is sensibly better than the precision of γ this can be, *a priori*, an excellent method to access γ. However experimental difficulties and the impossibility to obtain a measurement not depending on New Physics (β is measured in processes including loops and penguins), strongly reduces the appeal of this method.

2.3.1 An useful geometrical relation

Before focalizing the attention on the experimental method to measure γ let me introduce a geometrical relation, useful to understand the principle underlying the methods. A more complete and less pedagogical exposition can be found in [30].

Let z_+ and z_- be complex quantities defined by

$$Z_+ = M_+ e^{i(\Delta+\varphi)} \qquad Z_- = M_- e^{i(\Delta-\varphi)} \tag{2.58}$$

Later, the phase φ will be identified with the weak phase, changing sign under CP-conjugation, and Δ with the strong phase, which does not change under CP-conjugation. I define

$$c_{\pm} \equiv \cos(\Delta \pm \varphi) = \frac{\Re\mathrm{e} Z_{\pm}}{|Z_{\pm}|} \quad ; \quad s_{\pm} \equiv \sin(\Delta \pm \varphi) = \frac{\Im\mathrm{m} Z_{\pm}}{|Z_{\pm}|} \tag{2.59}$$

Is not difficult to show that

$$\begin{aligned} \sin^2\varphi &= \frac{1}{2}\left(1 + s_+ s_- - c_+ c_-\right) \\ &= \frac{1}{2}\left(1 - c_+ c_- \pm \sqrt{(1-c_+^2)(1-c_-^2)}\right) \end{aligned} \tag{2.60}$$

so that calculating $\sin\varphi$ from $c_{\pm}$ introduces a four-fold ambiguity in the measurement.

2.3.2 Gronau-London triangular relation

Let f_D be a final state having the reconstructed invariant mass consistent with a D^0 meson.

Following the formal approach from [30], I introduce the neutral D meson state

$$|D_{into\ f}\rangle = c_f^* |D^0\rangle + \bar{c}_f^* |\overline{D}^0\rangle \tag{2.61}$$

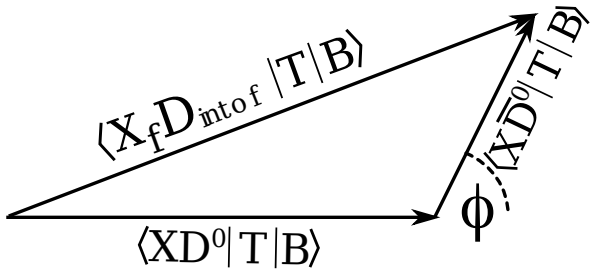

Figure 2.4: Gronau-London triangular relation on the complex plane.

$|D_{into\ f}\rangle$ is a generic superposition of the D^0 flavour eigenstates which decays in the final state $|f\rangle$. The ortogonal state $|D_{not\ into\ f}\rangle$ does not decay in $|f\rangle$. Its definition is

$$|D_{not\ into\ f}\rangle = \bar{c}_f|D^0\rangle - c_f|\overline{D}^0\rangle \tag{2.62}$$

where c_f and $\bar{c}_f$ are complex coefficients proportional to the probability amplitudes associated to a transition $D^0 \to f$ and $\overline{D}^0 \to f$, respectively. Naming the transition operator T, they are defined as

$$c_f = \xi\langle f|T|D^0\rangle \qquad \bar{c}_f = \xi\langle f|T|\overline{D}^0\rangle \qquad \text{normalised to } |c_f|^2 + |\bar{c}_f|^2 = 1 \tag{2.63}$$

where ξ is a normalisation constant. It is then evident that $|D_{not\ into\ f}\rangle$ cannot decay to f, in fact

$$\langle f|T|D_{not\ into\ f}\rangle = \xi\langle f|T|D^0\rangle\langle f|T|\overline{D}^0\rangle - \xi\langle f|T|\overline{D}^0\rangle\langle f|T|D^0\rangle = 0 \tag{2.64}$$

Considering the generic decay chain

$$B \to XD_{into\ f} \to Xf \tag{2.65}$$

and neglecting any contribution from D^0 mixing, we can write

$$\langle Xf|T|B\rangle \propto \langle XD^0_{intof}|T|B\rangle = c_f\langle XD^0|T|B\rangle + \bar{c}_f\langle X\overline{D}^0|T|B\rangle \tag{2.66}$$

This relation can be represented in the complex plane as a triangle. It is thus called Gronau-London (GL) triangular relation and it is the theoretical basis for the GLW and ADS methods. A schematic representation of the triangular relation in the complex plane is given in figure 2.4. Where ϕ is the phase difference between $\langle XD^0|T|B\rangle$ and $\langle X\overline{D}^0|T|B\rangle$.

2.3.3 Gronau-London-Wyler method: first formulation

The method which can immediately apply the Gronau-London triangular relation to a physical decay is the Gronau-London-Wyler method, choosing $|D_{into\ f}\rangle$ as a CP eigenstate. Both CP-even and CP-odd final states can be used. $|D_{into\ f}\rangle$ CP-even eigenstates are named $|D_{CP+}\rangle$ and are usually reconstructed as K^+K^- or $\pi^+\pi^-$ D decays. $|D_{into\ f}\rangle$ CP-odd eigenstates are named $|D_{CP-}\rangle$ and reconstructed in a pair of neutral mesons one of which being a short kaon K^0_s: $K^0_s\pi^0$, $K^0_s\eta$, $K^0_s\eta'$, $K^0_s\omega$ and $K^0_s\phi$, are typical signatures for a CP-odd $|D^0_{CP-}\rangle$ eigenstate.

Excluding D^0 oscillation, and considering the case $|D_{into\ f}\rangle \equiv |D_{CP+}\rangle$, one can write

$$|D_{into\ f}\rangle \equiv |D_{CP+}\rangle = \frac{1}{\sqrt{2}}\left(|D^0\rangle + |\bar{D}^0\rangle\right) \quad ; \quad |D_{not\ into\ f}\rangle \equiv |D_{CP-}\rangle = \frac{1}{\sqrt{2}}\left(|D^0\rangle - |\bar{D}^0\rangle\right) \tag{2.67}$$

Considering the $B^- \to K^-D_{CP+}$ the GL triangular relation becomes

$$\langle K^-D_{CP+}|T|B^-\rangle = \frac{1}{\sqrt{2}}\langle K^-D^0|T|B^-\rangle + \frac{1}{\sqrt{2}}\langle K^-\bar{D}^0|T|B^-\rangle \tag{2.68}$$

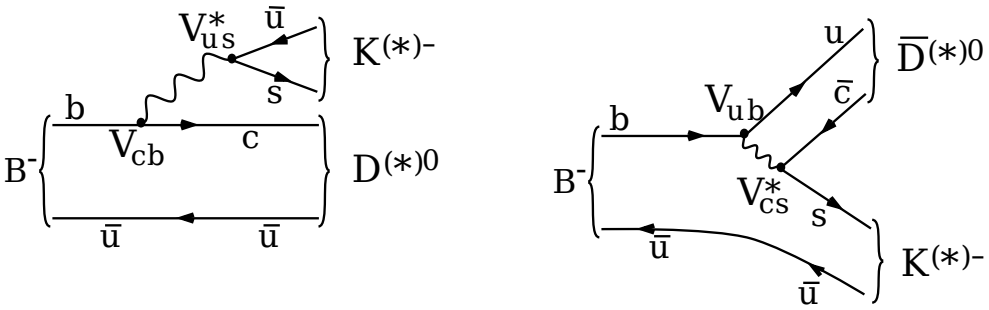

Figure 2.5: Feynman diagrams of charged B meson decays used in the measurement of γ. The left diagram is favored by a factor ~ 10 compared to the right one.

where T is the transition operator. Equation (2.68) can also be written in the form

$$A(B^- \to K^- D_{CP+}) = \frac{1}{\sqrt{2}} \left[A(B^- \to K^- D^0) + A(B^- \to K^- \bar{D}^0) \right] \tag{2.69}$$

It is thus evident that the phase difference between the two transition amplitudes $A(B^- \to K^- D^0)$ and $A(B^- \to K^- \bar{D}^0)$ influence significantly the partial width decay $\Gamma = |\sum A|^2$ of the $B^- \to K^- D_{CP+}$ decay channel. The next step is to show that the relative phase between the two diagrams depends on γ and to find the relation between the squared amplitudes of the three processes put in relation in equation (2.69) and γ.

If one considers the two B decays to DK final states shown in figure 2.5, one can observe that relative electroweak phase, coming from CKM matrix elements only, is

$$\varphi = \arg \left[\frac{V_{us} V_{cb}^*}{V_{cs} V_{ub}^*} \right] \tag{2.70}$$

With a little complex algebra it is possible to show that

$$\varphi = -\arg \left[-\frac{V_{ud} V_{ub}^*}{V_{cd} V_{cb}^*} \right] - \arg \left[-\frac{V_{cs} V_{cd}^*}{V_{us} V_{ud}^*} \right] = -\gamma - \epsilon' \simeq -\gamma \tag{2.71}$$

where ϵ' is the quasi-null angle ($\sim 10^{-6}$ rad) of the ds triangle, negligible if compared to γ in absence of NP, indeed D^0 mixing and D^0 CP violation can be neglected to an excellent accuracy. It is then a geometrical exercise to extract the γ angle from the decay widths, the only experimental observables, and then the lengths of the triangle sides. The same calculation for B^+ decays gives $\simeq +\gamma$, because CP conjugation acts on the Lagrangian as a complex conjugation.

There is another contribution to the phase, due to the strong interaction. Quarks live in a hadronic environment so that strong final state re-scattering and QCD contribution can add a phase contribution. This effect is well known in nuclear physics by the name "final state phase shift". These phases are the same for CP-conjugate states. There are other phase sources due to helicity projectors in Feynman diagram calculation, which, as QCD phases, do not change under CP-conjugation. A more detailed treatment of strong phases is given in [30]. All the relative phase contributions unaffected by CP-conjugation are summarized in a *relative strong phase* δ_B.

Considering the Feynman diagrams in figure 2.5, the left diagram is favored with respect to the right one by a factor ~ 10 in the amplitude, indeed the second channel is both Cabibbo and color suppressed. Color suppression is a constraint on the color of the produced quark pair: it has to be the same of quarks constituting the meson B. For example, if the B constituting quarks are red–anti-red, thus the produced pair has to be red–anti-red. If that is not the case, daughter particles could not be color singlets and therefore could not exist. The color suppression is a difficult theoretical problem involving non perturbative QCD, but it can be taken into account by a phenomenological factor $a_2/a_1 \sim 0.2$ [31].

Defining

$$a \equiv |A(B^- \to K^- D^0)| = |A(B^+ \to K^+ \bar{D}^0)| \qquad \text{(favored decays)} \tag{2.72}$$

and

$$ar_B \equiv |A(B^- \to K^- \bar{D}^0)| = |A(B^+ \to K^+ D^0)| \qquad \text{(suppressed decays)} \tag{2.73}$$

one can choose by convention that

$$\arg\Big[A(B^- \to K^- D^0)\Big] = \arg\Big[A(B^+ \to K^+ \bar{D}^0)\Big] \equiv 0 \tag{2.74}$$

and write

$$A(B^- \to K^- \bar{D}^0) = a e^{i(\delta_B - \gamma)} \qquad A(B^+ \to K^+ D^0) = a e^{i(\delta_B + \gamma)} \tag{2.75}$$

Representing the GL triangular relation in the complex plane one gets the figure 2.6, in formulae the triangular relation for B^+ decays can be written as

$$\begin{aligned} A(B^+ \to D^0_{CP+} K^+) &= \frac{1}{\sqrt{2}}\Big[A(B^+ \to \bar{D}^0 K^+) + A(B^+ \to D^0 K^+)\Big] \\ &= \frac{1}{\sqrt{2}}\Big(a + a r_B e^{i\gamma} e^{i\delta_B}\Big) \end{aligned} \tag{2.76}$$

while for B^- decays is

$$\begin{aligned} A(B^- \to D^0_{CP+} K^-) &= \frac{1}{\sqrt{2}}\Big[A(B^- \to \bar{D}^0 K^-) + A(B^- \to D^0 \to K^-)\Big)] \\ &= \frac{1}{\sqrt{2}}\Big(a + a r_B e^{-i\gamma} e^{i\delta_B}\Big) \end{aligned} \tag{2.77}$$

It is then possible to calculate squared amplitudes or decay widths as

$$\begin{aligned} \Gamma(B^+ \to D^0_{CP+} K^+) &= \frac{1}{2}|a + a r_B e^{i\gamma} e^{i\delta_B}|^2 \\ &= \frac{1}{2}\Big(a^2 + a^2 r_B^2 + 2a^2 r_B \cos(\delta_B + \gamma)\Big) \end{aligned} \tag{2.78}$$

analogously

$$\begin{aligned} \Gamma(B^- \to D^0_{CP+} K^-) &= \frac{1}{2}|a + a r_B e^{-i\gamma} e^{i\delta_B}|^2 \\ &= \frac{1}{2}\Big(a^2 + a^2 r_B^2 + 2a^2 r_B \cos(\delta_B - \gamma)\Big) \end{aligned} \tag{2.79}$$

For CP-odd eigenstates one could write

$$\begin{aligned} \Gamma(B^+ \to D^0_{CP-} K^+) &= \frac{1}{2}|a - a r_B e^{i\gamma} e^{i\delta_B}|^2 \\ &= \frac{1}{2}\Big(a^2 + a^2 r_B^2 - 2a^2 r_B \cos(\delta_B + \gamma)\Big) \end{aligned} \tag{2.80}$$

and

$$\begin{aligned} \Gamma(B^- \to D^0_{CP-} K^-) &= \frac{1}{2}|a - a r_B e^{-i\gamma} e^{i\delta_B}|^2 \\ &= \frac{1}{2}\Big(a^2 + a^2 r_B^2 - 2a^2 r_B \cos(\delta_B - \gamma)\Big) \end{aligned} \tag{2.81}$$

Calling two generic complex numbers z_1 and z_2, their sum z and their relative phase θ, one can easily show that

$$\cos\theta = \frac{|z|^2 - |z_1|^2 - |z_2|^2}{2|z_1||z_2|} \tag{2.82}$$

Applying equation 2.82 to the GLW, CP-even triangles (see figure 2.6) one gets

$$\cos(\delta_B \pm \gamma) = \frac{2\Gamma(B^\pm \to D^0_{CP+} K^\pm) - \Gamma(B^\pm \to D^0 K^\pm) - \Gamma(B^\pm \to \bar{D}^0 K^\pm)}{2\sqrt{\Gamma(B^\pm \to D^0 K^\pm)\Gamma(B^\pm \to \bar{D}^0 K^\pm)}} \tag{2.83}$$

Using equation 2.60, it is then easy to find γ.

However, even if this first formulation of the GLW method is *formally* sufficient to measure γ, experimental difficulties forced Gronau, London and Wyler to introduce a second, experimentally applicable formulation.

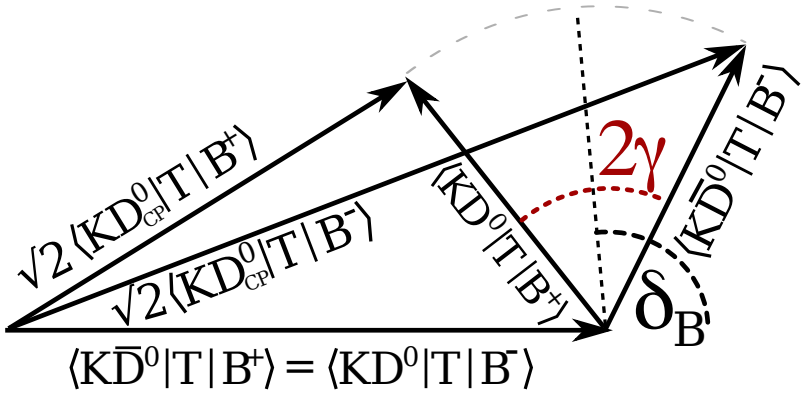

Figure 2.6: Representation on the complex plane of the relations between the CP and flavour decay amplitudes for B^+ and its CP-conjugate B^-. The common strong phase is named δ_B while the opposite weak phase is indicated as γ.

Experimental difficulties with the first formulation of the GLW method

The measurement of γ through the first formulation of the GLW method requires the measurement of the decay width

$$\Gamma\left(B^- \to \bar{D}^0 K^- \text{ with } \bar{D}^0 \to (K^+\pi^-)\right) \qquad (\text{“wrong sign” events}) \tag{2.84}$$

and its CP-conjugate. Experimentally this is a very hard task because of the pollution from another channel giving the same final state:

$$\Gamma\left(B^- \to D^0 K^- \text{ with } D^0 \to (K^+\pi^-)\right) \tag{2.85}$$

Calculating the ratio

$$\frac{\Gamma\left(B^- \to \bar{D}^0 K^- \text{ with } \bar{D}^0 \to (K^+\pi^-)\right)}{\Gamma\left(B^- \to D^0 K^- \text{ with } D^0 \to (K^+\pi^-)\right)} \sim \left|\frac{V_{ub}V_{cs}^*}{V_{cb}V_{us}^*}\right| \left|\frac{a_2}{a_1}\right|^2 \frac{Br(\bar{D}^0 \to K^+\pi^-)}{Br(D^0 \to K^+\pi^-)} \tag{2.86}$$

with the CKM matrix elements ratio

$$\left|\frac{V_{ub}V_{cs}^*}{V_{cb}V_{us}^*}\right| \sim 0.4 \tag{2.87}$$

the phenomenological color suppression [31] coefficient

$$\frac{a_2}{a_1} \sim 0.2 \tag{2.88}$$

and the D branching fraction ratio [24]

$$\frac{Br(D^0 \to K^+\pi^-)}{Br(\bar{D}^0 \to K^+\pi^-)} = (3.8 \pm 0.2)\ 10^{-3} \tag{2.89}$$

one concludes that the ratio in equation (2.86) is of the order of one, in other words the two channel have the same final state and the same decay width. Thus, $B^- \to D^0 K^- \to (K^+\pi^-)K^-$ channel constitutes a unavoidable background source for the channel $B^- \to \bar{D}^0 K^- \to (K^+\pi^-)K^-$ (required to extract γ), making the measurement impossible, and the GLW method experimentally inapplicable.

2.3.4 Gronau-London-Wyler method: second formulation

A second formulation of the GLW method is based on the measurement of $B \to D^0_{CP\_}K$ decays to add constraints to the measurement of the angle γ. As previously stated, the CP-even D^0

decay modes are $D^0_{CP+} \to K^\pm K^\mp$ and $D^0_{CP+} \to \pi^\pm \pi^\mp$, while the CP-odd modes are $D^0 \to K^0_s\{\pi^0, \eta, \eta', \omega, \phi\}$.

This reformulation of the GLW method proposes the evaluation of the CP asymmetry and the CP ratio, namely

$$\mathcal{A}_{CP\pm} = \frac{\Gamma(B^- \to D^0_{CP\pm}K^-) - \Gamma(B^+ \to D^0_{CP\pm}K^+)}{\Gamma(B^- \to D^0_{CP\pm}K^-) + \Gamma(B^+ \to D^0_{CP\pm}K^+)} \tag{2.90}$$

and

$$\mathcal{R}_{CP_\pm} = \frac{\Gamma(B^- \to D^0_{CP\pm}K^-) + \Gamma(B^+ \to D^0_{CP\pm}K^+)}{\frac{1}{2}\{\Gamma(B^- \to D^0K^-) + \Gamma(B^+ \to \overline{D}^0K^+)\}} \tag{2.91}$$

Starting from equation 2.78, 2.79, 2.80 and 2.81 it is easy to show that

$$\mathcal{A}_{\mathcal{CP}\pm} = \frac{\pm 2 r_B \sin\delta_B \sin\gamma}{1 + r_B^2 \pm 2 r_B \cos\delta_B \cos\gamma} \qquad R_{CP\pm} = 1 + r_B^2 \pm 2 r_B \cos\delta_B \cos\gamma \tag{2.92}$$

Even if r_B and δ_B are of no interest, it is impossible to achieve a good measurement of γ without a precise determination of these two parameters. For this reason they are called *nuisance parameters* and many methods for the measurement of γ are applied at the same time: even if some method shows a limited precision in the measurement of the angle, the information on r_B and δ_B can be shared with other methods more sensible on γ. In particular the GLW method suffers from the smallness of r_B and from its low precision. For this reason it is always coupled with the Atwood-Dunietz-Soni (ADS) method which presents a better resolution in r_B thanks to a sizeable interference term as I discuss in the next section.

Another problem with the GLW method is the smallness of the branching ratios of D to CP eigenstates:

$$\mathcal{B}r(B \to D^0K) \times \mathcal{B}r(D^0 \to f_{CP}) \sim 10^{-6} \tag{2.93}$$

For this reason a sizeable production of $b\bar{b}$ pairs is required to achieve a good measurement of γ.

Finally, since $\mathcal{R}_{CP\pm}$ is a ratio of squared amplitudes measured with different analyses, the differences in the event reconstruction, in the trigger and in the selection may introduce strong systematic errors. The problem can be partially solved calculating $\mathcal{R}_{CP}$ as a double ratio

$$\mathcal{R}_{CP\pm} \simeq \frac{R_\pm}{R} \tag{2.94}$$

where

$$R_\pm = \frac{\Gamma(B^- \to D^0_{CP\pm}K^-) + \Gamma(B^+ \to D^0_{CP\pm}K^+)}{\Gamma(B^- \to D^0_{CP\pm}\pi^-) + \Gamma(B^+ \to D^0_{CP\pm}\pi^+)} \tag{2.95}$$

$$R = \frac{\Gamma(B^- \to D^0K^-) + \Gamma(B^+ \to \overline{D}^0K^+)}{\Gamma(B^- \to D^0\pi^-) + \Gamma(B^+ \to \overline{D}^0\pi^+)} \tag{2.96}$$

the approximation 2.94 requires the assumption

$$\Gamma(B^- \to D^0_{CP\pm}\pi^-) + \Gamma(B^+ \to D^0_{CP\pm}\pi^+) \simeq \frac{1}{2}[\Gamma(B^- \to D^0\pi^-) + \Gamma(B^+ \to \overline{D}^0\pi^+)] \tag{2.97}$$

which is justified by considering the decay amplitude

$$A(B^+ \to D^0_{CP\pm}\pi^+) \simeq A(B^- \to D^0_{CP\pm}\pi^-) = \frac{1}{\sqrt{2}}[A(B^- \to D^0\pi^-) + A(B^- \to \overline{D}^0\pi^-)] \tag{2.98}$$

In fact

$$\begin{aligned}\Gamma(B^- \to D^0_{CP\pm}\pi^-) &= \left|A(B^- \to D^0_{CP\pm}\pi^-)\right|^2 = \left|\frac{1}{\sqrt{2}}[A(B^- \to D^0\pi^-) + A(B^- \to \overline{D}^0\pi^-)]\right|^2 \\ &= \frac{1}{2}\Gamma(B^- \to D^0\pi^-)\left|1 + \frac{A(B^- \to \overline{D}^0\pi^-)}{A(B^- \to D^0\pi^-)}\right|^2 \end{aligned} \tag{2.99}$$

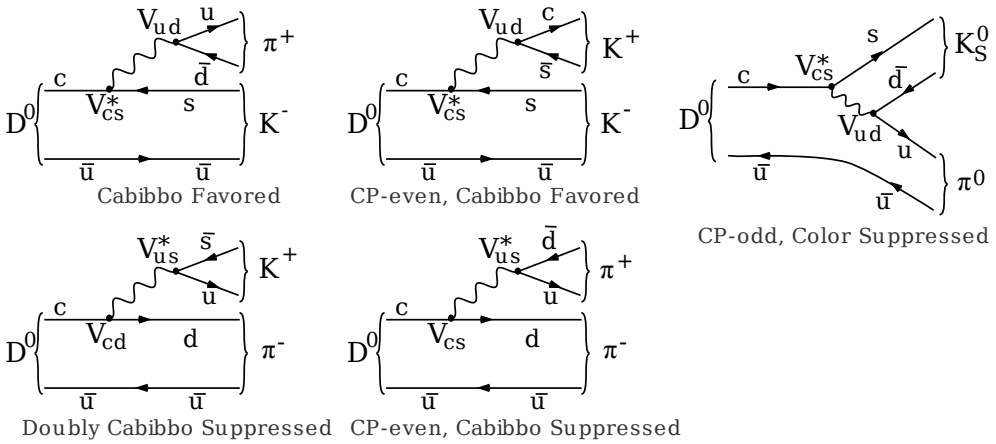

Figure 2.7: Table of the various D decays involved in GLW and ADS methods.

Since the ratio $\mathcal{A}(B^- \to \overline{D}^0\pi^-)/A(B^- \to D^0\pi^-)$ is of the order of 0.5 %, the approximation 2.94 is good at 1% level, well below the current precision on γ.

The branching ratio of $B^\pm \to D^0\pi^\pm$ channels is higher compared to analogous $B^\pm \to D^0K^\pm$ decays, therefore they are used as *normalization channels*, since most of the analysis is the same for $D^0K^\pm$ and $D^0\pi^\pm$ channels. The analysis parameters (except the hadron identification) can be tuned on the high statistics channel and then used on the physically interesting channel. Hence, the first step of a GLW analysis is often the characterization of normalization channels.

The various D decays involved in the GLW method (first and second formulation) are shown in figure 2.7.

2.3.5 Atwood-Dunietz-Soni (ADS) method

As discussed above, the yields for "wrong sign" events coming from Cabibbo Favoured and Doubly Cabibbo Suppressed D decays are of the same order of magnitude. This can be exploited to extract information from the interference between the two channels. In contrast with the GLW method, this technique introduced by Atwood, Dunietz and Soni [5] is very sensitive to r_B thanks to its sizable contribution to the interference. The physical observables are the ADS ratio and the ADS asymmetry, defined as

$$R_{ADS} = \frac{\Gamma(B^- \to D(K^+\pi^-)K^-) + \Gamma(B^+ \to D(K^-\pi^+)K^+)}{\Gamma(B^- \to D(K^-\pi^+)K^-) + \Gamma(B^+ \to D(K^+\pi^-)K^+)} \tag{2.100}$$

$$A_{ADS} = \frac{\Gamma(B^- \to D(K^+\pi^-)K^-) - \Gamma(B^+ \to D(K^-\pi^+)K^+)}{\Gamma(B^- \to D(K^+\pi^-)K^-) + \Gamma(B^+ \to D(K^-\pi^+)K^+)} \tag{2.101}$$

With some algebra it is possible to show that

$$R_{ADS} = r_B^2 + r_D^2 + 2r_Br_D\cos\gamma\cos(\delta_B+\delta_D) \qquad A_{ADS} = \frac{2r_Br_D\sin(\delta_B+\delta_D)\sin\gamma}{r_B^2 + r_D^2 + 2r_Br_D\cos\gamma\cos(\delta_B+\delta_D)} \tag{2.102}$$

where r_B and δ_B are the same parameters as before, while r_D and δ_D are the analogous parameters for the D decay. δ_D is the strong phase difference between the Doubly Cabibbo Suppressed and the Cabibbo Favoured D decays while r_D is the ratio between the two amplitudes.

r_D has been measured by charm dedicated experiments, the current world average is $r_D^2 = \frac{\Gamma(D^0\to K^-\pi^+)}{\Gamma(D^0\to K^+\pi^-)} = (0.337\pm0.009)\%$ [24]. δ_D can be extracted from current CLEOc data and additional global fit in D^0-$\overline{D}^0$ mixing as performed by HFAG [32] constraining δ_D to $(22.0^{+9.8}_{-11.2})^\circ$.

If compared to $R_{CP\pm} \sim 1 + r_B^2$, the measurement of R_{ADS} offers a better access to r_B because the collateral constant r_D^2 is smaller than one. However, since the system presents two equations but four unknowns, this method can be only used as a support for the GLW method. Additional

constraints can be added by the ADS method applied to the channel $B^{\pm} \to D^{*0}K^{\pm}$ [33]. D^{*0} is a resonance which decays to $D^0\pi^0$ or $D^0\gamma$. Since the neutral pion has J^{PC} quantum numbers of 0^{-+}, and the photon 1^{--}, the CP eigenvalues of the D^0 meson in the final state of the two possible D^{*0} decays are different. The price to pay for using D^{*0} channel is the presence of r_B^* and δ_B^*, two additional nuisance parameters different from the ones related to $B \to DK$ channels.

Considering the CP eigenvalues η, concerning the $D^{*0} \to D^0\pi^0$ decays in the D^{*0} rest frame, one gets

$$\begin{aligned}
\eta_{D^*} &= \eta_{D^0}\eta_{\pi^0}(-1)^{\ell} && (\ell \text{ is the final state angular momentum, it equals } D^{*0} \text{ spin: } \ell = 1)\\
&= -\eta_{D^0}\eta_{\pi^0} && (\text{the pion is a pseudo-scalar meson: } J^{PC} = 0^{-+}. \text{ Hence } \eta_{\pi^0} = -1)\\
&= \eta_{D^0} &&
\end{aligned} \tag{2.103}$$

which means that the D^{*0} and D^0 mesons have the same CP eigenvalue. If one writes the $|\tilde{D}^{*0}\rangle$ state of a D^0 coming from a $B^{\pm} \to \tilde{D}^{*0}K^{\pm}$ decay as

$$\begin{aligned}
|\tilde{D}^{*0}\rangle &= \frac{1}{\sqrt{1+r_B^{*2}}}\left(|D^{*0}\rangle + r_B^* e^{i(\delta_B^* - \gamma)}|\bar{D}^{*0}\rangle\right)\\
&= \frac{1}{\sqrt{1+r_B^{*2}}}\left(\frac{|D^{*0}_{CP+}\rangle + |D^{*0}_{CP-}\rangle}{\sqrt{2}} + r_B^* e^{i(\delta_B^* - \gamma)}\frac{|D^{*0}_{CP+}\rangle - |D^{*0}_{CP-}\rangle}{\sqrt{2}}\right)
\end{aligned} \tag{2.104}$$

the D^0 state coming from $D^*_{CP\pm} \to D_{CP\pm}\pi^0$ decays can be written as

$$\begin{aligned}
|\tilde{D}^{0}\rangle &= \frac{1}{\sqrt{1+r_B^{*2}}}\left(\frac{|D^{0}_{CP+}\rangle + |D^{0}_{CP-}\rangle}{\sqrt{2}} + r_B^* e^{i(\delta_B^* - \gamma)}\frac{|D^{0}_{CP+}\rangle - |D^{0}_{CP-}\rangle}{\sqrt{2}}\right)\\
&= \frac{1}{\sqrt{1+r_B^{*2}}}\left(|D^{0}\rangle + r_B^* e^{i(\delta_B^* - \gamma)}|\bar{D}^{0}\rangle\right)
\end{aligned} \tag{2.105}$$

For $D^{*0} \to D^0\gamma$ decays, considering that only odd-ℓ solution are allowed by parity P conservation,

$$\eta_{D^{*0}} = \eta_{D^0}\eta_{\gamma}(-1)^{\ell} = -\eta_{D^0} \tag{2.106}$$

Since the γ CP eigenvalue, $D^*_{CP\pm}$ decays to $D_{CP\mp}\gamma$. The D^0 state can be written as

$$\begin{aligned}
|\tilde{D}^{0}\rangle &= \frac{1}{\sqrt{1+r_B^{*2}}}\left(\frac{|D^{0}_{CP-}\rangle + |D^{0}_{CP+}\rangle}{\sqrt{2}} + r_B^* e^{i(\delta_B^* - \gamma)}\frac{|D^{0}_{CP-}\rangle - |D^{0}_{CP+}\rangle}{\sqrt{2}}\right)\\
&= \frac{1}{\sqrt{1+r_B^{*2}}}\left(|D^{0}\rangle - r_B^* e^{i(\delta_B^* - \gamma)}|\bar{D}^{0}\rangle\right)
\end{aligned} \tag{2.107}$$

The expressions for R_{ADS} in the two cases are

$$R^{\pi^0}_{ADS} = r_B^{*2} + r_D^2 + 2r_B^* r_D \cos(\delta_B^* + \delta_D)\cos\gamma \tag{2.108}$$

$$R^{\gamma}_{ADS} = r_B^{*2} + r_D^2 - 2r_B^* r_D \cos(\delta_B^* + \delta_D)\cos\gamma \tag{2.109}$$

for $D^{*0} \to D^0\pi$ and $D^{*0} \to D^0\gamma$, respectively. The experimental difficulty measuring the D^{*0} decays comes from the reconstruction of the neutral particle (photon or pion). The detection and reconstruction of these particles is obtained using electromagnetic calorimeter only, which offers an angular resolution much worse than any tracking system. I will discuss these sub-detectors in the next chapter.

2.3.6 The Giri-Grossman-Soffer-Zupan (GGSZ) method. Dalitz plot analysis

So far, the most efficient method to measure γ is the GGSZ method [22], which exploits a bidimensional fit on the Dalitz plot of three-body D decays to extract the angle γ. It is currently applied at B-factories.

The most interesting channel is the decay $B^{\pm} \to D^0 K^{\pm}$ with D^0 decaying to $K_S \pi^+ \pi^-$.

To the first order, this method mixes the principles of GLW and ADS methods, since CP and doubly Cabibbo suppressed states can also be accessed as particular cases of three-body D decays.

In the GGSZ method a D^0 decay strong phase is present, analogous to the δ_D phase in the ADS method, which varies strongly over the Dalitz plane. It is thus necessary to provide the relative value of this strong Dalitz phase with respect to a reference (usually $K_s \rho^0(\pi\pi)$), as an external input to the bidimensional fit. As for δ_D, the values of these phases have been obtained at c-factories.

In addition to this difficulty, at LHCb the resonance-structured background is not negligible nor well modeled, hence it can introduce a sizable systematics error in particular in the determination of the strong phase. Such a problem is much less important at BaBar and Belle.

2.3.7 Neutral B meson oscillation. Indirect measurement.

An alternative to the study of charged B meson decays is offered by the time-dependent B^0 decay analysis. The decays considered in the analysis are $B^0 \to D^- \pi^+$ and $\overline{B}^0 \to D^- \pi^+$. Since B^0 mesons can oscillate through box diagrams, also the channels $\overline{B}^0 \to B^0 \to D^- \pi^+$ and $B^0 \to \overline{B}^0 \to D^- \pi^+$ have to be considered.

The measured quantity is found to be $\sin(2\beta + \gamma)$, where the β contribution arises from oscillations. *A priori* this measurement can be as precise as the direct measurement of γ, because the β angle has been measured with a precision well beyond the current γ resolution. However, since the measurement of β is based on penguin diagrams, this measurement of γ cannot exclude contributions from New Physics. Furthermore there are experimental difficulties in tagging the hadrons, which made this method inefficient for experiments at B-factories.

Chapter 3

The Large Hadron Collider and the LHCb experiment

In the previous section, I have theoretically discussed the techniques to measure the angle γ. Since the physical observables are ratios and asymmetries it is evident that, neglecting systematics, a higher statistics allows a better precision on the observables and therefore on γ. In order to increase statistics one needs particle accelerators able to produce $b\bar{b}$ pairs at a much higher rate than present B-factories. Hence, Super B-factories are being studied to build up two electron-positron colliders in Italy and Japan which would increase significantly the luminosity compared to PEP-II and KEK-II, the e^+e^- colliders exploited by Babar and Belle experiments. But, at the moment, the highest $b\bar{b}$ production rate is offered by the Large Hadron Collider (LHC) developed at CERN: a proton-proton collider which has reached a center-of-mass energy $\sqrt{s} = 7$ TeV, and has been designed to reach 14 TeV in three years. The high $b\bar{b}$ cross section at these high energies is not sufficient to obtain a large $b\bar{b}$ statistical sample, indeed the angular distribution of $b\bar{b}$ pairs is peaked in the forward and in the backward regions, in part very closed to the proton beams. Increasing efficiency in these regions means to increase counting rates due to beam halos, thus the general purpose detectors often do not care of these regions. LHC has thus devolved an experiment to the analysis of the forward region to study b physics and CP violation in B mesons. It is named LHCb, the Large Hadron Collider beauty experiment. LHCb is specialized in the reconstruction of $b\bar{b}$ events, with a geometrical acceptance reaching a very small polar angle (measured with respect to one of the beams).

To face the high counting rate of such regions, with limited tape recording bandwidth, an excellent trigger is required. In order to reduce the hadronic background a precise vertex reconstruction is needed, indeed b mesons are identified by their characteristic flight distance (~ 7 mm in average at LHCb).

In this chapter I briefly describe the LHC machine and the LHCb detector.

3.1 The Large Hadron Collider

The *Large Hadron Collider* (LHC) is a proton-proton and heavy ion (lead) collider at CERN. It is located at the French-Swiss border, in a 27 km long tunnel which contains two beam pipes for the two particle beams accelerated in opposite directions. The choice of using proton-proton collisions allows LHC to reach a high luminositybecause it is not required to produce anti-protons to be used in the collisions. LHC is keeping to deliver a luminosity close to $2 \times 10^{33}\text{cm}^{-2}\text{s}^{-1}$, the applied filling scheme has 1380 bunches per beam. It is the originality of LHC superconducting bending magnets to have the two beams bent and circulating in opposite directions in the same structure. This achievement has been possible also thanks to the magnetic return flux structure. It is the sizable bending power of the magnets which will allow LHC to reach 7 TeV per beam, and a $\sqrt{s}$ value of 14 TeV.

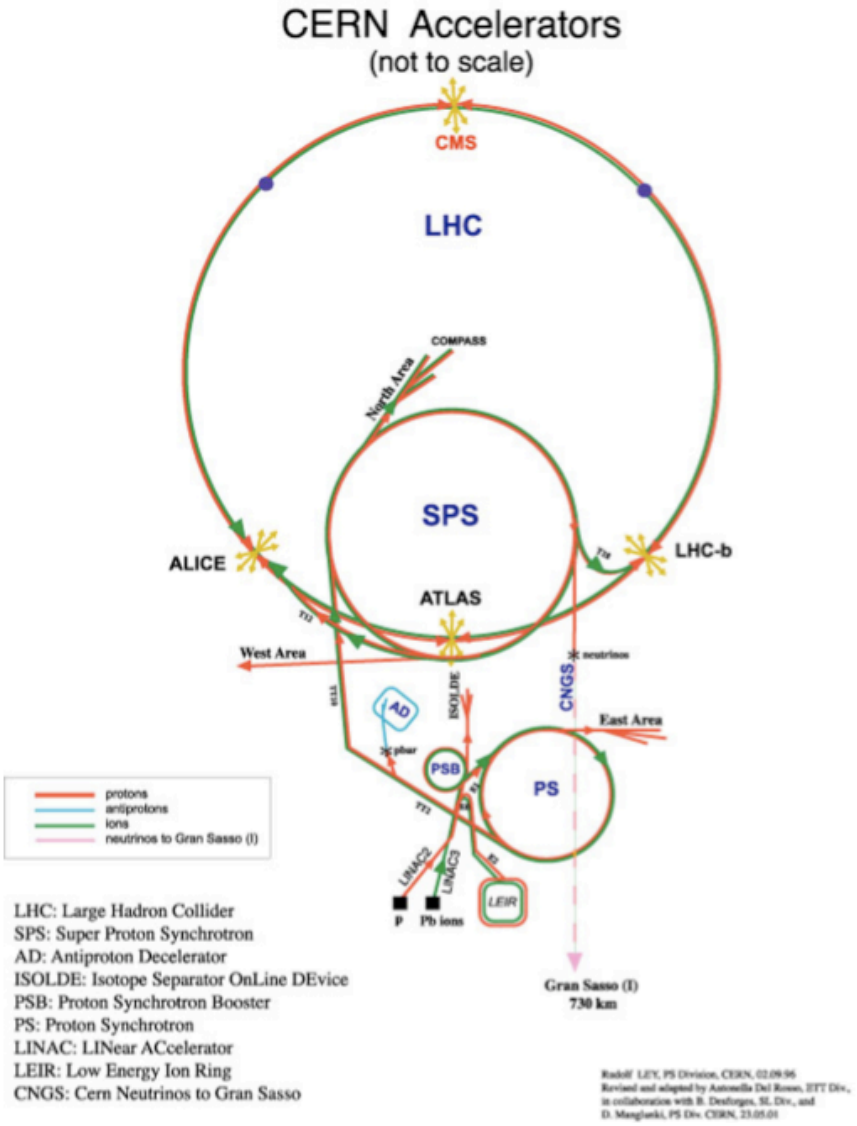

Figure 3.1: Schematic representation of the CERN accelerator system.

3.1.1 The LHC accelerator system

The LHC is not the only accelerators at CERN, and it is served by other smaller and less powerful CERN accelerator which gradually accelerate protons up to 540 GeV before transferring them to the LHC storage rings, where they are further accelerated for about 20 minutes before reaching the operational energy. In figure 3.1, a schematic representation of the accelerators complex of CERN is shown.

For the first acceleration stage a linear accelerator, called LINAC2, is sufficient. The second stage is provided by the Proton Synchrotron Booster which injects protons in the Proton Synchrotron (PS). The PS accelerates protons up to an energy of 25 GeV. The Super Proton Synchrotron, famous because of the discovery of $W^{\pm}$ and Z^0 bosons, brings the energy up to 540 GeV, protons can then be extracted for fixed target experiments or to be injected in the LHC storage rings. Many experimental activities are possible thanks to the various accelerators, only a short summary at LHC performances and of its larger experiments will be included in this thesis.

3.1.2 The large experiments at the LHC

There are four large experiments exploiting the LHC proton-proton collisions. CMS (*Compact Muon Solenoid*) is a general purpose experiment whose detector is composed of various concentrical sub detectors around the interaction point. The detector is subdivided in three parts, two end-cups

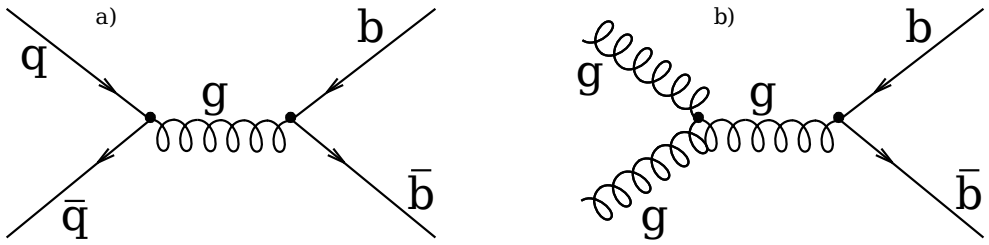

Figure 3.2: $s-$ way Feynman diagrams for two concurrent $b\bar{b}$ production at the leading order. The diagram a) dominates at low energy, at the energy of LHC the diagram b) dominates. t- and u-way diagrams only exist for $gg \to b\bar{b}$ diagrams.

and a cylindrical part. It contains a superconducting solenoidal magnet generating a magnetic field of 3.8 T, this allows a very compact structure and motivates the experiment name. The whole detector is 12 500 tons heavy. One of the main aims of CMS is the Higgs boson search, but also precision measurement to study top and bottom physics are possible.

The other general purpose detector of LHC is ATLAS (A Toroidal LHC ApparatuS). It is 46 meters long with a diameter of 25 meters and a weight of 7 000 tons. It is the largest collider experiment ever built and the ATLAS collaboration is the largest scientific collaboration in the world. Among the aims of ATLAS there is the search of the Higgs boson and supersymmetric particle candidates.

ALICE (A Large Ion Collider Experiment) exploits heavy ion (Pb-Pb) collisions at LHC. ALICE aims to study nuclear matter at high temperature and pressure and look for quark-gluon plasma, a phase where quarks are expected not to be confined inside hadrons and the QCD to become perturbative.

Finally LHCb, described in some detail in the next section, is the only experiment at LHC mainly devolved to precision measurement aiming to an indirect search for New Physics. While CMS and ATLAS search for New Physics signature as peaks in the reconstructed masses of expected particles in some well defined decay channels, LHCb tries to put in evidence discrepancies in the Standard Model which could be an evidence for New Physics arising in loop processes or unexpected diagrams.

3.1.3 The $b\bar{b}$ production cross section

The $b\bar{b}$ production cross section depends on the energy and increases significantly with the center-of-mass energy. Since LHC uses pp collisions, one could expect the $b\bar{b}$ cross section to be reduced since the s-way Feynman diagram with interacting quarks (figure 3.2.a) is suppressed in pp collisions. Indeed, only Dirac sea antiquarks are available. But, at LHC energy, gluon fusion diagram (figure 3.2.b) dominates, and t- and u-ways Feynman diagrams only exist for gluon-gluon interaction; therefore production cross section in pp collision are not significantly smaller than in $p\bar{p}$ collisions.

The cross-sections of various processes as functions of the center-of-mass energy $\sqrt{s}$ are presented in figure 3.3 for a comparison between TeVatron and LHC. As usual, cross-section are expressed in barn sub-multiples. A barn b equals 10^{-28} m^2, sub-multiples from millibarn (mb) to attobarn (ab $= 10^{-18}$ b) are often used.

The $b\bar{b}$ production cross section at TeVatron ($\sqrt{s} = 1.96$ TeV) in the geometrical acceptance of CDF has been estimated to be $\sim 10\mu$b, the $b\bar{b}$ production cross section at LHC has been estimated to be $\sim 290\mu$b, corresponding to a cross-section of 75μb in the geometrical acceptance of LHCb, for a center-of-mass energy of 7 TeV. At the nominal value of 14 TeV, the cross section at LHC is expected to exceed 500μb.

The angular distribution of the $b\bar{b}$ production is peaked in a small region, in the forward and backward directions. The high correlation between the flight direction of the two hadrons is not surprising if one considers that the $b\bar{b}$ pairs are mainly generated in a s-way Feynman diagram (shown in figure 3.2.b), by two interacting gluons with a high energy and a high momentum. Since the two virtual gluons interacting in the $b\bar{b}$ production transport a variable fraction of the

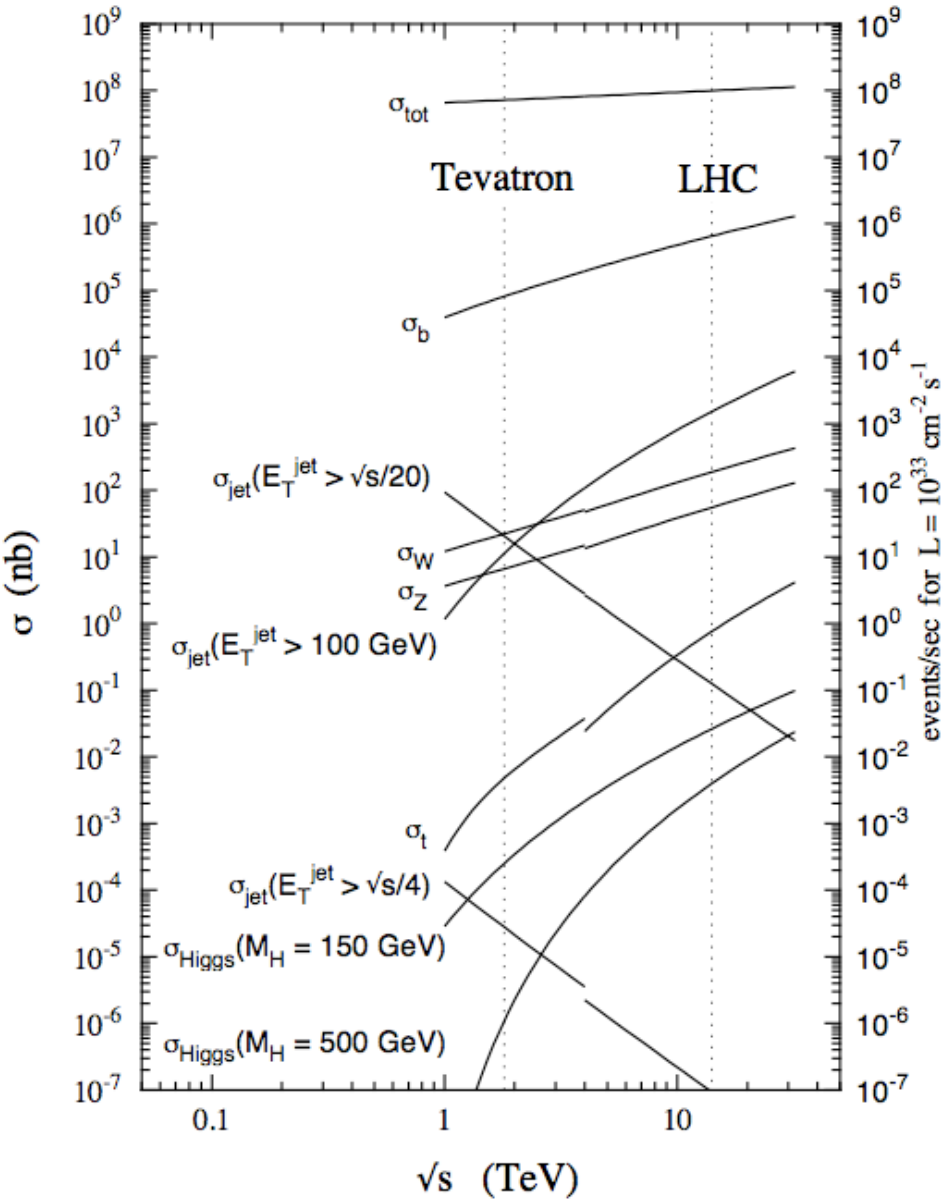

Figure 3.3: Cross sections as a function of the energy $\sqrt{s}$ in the center of mass reference system. For lower energies $p\bar{p}$ collision cross section are represented. For higher energies the pp collision cross sections are plotted. The vertical dotted lines indicate the $\sqrt{s}$ energy of TeVatron and the the design $\sqrt{s}$ of LHC.

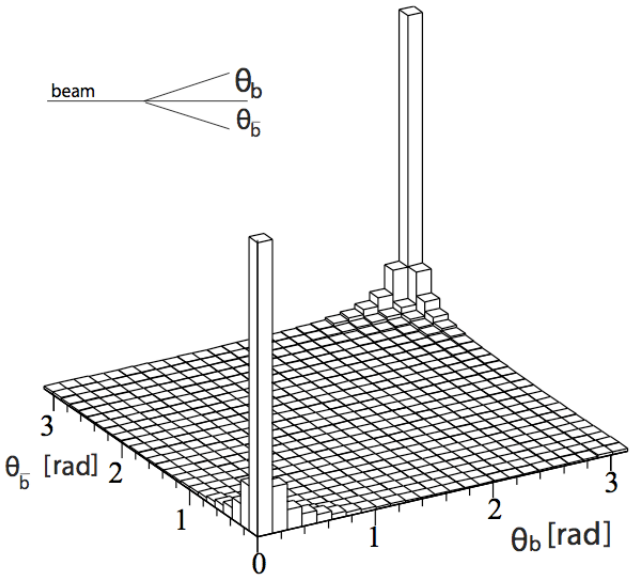

Figure 3.4: The two-dimensional histogram representing the correlation in the directions of the B mesons events generated by a PYTHIA simulation of pp $B\overline{B}$ X events at LHC. The angles θ_b and $\theta_{\bar{b}}$ are the angles between the B ($\bar{B}$) meson flight direction and the beam axis.

colliding protons momentum, they are very unlikely to have exactly opposite momenta. As a consequence, the $b\bar{b}$ pair momentum has a direction close to the beam axis as the longitudinal momentum of the $b\bar{b}$ pair is usually much larger than the transverse one. Once the b quarks are generated they collect light quarks, through the fragmentation (*hadronization*) process, generating baryons or more often mesons. Even if in the hadronization process gluons are exchanged, the B meson flight direction does not differ significantly from the original b quark momentum direction. A Monte-Carlo simulation obtained with PYTHIA is shown in figure 3.4. The illustration shows the remarkable correlation between the directions of the B and $\overline{B}$ mesons in the same event, and the favourite flight direction in forward and backward regions.

3.1.4 The luminosity and the beam time structure

The instantaneous luminosity $\mathcal{L}$ is an important parameter for an accelerator allowing to estimate the expected event rate when the cross section is known. It is defined as the ratio between the event rate and the cross section. It depends on various beam parameters:

$$\mathcal{L} = f\frac{n_1 n_2}{4\pi\sigma_x\sigma_y} \tag{3.1}$$

where f is the frequency of colliding bunches, n_1 and n_2 are the number of protons per bunch and σ_x and σ_y represent the beam transversal dimensions. Because of the variation of n_1 and n_2 due to beam-beam collisions which eject protons from the beams, and because of the increase in σ_x and σ_y due to beam warming, $\mathcal{L}$ changes during the acquisition period. Hence, in order to estimate the number of events expected in a given data sample, the integrated luminosity $\int \mathcal{L}dt$ is usually preferred. To make easier the multiplication with a known cross sections to estimate the number of events in a given period, the integrated luminosity is usually expressed in inverse picobarn pb^{-1}(or its multiples: 1 $\text{ab}^{-1} = 10^3$ $\text{fb}^{-1} = 10^6$ pb^{-1}).

At LHC, the beam is structured in bunches, with a bunch spacing of 25 ns or multiples (at the present time, only a 50 ns spacing is achievable). Up to 2340 bunches of protons per beam can be accelerated in the storage rings. An important parameter is μ, the average number of pp collisions per bunch crossing visible in the detector. This parameter depends on the instant luminosity of the

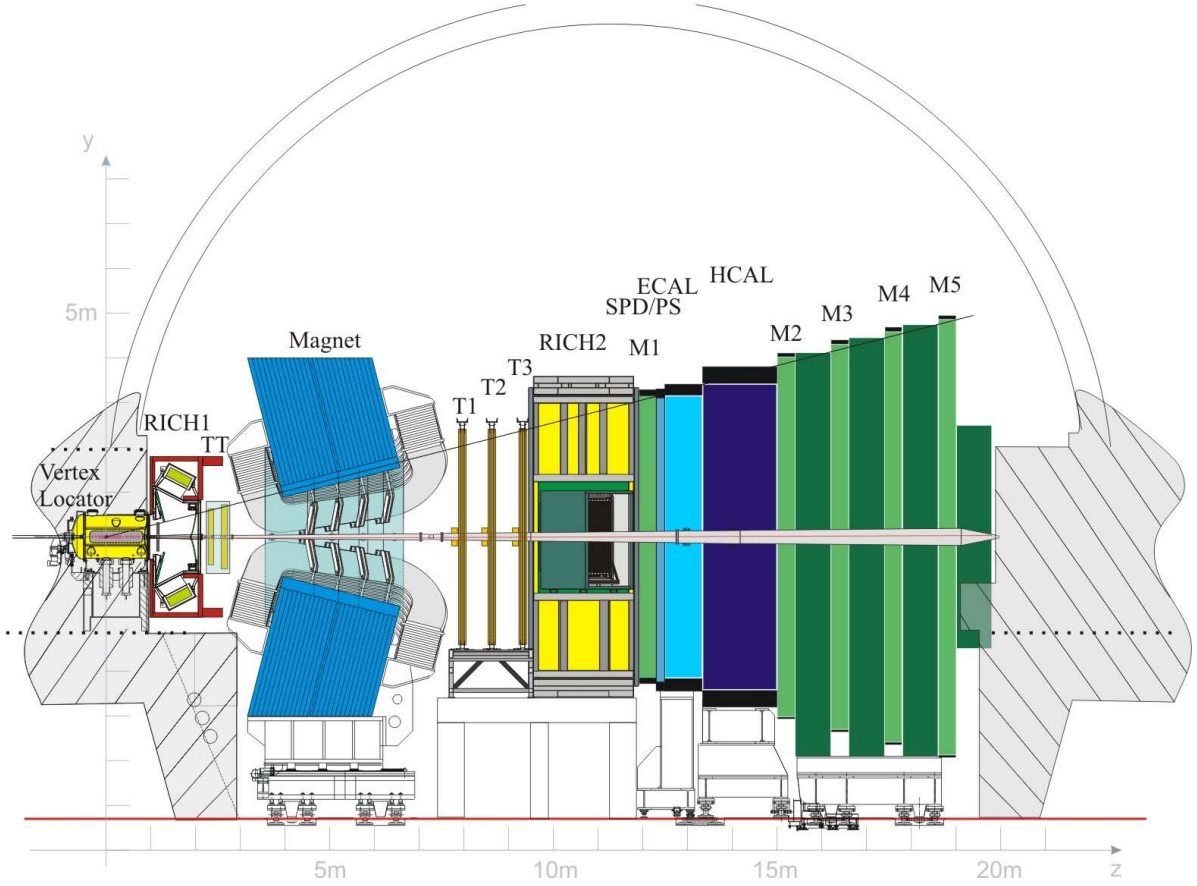

Figure 3.5: A schematic representation of the LHCb detector in the non-bending vertical plane. The definition of non-bending is referred to the magnetic field, which bends particles trajectories in a plane orthogonal to the represented one. The origin of the xy reference system is centered on the beam-beam interaction point.

accelerator. A high value for μ makes the triggering and the event reconstruction more difficult, because more events are produced at the same time. For this reason the LHCb collaboration, to simplify the triggering step, can use beam magnets near the interaction point (IP) to reduce the luminosity and therefore μ. At the time of writing μ equals 1.4. Considering that the $b\bar{b}$ production cross section at 7 TeV, in the LHCb acceptance equals (75.3 ± 14.7) μb [34], 10^{10} $b\bar{b}$ pairs are estimated to be produced in the LHCb acceptance with the first 37 pb^{-1}of data collected in 2010. *BABAR* and Belle have produced $\sim 1.5 \times 10^9$ in their full life-time with an integrated luminosity of $\sim$1.5 ab^{-1}.

3.2 The LHCb detector

The LHCb detector 3.5, located in the cavern previously occupied by the DELPHI LEP experiment, has been developed as a single-arm detector, in contrast with the other three large LHC detectors (ATLAS, CMS and ALICE) which are called 4π detectors since they cover a solid angle of nearly 4π srad. This is a worth choice since the peaked angular distribution of $b\bar{b}$ pair production. The choice of having only one side equipped is a trade off between physics expectations and money costs.

The geometrical acceptance of LHCb for $b\bar{b}$ pairs is about 18%. This is due to the fact that the detector cannot be too close to the beam to measure particles in the highest pseudorapidity[1] regions, without increasing the noise rate due to beams halos. The LHCb detector covers a pseudorapidity range $1.9 < \eta < 4.9$, corresponding to the interval $15 \div 250$ mrad for the polar angle θ.

[1]The pseudorapidity η is defined as $\eta = -\ln\left[\tan\left(\frac{\theta}{2}\right)\right]$, where θ is the angle between the particle momentum and the beam axis.

The key features of LHCb include

- A versatile trigger scheme. High efficiency is required in both leptonic and hadronic B decay channels, in order to collect high statistics samples as well as to measure the variety of modes with small branching ratios;
- An excellent vertex and proper time resolution;
- Precise particle identification, especially for π-K separation;
- Precise invariant mass reconstruction. This feature is required to efficiently reject background due to random combinations of tracks (combinatorial background) and implies a good momentum resolution.

The LHCb detector can be conceptually subdivided in two subsystem:

- *The tracking system*, composed of a vertex locator and a set of tracking stations before and after the huge dipole magnet,
- *The particle identification system*, composed of two calorimeters, two RICH detectors and five muon stations.

The detector has been designed to be projective, in order to reduce dead zones, regions inside the geometrical acceptance of the detector where a particular subdetector is blind.

3.2.1 The tracking system

The LHCb detector is composed of various sub-detector systems [12]. The tracking system is based on four classes of detectors: the Vertex Locator (VELO), a set of silicon tracking stations in the close proximity of the interaction point; Trigger Trackers or *Tracker Turicensis* (TT) placed after the first RICH, before the magnet, and Inner and Outer trackers (IT and OT, named T1, T2 and T3 in figure 3.5) placed after the huge dipole magnet in the inner and outer region respectively. The aim of VELO trackers is to detect with the highest precision the position of the secondary vertices to improve b-tagging and complex decay chains reconstruction efficiency. The Trigger Trackers are used to set a reference before the magnetic deflection. With the additional information from trackers after the magnet, it is possible to evaluate the momentum and to trigger on its transversal component in order to select events with heavy-particle daughter tracks. Finally the Inner and Outer trackers are used to measure the particle deflection due to the 1.1 T magnetic field, and therefore the particle momentum.

The resolution of the tracking system is presented in figure 3.6 for momentum and position near the interaction point. A schematic representation of the magnet is given in figure 3.7.

The Vertex Locator

The VErtex LOcator (VELO) is a silicon detector developed to provide precise measurements of track coordinates close to the interaction region, which are used to identify the displaced secondary vertices which represent a distinctive feature of b- and c-hadron decays [12]. It is composed of 25 silicon stations providing a measurement for the ϕ and r coordinates measured on the opposite sides of each detector. The choice of using cylindrical polar coordinates with z along the beam axis allows a fast determination by the trigger of the impact parameter (the distance of closest approach between the track and the primary vertex) of tracks involved in the decay: the ϕ coordinate is ignored[2] and, defining z the beam axis, only the zr plane is considered.

The VELO stations are arranged to make sure that a particle produced in the geometrical acceptance passes through at least three stations. Since B-mesons fly for a few millimeters (~ 7 in average), a precise measurement of the vertex position allows to achieve the required b-tagging efficiency.

[2]The ϕ coordinate is nonetheless used for track matching.

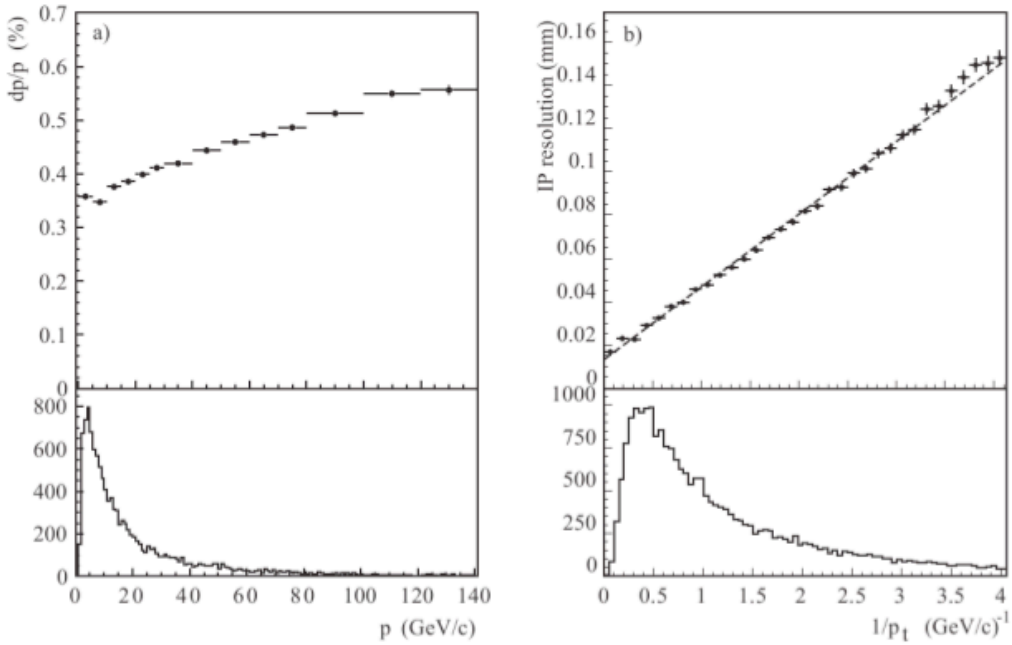

Figure 3.6: On top, resolution on the measurement of p and on the position of the primary vertex as a function of the momentum and of $1/p_T$, respectively. The distributions on these variables are also shown (bottom).

VELO stations are something similar to electronic printed boards with a central hole to let the proton beams pass. To avoid radiation damaging in the LHC injection and acceleration phases, the VELO stations can be opened to move away sensible regions from the not well focalised proton beams. The beams can not be injected if the VELO is not completely opened. Once the injection is over, in condition of stable beams, the VELO stays closed. Since the importance of this detector, data collected with open VELO are considered to be useless and discarded. Before the beams are declared stable, a hardware protection imposes the beam dumping (quick beams switch off) whenever the VELO is moved from the completely open position. When the VELO is closed, only a thin aluminum foil (RF foil) separates the sensor from the beam vacuum in order to prevent out-gassing of the sensor and to shield the electronics against RF pickup from beams. In stable running condition, with the VELO closed, the distance between foil and beam is 5 mm.

The Trigger Tracker

The tracking system is completed by a set of five tracker stations, represented as yellow rectangular shapes in figure 3.5, which measure the position of charged particles downstream of the VELO detector.

The Trigger Tracker (TT) is located just upstream the magnet. It consists of two stations separated by 27 cm. Each station has two layers of silicon strip detectors covering the full acceptance. The strips of the four layers are arranged in order to measure x, u v, x, coordinates, where x is the horizontal axis orthogonal to the beam axis, y is the vertical axis orthogonal to x and to the beam axis (z); and u and v are non-orthogonal axes such that there is a 5 degrees angle between u and x, and between v and x, clockwise and anti-clockwise respectively. This structure is named $xuvx$ and allows a spatial resolution of about 50μm.

Inner and outer tracker

The tracking stations downstream of the magnet (T1, T2 and T3 in figure 3.5) are required to measure the momentum of charged particle deflected by a dipole magnetic field. Their inner part (inner tracker), closer to the beams, is composed of silicon detectors, while the detectors in the outer trackers are *straw tubes*, gas detectors developed to minimize the material budget before the

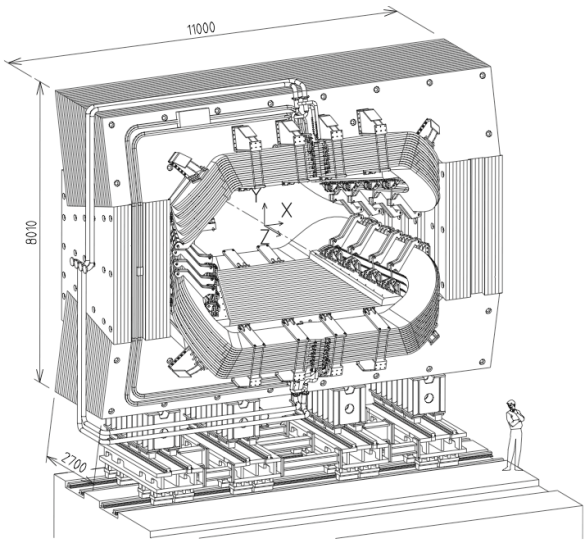

Figure 3.7: A schematic representation of the LHCb magnet.

calorimeters. Inner trackers only cover a region of $\sim 2\%$ of the total area (5 m $\times$ 6 m) of a tracking station, however they measure about 20% of the particle flux, due to the low-angle peak in particle distributions. The rest of the region is covered by *straw tubes* (*drift tubes*), these gas detector rely on the following physical principle: a charged particle passing through an appositely chosen gas ionizes some gas molecules, the intense electric field attracts the ions towards a cathode and the electrons towards the anodic wire. In proximity of the anodic wire, the electric field is stronger and an avalanche multiplication process takes on. The passage of a particle is thus read as a charge collected by the anodic wire. Using the external timing reference from the LHC clock and the drift speed of the chosen gas as an input parameters, it is possible to determine the position of the track with higher spatial resolution by measuring the drift time in the gas. Outer tracker, as well as inner tracker, are disposed following the $xuvx$ structure described in previous section which allows to minimize the dead zones.

The magnet

A dipole magnet is used in the LHCb experiment to deflect charged particles allowing to determine their momentum from the deflection measured by the tracker stations up- and downstream of it. The superconducting magnet originally proposed was too expansive and the construction time was too long, so it has been substituted by a warm magnet with saddle-shaped coils matching the detector acceptance. It provides a peak field of 1.1 T and an integrated bending power of 4 Tm (for 10 m long tracks).

The magnetic field can be inverted periodically to reduce asymmetries due to dis-uniformities in the detector. This feature is of particular interest for analyses involving asymmetries between events originated by B mesons of different charge.

3.2.2 The RICH system. Particle Identification

If compared to ATLAS and CMS, at LHC, and CDF and D$\emptyset$, at TeVatron, LHCb is equipped with a more efficient system of charged particle identification to discriminate between protons, electrons, muons, pions and kaons abundantly produced in B and D meson decays. LHCb is equipped with two Imaging Cherenkov detectors (RICH, *Ring Image CHerenkov*). The first RICH (RICH 1 hereafter) is placed before the magnet and aims to measure low momentum particles which can be deflected out of the detector acceptance by the magnetic field. The RICH 1 provides a complex optical structure made of spherical and plane mirrors which are required to reflect Cherenkov light to the photomultiplier (PMTs) tubes conserving the information on the angles. The PMTs are placed outside the geometrical acceptance and a magnetic shield is provided. Two different

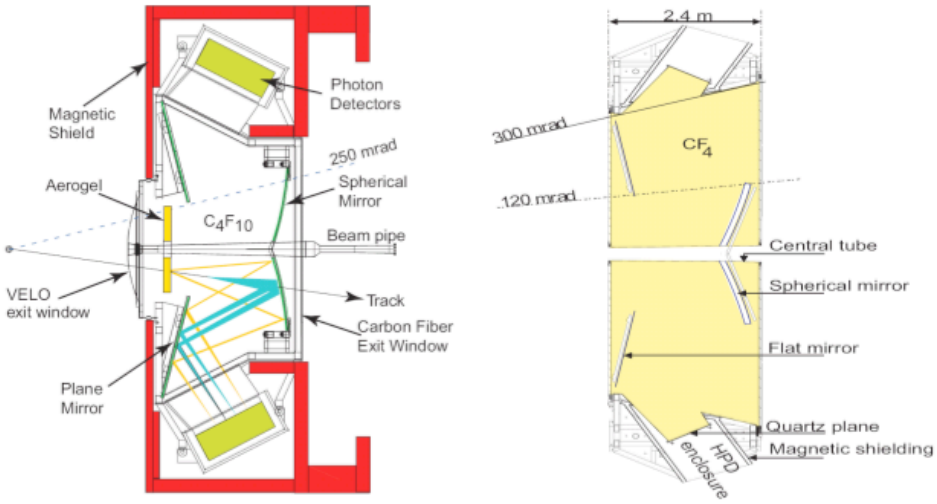

Figure 3.8: A schematic representation of RICH 1 and RICH2 detectors.

radiators share the optical system of RICH 1: silicon aerogel with a refractive index tuned to 1.030 and C_4F_{10} with a refractive index slightly dependent on the wavelenght. At $\lambda = 400$ nm, the gaseous radiator offers a refractive index of 1.0014.

Particles with a higher momentum are supposed to remain in the geometrical acceptance after the magnetic deflection. A second RICH (RICH 2), optimised for high momentum particles, is thus placed after the magnet. The optical structure is somehow similar to the RICH 1, but the only radiator is CF_4, a fluorocarbon gas which offers a refractive index of 1.0005 at $\lambda = 400$ nm. RICH1 acceptance requires a momentum between 1 and 70 GeV/c, while for RICH 2 the interval is 12÷150 GeV/c.

The physical principle of RICH detectors is the emission of Cherenkov light. If the light speed in a given medium is c/n and a charged particle traverses it with a velocity βc, then it emits a cone of Cherenkov light with an angle θ_c between the particle flight direction and the light direction. These quantities are related by the equation

$$\cos\theta_c = \frac{1}{n\beta} \tag{3.2}$$

Experimentally one observes a limited number of PMT activated per event.

To identify a particle the information on the direction and the momentum of a particle is taken from the tracking system, then one ring for each possible mass hypothesis is constructed and the likelihood of each test ring against the positions of the activated PMTs is evaluated.

The RICH likelihood, combined with the information from the calorimeters and the muon system, is associated to each track, and allows different analyses to use different likelihood thresholds to identify a particle. The RICH detectors are schematically represented in figure 3.8.

3.2.3 The calorimeters

The LHCb calorimeter system is composed of an electromagnetic calorimeter and, behind, a hadronic calorimeter. The former is designed to identify electromagnetic showers generated by $e^{\pm}$ and γ due electromagnetic interaction, the latter records energy deposited hadronic showers.

When an electron or a positron traverses the electromagnetic calorimeter, it emits photons by *bremsstrahlung*. For high energy electrons ($E > 1$ GeV), the characteristic distance of this process does not depend on energy and is named *radiation length* X_0. It is defined as

$$\frac{1}{X_0} = \lim_{E\to\infty} \frac{1}{E}\left(\frac{\mathrm{d}E}{\mathrm{d}x}\right)_{\text{Bremsstrahlung}} \tag{3.3}$$

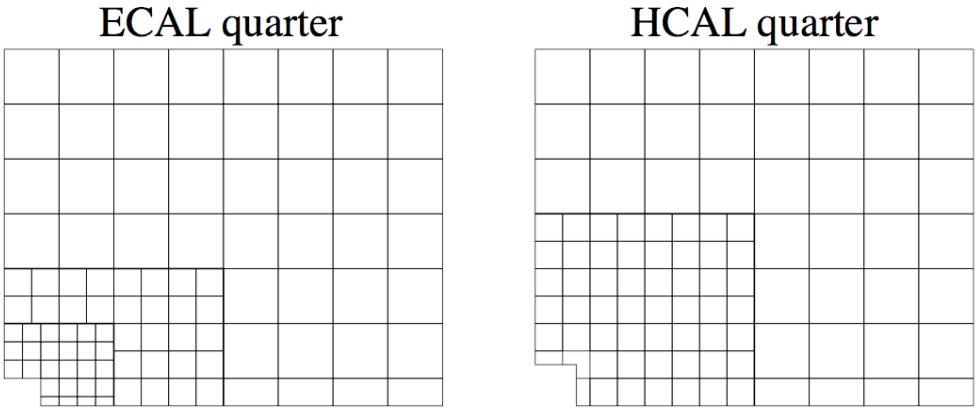

Figure 3.9: Calorimeter lateral segmentation: electromagnetic calorimeter (left), hadronic calorimeter (right).

The radiation length is also relevant for the multiple scattering process, the deflection of a particle traversing matter due to multiple Coulomb scattering.

Each emitted photon then converts to an electron and a positron, which emit bremsstrahlung photons and so on, thus originating an electromagnetic shower.

A photon hitting the calorimeter converts to an electron-positron pair, starting an electromagnetic shower. The average distance that a high energy photon can cover before converting to e^+e^- is $\frac{7}{9}X_0$. Since the characteristic length for photons and electrons are of the order of X_0, this value is appropriate to describe the longitudinal development of an electromagnetic shower and is used to indicate the thickness of electromagnetic calorimeters.

Using PMT-read scintillator layers, alternated to high-Z absorber layers, it is possible to estimate the energy deposited by charged particles generated in such an electromagnetic shower. Calorimeter calibration allows to determine the relation between the electric signals from PMTs and the deposited energy.

An analogous principle is exploited in hadronic calorimetry, but in this case the traversing hadron interacts by strong nuclear interaction with atomic nuclei. The hadronic shower process is much more complex to describe than the electromagnetic case, but it is essential to study neutrons and useful to identify charged hadrons. In this case the characteristic length of the process is called (nuclear) interaction length λ_I and is defined as the average distance a hadron covers before a strong interaction occurs.

The main purposes of calorimeters are:

- To achieve the transverse energy measurement for charged hadron, electron and photon candidates. This information is used for the lower level trigger decision.
- To provide particle identification to distinguish between electrons or positrons, photons and hadrons. Calorimeters are also intended to measure position and energy of neutral particles.
- To offer high reconstruction accuracy for π^0 and photons.

The electromagnetic calorimeter

The Electromagnetic CALorimeter (ECAL) is a sampling calorimeter composed of multiple and alternated layers of lead and scintillator, in a structure named *shashlik*. The scintillator is readout through optical fibers wired to photomultiplier tubes. A lateral segmentation in square-shaped cells provides good shower separation and angular resolution. The cell size varies with the region: in the inner section, closer to the beam, where the ECAL requires to deal with a higher particle rate, it is equipped with 40.4 mm wide cells. The cells in the intermediate region are 60.6 mm wide, while in the outer region a 121.2 mm width is considered sufficient to deal with the lower particle

	M1	M2	M3	M4	M5
R1[mm^2]	10 × 25	6.3 × 31	6.7 × 34	29 × 36	31 × 39
R2[mm^2]	20 × 50	12.5 × 63	13.5 × 68	58 × 73	62 × 77
R3[mm^2]	40 × 100	25 × 125	27 × 135	116 × 145	124 × 155
R4[mm^2]	80 × 200	50 × 250	54 × 270	231 × 290	248 × 309

Table 3.1: Logical pad dimensions (horizontal × vertical) for each station and region. Dimensions follows the projective principle of LHCb design.

rate. The ECAL lateral segmentation is shown in figure 3.9, left. The ECAL resolution follows the expression

$$\frac{\sigma_E}{E} = \frac{10\%}{\sqrt{E/1\text{GeV}}} \oplus 1\% \tag{3.4}$$

where the symbol $\oplus$ indicates a squared sum root: $a \oplus b = \sqrt{a^2 + b^2}$.

To distinguish between charged and neutral particles hitting the calorimeter a scintillator pad detector (SPD) is placed in front of the electromagnetic calorimeter. It is a fine laterally segmented scintillator layer which aims to associate an input position to charged particles before the electromagnetic shower. This also improves the connection of the shower with the corresponding charged track. In order to disentangle overlapping electromagnetic showers casted by different particles a second finely segmented scintillator pad, called pre-shower detector (PS), is placed downstream of a 2.5 X_0 thick lead converter layer, located downstream of the SPD. This PS detector is also useful to distinguish between charged pions and electrons or positrons: indeed, as opposed of electrons and positrons, pions are supposed to traverse the 2.5 X_0 absorber without initiating a shower. The thickness of the ECAL is 25 radiation lengths, which are considered to be sufficient to completely contain electromagnetic showers of higher energy photons.

The hadronic calorimeter

The Hadronic CALorimeter (HCAL) is a sampling device made of iron and scintillating tiles, as absorber and active material respectively. In contrast with the ECAL, the scintillator tiles of the HCAL are oriented to be parallel to the beam axis. This feature can be used to obtain a better angular resolution from the HCAL. The HCAL thickness equals 5.6 interaction lengths, which are not sufficient to ensure the whole containment of the hadronic shower, but are enough to achieve a good measurement of the energy.

The HCAL is laterally segmented into square cells of size 131.3 mm in the inner section and 262.6 mm in the outer section, see figure 3.9, at right.

3.2.4 The muon system

Many CP-sensitive B decays have muons in their final states. Hence, muon triggering and also offline reconstruction of muons is of great importance at LHCb. The muon detection subsystem is composed of 4+1 stations of multi-wire proportional chambers (MWPCs) with cathode pad readout. Four of the five stations are placed behind the HCAL, the first one is placed between the RICH 2 and the ECAL. The five stations are referred to as M1, M2 ... M5 and cover an angular acceptance of 20 ÷ 306 mrad in the bending xz plane and 16 – 258 mrad in the non-bending yz plane. The minimum muon momentum required to traverse all the five stations is about 6 GeV/c.

The tracks measured by the last four stations are considered to be muons since other particles are supposed to lose all their energy before or inside the HCAL. To ensure that no other particle can reach the MWPCs, the four stations M2-5 are interleaved with three 80 cm thick iron absorbers (see fig. 3.5).

The lateral segmentation depends on the region. Each muon station is divided in four regions R1 ... R4 from the inner to the outer border. To simplify the electronics, more cathodic pads are OR-ed in logical pads. The dimensions of logical pads are given in table 3.1.

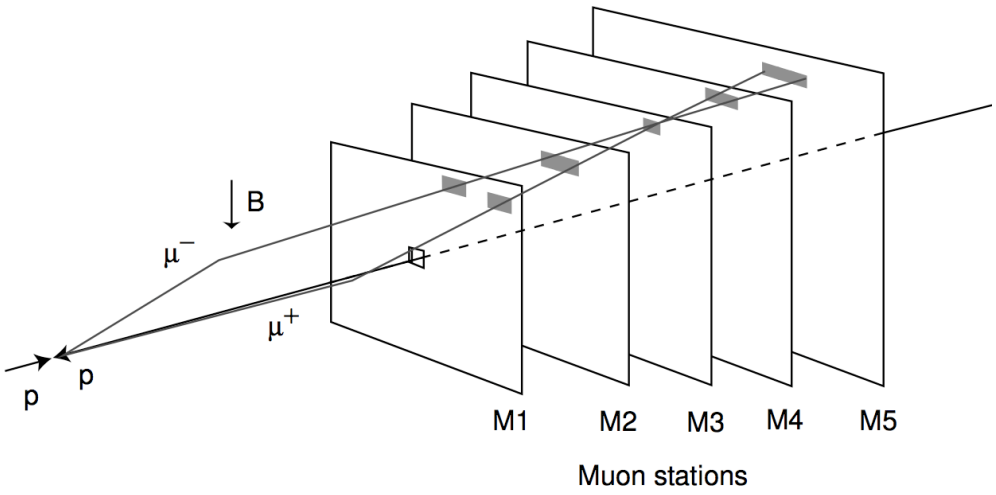

Figure 3.10: Schematic representation of the muon system. The drawn tracks represent two muon of opposed charge, traversing the muon system in the external region. Only M1 register them as two different tracks.

M1 is placed before the calorimeters and has the double aim to improve muon momentum determination, by measuring the muon position before the random deviation of the muon track introduced by multiple Coulomb scattering phenomena, and to distinguish the two muons in events like the dimuon event shown in figure 3.10. Since M1 is located before the calorimeters, the inner region of this chamber is interested by a high counting rate. Since MWPC technology is not sufficiently resistant to radiation damage nor to achieve an occupancy low enough, Gas-Electron-Multiplier chambers (GEMs) have been adopted in the region M1R1. While the momentum is measured with the tracking system, the muon station is crucial for muon identification in decays such as $J/\psi \to \mu\mu$ or searches for rares decays $B_{s,d} \to \mu\mu$ and $B_{s,d} \to K^*\mu\mu$.

3.2.5 The Trigger

One of the key feature of the LHCb experiment is the trigger system. At LHCb luminosity, considering the LHC bunch crossing structure, the rate of events with at least two particles in the LHCb acceptance is ~ 10 MHz (against the nominal value of 40 MHz if one considers the LHC nominal crossing rate). The rate of events containing b quarks is ~ 100 kHz, but only a few hertz rate is expected for interesting events, due to the combined effect of branching fraction and detector acceptance. This is why LHCb needs a highly selective and efficient trigger.

One of the discriminant variables for the trigger selection is the long b hadrons lifetime, resulting in secondary vertices well separated from the primary one. Also their relatively large mass, resulting in decay products with a large transverse momentum, is useful to discriminate b hadrons decay products from the combinatorial background.

The trigger is structured in two layers, the Level 0 (L0) trigger and the High Level Trigger (HLT). L0 is hardware implemented on electronics boards, and it is designed to reduce the input rate to 1 MHz with a fixed latency of 4 μs. At this rate LHCb sub-detectors can be read out, and events are sent to a computer farm with about 1350 multiprocessor boxes where more than 20 000 copies of the HLT software algorithm are executed in parallel. The HLT has to reduce the event rate down to 2-3 kHz, a rate which allows tape recording.

The L0 trigger

The Level0 trigger is based on calorimeter and muon chamber information. It selects muons, electrons, photons or hadrons above a loose transverse momentum or energy threshold. Such a threshold is usually in the range $1 \div 4$ GeV and depends on the particle type (photons have a

higher threshold than muons).

While in 2010 the L0 bandwidth was dominated by muon triggers because during the preliminary acquisition phases a higher priority was set to brighter channels, requiring less statistics to achieve interesting results, the plan for 2011 is to select $\sim$ 400 kHz events by L0 hadron trigger, which is unique within the LHC experiments, and 400 kHz by muon triggers. The rest of the bandwidth would be occupied by the electromagnetic calorimeter triggers.

The High Level Trigger

The HLT algorithms are designed to be inclusive, fast and simple to minimize systematic uncertainties. This is possible by performing at a first stage, called HLT1, a partial event reconstruction in order to confirm L0 trigger decision with a more complete analysis. Once the decision has been confirmed, the event rate reduces down to $\sim$ 30 kHz and the global event reconstruction is possible. The average CPU time for the global reconstruction is of the order of 20 ms per event.

The second stage of the High Level Trigger, called HLT2, reduces events to a rate of $\sim$ 3 kHz, a relatively high rate exceeding the design value of 2 kHz. This increase is due to the broader physics program that the collaboration is now pursuing, in particular in charm decays area. The experiment will thus collect a clean sample of about 1 kHz each for leptonic, hadronic b decays and charm decays categories.

The trigger efficiency has been estimated for the three classes of decays. For B leptonic decay, the trigger is expected to reach an efficiency of about 90%. For hadronic B decays, a 40% trigger efficiency is expected. For charm decays, only a 10% efficiency is achievable, but the expected number of produced c quarks is much higher than the expectation for b quarks. These values are orders of magnitude and are slightly different for each individual channel in a same category.

3.2.6 2010 running conditions

During 2010 run, the LHCb experiment has collected an integrated luminosity of $\sim$ 37 pb^{-1} at a center of mass energy $\sqrt{s}$ = 7 TeV. The performance of the LHC has improved progressively all along the year and most of the integrated luminosity was collected with the last few days. At the beginning of 2010, LHC run with a reduced number of colliding bunches, so that LHCb could use a very loose trigger. However, at the end of the year, LHC has reached an impressive peak luminosity by colliding a number of bunches eight time smaller than nominal (344 instead of 2622) but achieving outstanding beam focalization, with an high number of protons per bunch. This implies a number of visible interactions per bunch crossing $\mu > 2.5$, a factor six above the design value. Such a *pile-up* value represents a challenge for the trigger, the offline reconstruction and data processing in general.

LHCb has demonstrated to be able to cope with these extreme conditions, so that data was taken at the highest luminosity available from LHC all the time.

Such an excellent experience in 2010 has opened interesting prospects for 2011-2012 run. A procedure of luminosity leveling, based on displacing the beams in the vertical direction has been defined with the LHC team. This would imply less pile-up at the start of the fill and a more constant behavior in time, allowing LHCb to collect the maximum integrated luminosity under optimal conditions. This procedure uses a vertical displacement of the beams and takes on after any beam initialization (once the beam has been declared stable) in order to reach a luminosity of $3 \times 10^{32}\text{cm}^{-2}\text{s}^{-1}$ (about $\frac{1}{7}$ of the $\sim 2 \times 10^{33}\text{cm}^{-2}\,\text{s}^{-1}$ achieved at ATLAS and CMS since end of July 2011). Whenever the luminosity decreases during the run, the two beams are approached to reach the required luminosity, again.

3.2.7 LHCb compared to the other LHC experiments

An interesting question, often addressed to LHCb scientists is "couldn't we study the same physics with the LHC general purpose detectors?". To answer the question, I briefly review the main differences between LHCb and ATLAS/CMS.

The single arm structure reduces the geometrical acceptance by about a factor 2 with respect to the two symmetric arms solution, but, besides reducing costs of a much higher factor, there are other significant advantages which make the choice worth. The possibility to allocate the infrastructures outside the geometrical acceptance allows a very low material budget (less than one radiation length before the calorimeters), which means that multiple scattering problem is strongly reduced. As a consequence it is possible to obtain very good vertex and interaction point resolutions. The vertex resolution in the transversal direction is 15.8 μm for LHCb, whereas for ATLAS is 60 μm and for CMS between 20 and 40 μm. LHCb can achieve these resolutions with 25 tracks or less, a greater number of charged tracks would make harder for the tracking system to reconstruct properly the event. For this reason the luminosity at LHCb has been reduced.

Also the mass resoultion at LHCb is better than the mass resolution at ATLAS and CMS. Considering the $J/\psi \to \mu\mu$ channel, LHCb can reach a mass resolution of 13 MeV, while CMS and ATLAS have 40 and 71 MeV resolution, respectively.

However, ATLAS and CMS have an important part of their experimental program on b physics.

Chapter 4

Elements of the analysis of $B^{\pm} \to D^0 K^{\pm}$

As described in the chapter 2.3.7, $B^{\pm} \to D^0 K^{\pm}$ decays represent the favourite channel to measure the angle γ through GLW and ADS methods. Results from the B-factories will be improved by LHCb analyses. In this section I briefly review results from *BABAR* and Belle and describe what has been done at LHCb. Using the selection criteria from the collaboration, I have implemented the software tools to select the candidates from the stripped data samples and to fit reconstructed B mass distribution of the selected events.

About the notation

In this section I won't distinguish between D^0 and $\bar{D}^0$ states, indicating with D^0 both flavor eigenstates. Experimentally, the D^0 is reconstructed from the decay to two charged hadrons requiring the correct reconstructed invariant mass, which is the same for D^0 and $\bar{D}^0$ states. However, it is worth to remind that B^+ decay products are more often $\bar{D}^0 h^+$ than $D^0 h^+$ and vice-versa B^- decays preferentially to $D^0 h^-$ with respect to $\bar{D}^0 h^-$.

4.1 Results from B factories and CDF

B-factories reconstruct D mesons in both $CP+$ and $CP-$ final states, while CDF only reported studies on $CP+$ final states. For $CP+$ final states both K^+K^- and $\pi^+\pi^-$ final states are considered. $CP-$ final states are detected as $K^0_s\pi^0$, $K^0_s\phi$ and $K^0_s\omega$. The $CP-$ final states are difficult for LHCb to reconstruct, so that in a first analysis they will not be included.

Yields and results are reported in table 4.1. One can notice that the statistical precision on GLW and ADS observables depends on N_{CP+} and N_{WS}, respectively.

GLW method

	BELLE [13] (2006)	BABAR [14] (2010)	CDF [15] (2009)	Combination
N_{CP+}	149	477	91	-
R_{CP+}	$1.13 \pm 0.16 \pm 0.08$	$1.18 \pm 0.09 \pm 0.05$	$1.30 \pm 0.24 \pm 0.12$	1.18 ± 0.08
A_{CP+}	$0.06 \pm 0.14 \pm 0.05$	$0.25 \pm 0.06 \pm 0.02$	$0.39 \pm 0.17 \pm 0.04$	0.24 ± 0.06
$\int \mathcal{L} dt$	-	-	5 fb^{-1}	
$N_{b\bar{b}}$	275 millions	467 millions		

ADS method

	BELLE [16] (2011)	BABAR [17] (2010)	CDF [18] (2010)	Combination
$N_{RS}(B \to D\pi)$	49000	24000	17700	90700
N_{WS}	35	19	34	88
R_{ADS}	$0.0163^{+0.0044\ +0.0007}_{-0.0041\ -0.0013}$	$-0.011 \pm 0.006 \pm 0.002$	$0.0225 \pm 0.0084 \pm 0.0079$	-0.0153 ± 0.034
A_{ADS}	$-0.39^{+0.26\,+0.04}_{-0.28\,-0.03}$	$-0.86 \pm 0.47^{+0.12}_{-0.16}$	$-0.63 \pm 0.40 \pm 0.23$	-0.53 ± 0.21
$\int \mathcal{L} dt$	-	-	1 fb^{-1}	
$N_{b\bar{b}}$	722 millions	467 millions		

Table 4.1: Yields and results claimed by B-factories and CDF experiments for GLW and ADS methods. Reference: [19]

As discussed below, with the 37 pb^{-1} from the first year of data taking LHCb claims a yield of about hundred CP+ events. Even if the analyses are at a very preliminary stage, the important contribution that the collaboration will bring to the measurement of γ is already evident. ADS method has also been studied at B-factories and CDF. The three experiments have measured different values for A_{ADS}, but the sign is the same for the three results. Finally, one can notice the large value of the ADS asymmetry (even if with large errors) as anticipated for this method. Currently the most accurate A_{CP+} measurement has been performed by the Babar collaboration reporting an asymmetry of $0.25 \pm 0.06 \pm 0.02$.

More details about the current precision on the GLW and ADS observables are available in [19, 35].

4.2 The Analysis at LHCb

It is always difficult to simulate experimental conditions of a quickly changing environment. Even with a precise description of material distribution and detector response of a highly efficient experiment, the simulation is never perfect. In 2010 the LHC machine running conditions have changed all along the year as well as the LHCb trigger conditions. Therefore Monte Carlo simulations are considered to be unsafe and their use in analyses is deprecated, however the comparison between MC simulated data samples and real data is a powerful tool to understand the kinematics of signal and background and the response of the detector. Hence, a validation of Monte Carlo sample versus real data is a common starting point for analyses. Once that the distributions of analysis-related variables are verified, trigger effects can be investigated by applying the trigger algorithms on MC samples. While the selection of the events on MC allows to evaluate the selection efficiency, D mass sidebands in data sample are exploited for background rejection studies. The B mass probability density function (pdf) is modelled using MC samples for signal and specific background channels, while generic and combinatorial background is modelled using mass sidebands. A final fit on data is used to extract the number of signal candidates. Ratios between yields are proportional to ratios between the squared amplitudes, thus the measurement of A_{CP} and R_{CP} can be extracted by combining fit results. The more difficult ADS analysis is not yet available at LHCb.

4.2.1 Monte Carlo validation.

A Monte Carlo simulation is a huge software tool using Monte Carlo algorithms to generate particles with the expected probabilities in proton-proton collisions, Monte Carlo algorithms to establish the decay chain of each generated particle, and Monte Carlo algorithms to study the interaction of each particle with the detector. Once the simulation is over, the collaboration has output files identical to real data files, with the addition of the so called *Truth* information, a set of variables filled by the Monte Carlo simulation describing the particle properties as they were intended by the Monte Carlo generator, rather than they have been reconstructed by the detector. Imposing a condition between reconstructed and *true* variables is called truth matching. In my work I have often adopted a PID truth match, selecting only events whose particles have been properly identified.

In order to validate MC sample versus real data, the distributions of variables which are involved in the reconstruction and in the selection are presented, for data and Monte Carlo, in appendix A. The distributions are obtained from the Cabibbo Favored (CF) analysis $B^- \to D^0\pi^-$ with $D^0 \to K^-\pi^+$ after all the selections (see below) have been applied.

A comparison between the distributions obtained for Monte Carlo and data shows that the agreement between the two samples is quite good for all the variables related to the analysis, but:

- Variables related to particle identification, like the PID likelihood[1] of the bachelor track (the hadron h produced in $B \to Dh$ decay). As an example, the difference of log-likelihood $K - \pi$

[1] A likelihood $\mathcal{L}$ is something similar to a non-normalized probability. In this case it represents the probability for a measured particle to be a kaon. If a long-lived charged hadron is not identified as kaon or as a proton (anti-proton), it is considered to be a pion. The negative values of the $K - \pi$ DLL (difference of logarithmic likelihood, $K - \pi$ DLL $= \log \mathcal{L}_K - \log \mathcal{L}_\pi$) are intended as an indication that the particle is likely to be a pion.

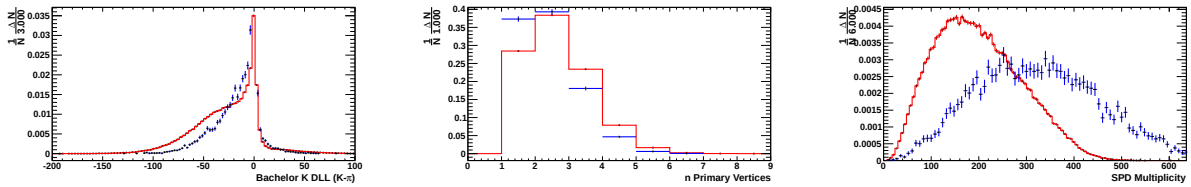

Figure 4.1: Comparison between the normalized probability density functions in Monte Carlo simulation (red solid line) and data (blue points). The variables which have been considered are, from left to right: the difference of logarithmic likelihoods between kaon and pion hypotheses ($K-\pi$ DLL) for the bachelor track, the number of primary vertices reconstructed in the VELO and the number of hits in the SPD (scintillator pad). The distributions for the other variables involved in the analysis are given in appendix A.

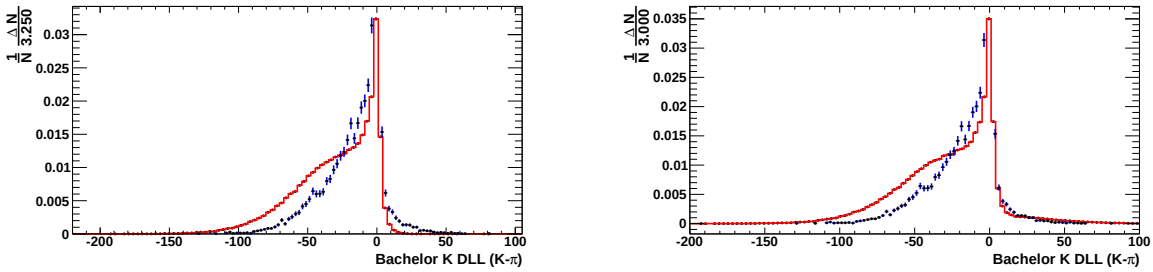

Figure 4.2: Monte Carlo validation for the $B \to Dh$ bachelor track PID with a pure $B \to D\pi$ MC sample (left) and with a MC sample mixing $B \to D\pi$ and $B \to DK$ events according to the nominal branching ratios (right). Plots show the normalized pdf in the $K-\pi$ DLL. Blue points with errors represent data, red histograms MC.

DLL is plotted in figure 4.1 (left).

- Variables related to track multiplicity. In particular the number of primary vertices detected by the VELO detector and the number of hits on the calorimeter scintillator pad detector (SPD). Both distributions are presented in figure 4.1, middle and right plots. These quantities directly depend on LHC operational conditions.

The problem on PID related probability density functions is being studied. It is probably due to a poor RICH aerogel-radiator simulation. Problems in multiplicity are also investigated. They are probably due to the many and frequent changes in configurations which, in the first period of LHC operation, have been impossible to be accurately modelled in Monte Carlo. In particular all the parameters related to the luminosity (including the number of colliding bunches and the time spacing, which have been varying often), to the LHC optics near to the interaction point and to trigger conditions, have changed dramatically from March to November 2010, while the whole MC sample has been obtained for a fixed set of parameters. Analyses which have to rely more on Monte Carlo simulations should provide a recalibration of the MC sample to correctly reproduce the experimental behaviour. The analysis presented here has been performed with a typical fixed Monte Carlo, since its reliability has been considered sufficient for a preliminary analysis.

The particular case of the PID of the bachelor track

The PID of the bachelor track is a particular case because the $B \to DK$ and $B \to D\pi$ decays have been simulated in separate MC samples. In data both $B \to DK$ and $B \to D\pi$ are present, with a ratio between the branching fractions

$$\frac{\Gamma(B \to DK)}{\Gamma(B \to D\pi)} \sim 7\% \tag{4.1}$$

Neglecting the contribution of $B \to DK$ decays, and comparing the data set $K-\pi$ DLL distribution with that of the dominant channel $B \to D\pi$ in MC simulation, one gets the plot in figure 4.1 at

left. Since the agreement is very poor, one can try to introduce the missing $B \to D\pi$ decays with the correct branching ratio. The result is shown in figure 4.1, the agreement is better in the right (kaon) portion of the histogram, but strong problems in the agreement between data and Monte Carlo are still present.

The cause of the disagreement is perhaps related to a non perfect simulation of the combinatorial background and the π identification.

4.2.2 Considerations on the trigger

The comprehension of the trigger structure is essential to understand selection efficiencies. Since the trigger evolves quickly with the physics priorities (in 2010, muon trigger algorithms for rare decays as $B_s \to \mu\mu$ have dominated the trigger occupancy), a trigger configuration identifier (Trigger Configuration Key, TCK) is provided to allows analysts to reproduce the trigger influence on simulated data for different acquisition periods. It is important to study differences in the efficiency for each TCK, a two byte configuration word which identifies uniquely the algorithms used in the trigger. A study on the TCKs used in 2010 suggests that the efficiency is almost independent of the TCK. In the HLT2 [36] one distinguishes between Topological and Physics trigger lines (algorithms). The Physics trigger lines are based on the identification of the specific channel of interest, while Topological trigger lines look for hadronic B decays to two, three or four charged particles. For the channels considered here, the efficiency of the physics trigger lines ($\sim 18.5\%$) is slightly higher than the efficiency of the topological lines ($\sim 17.5\%$).

Possible biases in various event samples can be studied using the TIS and TOS categories. For Trigger On Signal (TOS) events, the trigger decision is due to the detection of the considered decay. For Trigger Independent on Signal (TIS) events, the trigger decision is taken because other interesting channels are detected, and so the event is recorded independently on the signal considered in the analysis. The number of TIS events is expected to be well below the TOS yield, but the comparison between the two categories is an important tool to study biases introduced triggering on signal.

4.2.3 The global reconstruction

The global event reconstruction is a very CPU-time consuming process, for this reason it is managed by the collaboration and its output constitutes the input for the many LHCb analyses. This has the double advantage that the reconstruction policy, which requires a deep knowledge of the detector, can be fixed for all the collaboration to the most reliable form by experts from each sub-detectors, secondly the analysis process can be focalized on the event selection and noise rejection or to the a more precise reconstruction of few particularly relevant variables to override the collaboration standard.

There are two global reconstructions during the acquisition chain of LHCb. The first global reconstruction occurs in the trigger between the HLT1 and the HLT2 selections. The second, much more complete and accurate, is the first off-line operation and restarts from tape recorded raw data. During the reconstruction tracks and vertex are formed. A track is a hypothetical pathway of a charged particle reconstructed according to the hits recorded in the tracking system, from the VELO down to the T1, T2 and T3 stations. A track is not required to traverse all the tracking stations: charged particles leaving the detector acceptance before the magnet, or just after the VELO are still named tracks. In general the fit algorithm to transform a set of hits into a track starts with lower occupancy detectors and extrapolates the expected track to higher occupancy regions, if the track match is possible the track is kept, else it is rejected. Once the set of hits is defined a fine fit is performed and the information from the PID apparatus (calorimeter, RICH and muon systems) is added to complete the information on the particle.

An intersection between the tracks is called vertex. Vertices are classified in primary and secondary vertices. The former are proton-proton interaction vertices, giving rise to the primary particles (for example B mesons), the latter are decay vertices.

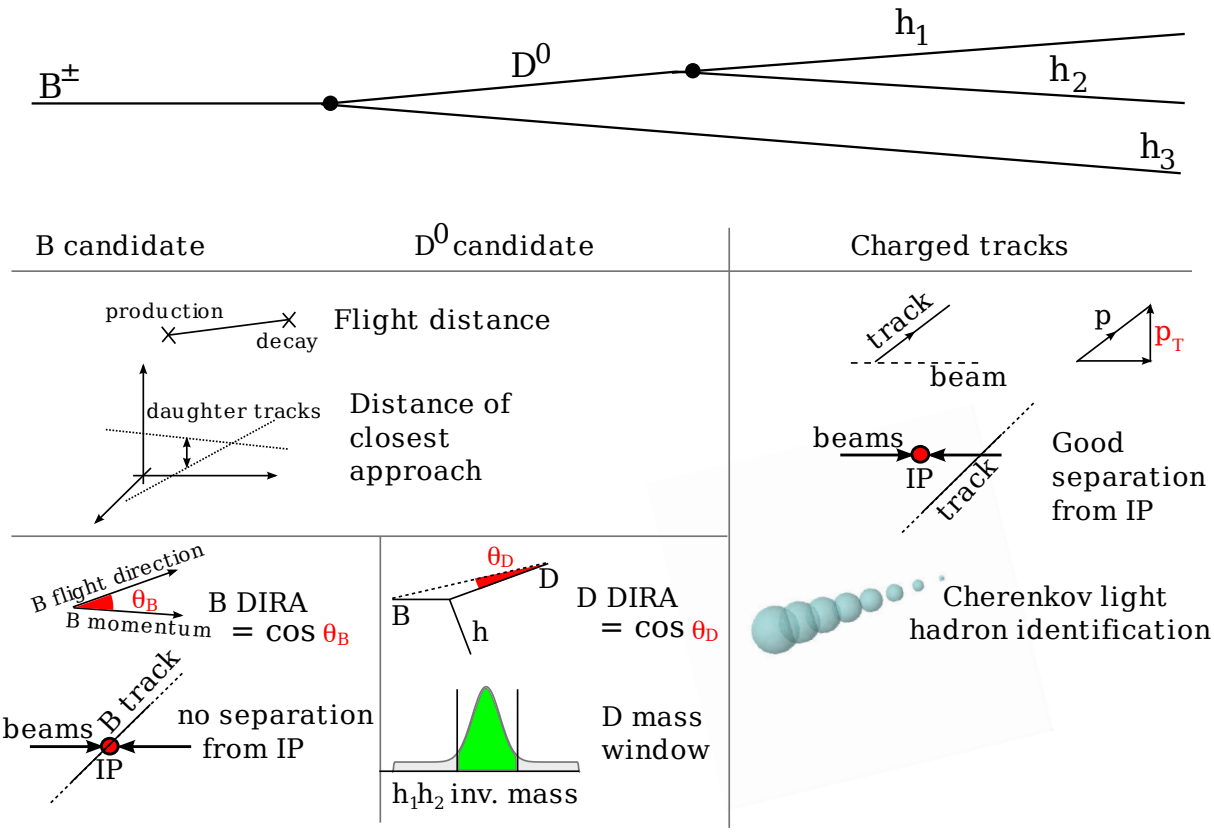

Figure 4.3: A graphical summary of the variables involved in the event selection.

In case of ambiguity between (for example) two possible tracks or two possible PID hypotheses, both solutions are saved in the output location of the global reconstruction. It is up to the selection algorithms to discard the wrong candidate according to tunable criteria.

4.2.4 Selection

Stripping

The process to select events from the triggered sample, written on tape and arranged according to the trigger line activated by the event, is structured in two steps. The first stage is called *stripping* and consists of algorithms which read various trigger lines and, after the event reconstruction, select events eligible for containing the required signal and write them to files, stored in multiple copies (replicas) on computing centers all over the world inter-connected through the LHC Computing Grid (LCG) protocol [37]. The data samples are named according to the off-line reconstruction and stripping versions. The data sample used for this analysis is called *Reco08Stripping12* and corresponds to an integrated luminosity of ~ 37 pb^{-1}. The stripping line used for this analysis is called *StrippingB2DXWithD2hhLine* and applies very loose cuts to select the inclusive channel $B \to D^0 X$ with $D^0 \to hh$, where h is a generic charged hadron. The stripping line requires the total number of tracks with hits in both VELO and tracker stations to be less than 100. To identify a track as a B or D daughter particle, its momentum has to be higher than 2 GeV/c with a transversal component greater than 250 MeV/c. Cuts on the reconstruction quality requires a χ^2 for the charged particle trajectories lower than 5 and, to discard particles generated in the p-p collision, the separation χ^2 from the primary vertex, obtained by forcing in the charged tracks fit the null-separation hypothesis, is required to be 4 or more. To state that a particle is a D candidates, involved in a $B \to (D \to hh)h$ decay, one requires the following conditions to be satisfied. The reconstructed meson mass is required to be in an interval of $\pm$ 100 MeV from the nominal value of the D meson mass. In order to reduce combinatorial background, the D decay vertex has to be reconstructed with a χ^2 smaller than 12, while the χ^2 related to the separation of the decay vertex

Charged tracks	**D^0 candidate**	**$B^\pm$ candidate**
$p_T > 330$ MeV/c	DOCA < 0.3 mm	Interaction point $\chi^2 < 9$
Separation χ^2 from IP > 21	Flight Distance $\chi^2 > 252$	DOCA < 0.1 mm
Bachelor K PID $K-\pi$ DLL > 3	DIRA > 0.992	Flight Distance $\chi^2 > 72$
Bachelor π PID $K-\pi$ DLL $<$ -2	Vertex χ^2 / $N_{dof} < 6$	DIRA > 0.99995
Kaon (D^0 daughter) $K-\pi$ DLL > 0	Mass window: {-40, +30 } MeV/c^2	
π (D^0 daughter) $K-\pi$ DLL < 10		

Table 4.2: Summary of the selection cuts applied to the $B^\pm \to D^0(hh)h$ analyses. The definition and the explanation of the selections is given in the text.

from the primary vertex has to be at least 36, furthermore the separation χ^2 from the primary vertex, for at least one of the D daughters, has to be higher than 40. The transverse momentum of the D candidate is required to be higher than 1 GeV/c. The cosine of the angle between the momentum of the D meson, and the straight line passing through primary and D decay vertices, (called DIRA) is required to be higher than 0.9. As expected, this quantity is always close to one (the angle is almost null), because the momentum of the B particle, in the lab frame, is almost aligned with the D momentum. Finally the Distance Of Closest Approach (DOCA) between the daughter particles is required to be smaller than 1.5 mm.

The selection cuts applied to the B candidates are listed below. The bachelor hadron track is required to have a momentum higher than 5 GeV/c with a transverse component of at least 500 MeV/c. The χ^2 of separation between the B decay vertex and the primary vertex has to be greater than 16, while the χ^2 of the decay vertex reconstruction is required to be less than 12. Also, the separation χ^2 between the primary vertex and the beam-beam interaction point cannot be higher than 25, because the B meson is expected to be created in the p-p collision. The proper lifetime of the B candidate has to be at least 200 fs while the DIRA (cosine of the angle between the B momentum and the line passing through the primary and B decay vertices) is required to be higher than 0.9998.

Offline analysis selection

The offline final selection refines the cuts of the stripping selection, furthermore it adds flight-distance and PID information. The separation of production and decay vertices of D^0 and $B^\pm$ mesons are estimated by calculating the χ^2 ("Flight Distance" χ^2) obtained forcing the superposition of the two vertices, the PID information is a $K-\pi$ likelihood related to the probability that a particle is a kaon. Hadronic charged tracks unlikely to be kaons are considered to be pions. The final selections are summarised in table 4.2.

Optimization and structure of the reconstructed masses distribution

In order to study and optimise the selection, pure signal and pure background samples have been used. The pure signal sample is obtained by truth-matched Monte Carlo simulations, while D^0 mass sidebands in LHCb data are used as background samples. This is based on the assumption that the background in B mass spectrum can be represented by events passing all the selections, but with a wrong D^0 mass. This procedure is correct to model the combinatorial background but the model is incomplete because a variety of non-signal events contains a D^0. In particular the loss of a particle or the misidentification of the bachelor track can give rise to a background not present in the sidebands. However there is a limited number of sources of this kind of background which can be studied separately. Since losing a particle shifts the reconstructed B mass towards lower values, this kind of background is said to affect the *Low-Mass* region. A graphical representation of D sidebands and low mass region is given in figure 4.4. The two-peaks structure of the low mass region is due to the helicity properties of $D^{*0} \to D^0\pi^0$ and $D^{*\pm} \to D^0\pi^\pm$, reconstructed as a D^0 because of the loss of the pion. It can be shown that θ, defined as the angle between the $B^\pm$ and D^0 flight directions in the D^{*0} rest frame, because of the helicity of the particles involved, follows a distribution proportional to $\cos^2\theta$. Another contribution to the low mass region, with lower branching ratio, is given by $D^{*0} \to D^0\gamma$ decays with the photon loss. In this case the decay

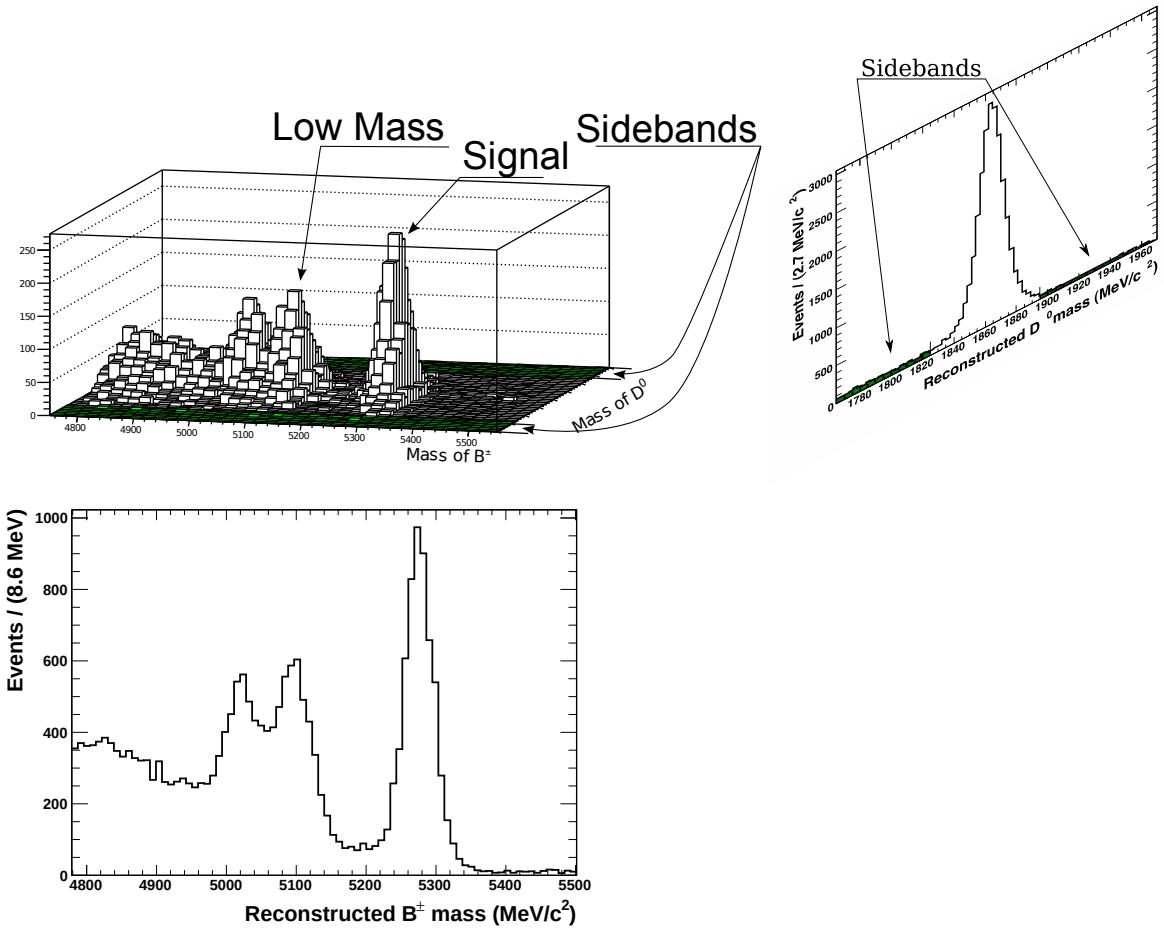

Figure 4.4: A graphical representation of the region called Low Mass and of the sidebands. The bidimensional histogram has been obtained for the $B^{\pm} \to D^0(K^{\pm}\pi^{\mp})\pi^{\pm}$ channel after all of the selections have been applied (except for the D^0 mass window). The two unidimensional histograms are projection over the two axes.

distribution in θ is proportional to $\sin^2\theta$. Figure 4.10, where Low-Mass contributions are split according to the originating B decay, qualitatively confirms expectations.

This means that the kinetic energy of the D^0 in the lab frame follows a doubly peaked distribution, the lower energy peak corresponding to the back-emitted D^0, the higher energy one corresponding to the forward-emitted D^0 (a more detailed analysis is reported in the section 5.1.3).

The study of these selections has been achieved developing a simple framework (*Leaf End-user Analysis Framework*) usable for various charmed B decays analyses. In particular it has been used for D^0 and D^{*0} selections. Leaf has been developed to run in parallel sessions for multiple analyses and is open to future extension for working on the LHC Computing Grid (LCG) [37]. A brief description of this framework, that I developed during my training period, is given in appendix B.

4.2.5 Multiple Candidates

After all the selections have been applied it is possible to have more than one candidate per event in the sample to be used for the fit. This problem is common to many analyses [38] and is mostly due to three main cases.

- *Clone candidates* share at least one cloned track, *i.e.* a track reconstructed twice. Cloned tracks are quite common so that the tracking software provides a clone suppression algorithm based on the Kullback-Liebler (KL) distance [39]. However it is possible that some clone candidates are not recognised by the reconstruction software affecting the fit result. To

remove clones from the final sample, a test on the angle between each pair of tracks has been implemented.

- *Overlap candidates* share at least a reconstructed track. A common example concerning the analysis of $B \to Dh$ with $D \to hh$ is the exchange of one of the D daughter tracks with the bachelor track. If the momentum of the two particles is similar, the reconstructed D mass can lie in the selection mass window so that both combinations are present in the final sample.

- *Genuine candidates* are real candidates in the same event. This is quite unlikely in data, because the branching ratio of $B \to Dh$, with $D \to hh$ is at most of $\mathcal{O}(10^{-4})$. In Monte Carlo simulations producing $B\bar{B}$ pairs, one of the B mesons is forced to decay in the analysis channel, while the other follows the world averaged branching ratios [24]. Background characterisation shouldn't rely on the single candidate assumption.

As an example, the classification of multiple candidates for of Right Sign analyses is given in table 4.3. The number of events per sample is given as a normalization for the number of multiple candidates. However one can observe that, since the same number of MC events ($\sim 1.5 \times 10^6$) has been generated for the Cabibbo Favoured ($B \to D^0\pi$) and the Cabibbo Suppressed ($B \to D^0K$) channels, the ratio between MC and data generated events is higher for the CS (~ 47) than for the CF (~ 3) channel, but in both the cases the MC statistics is enough to make statistical errors negligible in this preliminary analysis. One can observe that the purity of the Cabibbo Favored selection is definitely higher than for the Cabibbo Suppressed channel. As expected, the number of genuine multiple candidates is almost null ($< 10^{-4}$). The clone multiple candidates dominate. Since clone candidates in a same event are substantially equivalent (because they share very similar values for the reconstruction variables), eliminating clones requires a smaller effort than eliminating overlaps. Indeed the difference between the B masses reconstructed for two clone events is usually tiny, and a wrong choice would not change significantly the B mass distribution, which is used to measure the event yield. The correlation between the reconstructed masses for each pair of multiple candidates is shown in figure 4.5 in the Monte Carlo simulation at left and in data at right.

After the classification, genuine multiple candidates are kept, while among overlap and clone candidates for each event the one with highest p-value[2] associated to the reconstruction of the B decay vertex (quality parameter) is the only to be selected. The p-value is evaluated from the fit of the reconstructed track for the D^0 meson and the bachelor track forcing an intersection point, which is interpreted as the B decay vertex. This is considered to be a good quality test because it

[2]Given a pdf $f(x)$, the p value is a statistical test associated to a point x_0 defined as $p = \int_{x_0}^{+\infty} f(x)\mathrm{d}x$. Often, it is used to estimate the quality of a fit considering the minimum χ^2 against the χ^2 distribution for a given number of degrees of freedom. By design, the p value can take values between 0 and 1, the higher is the p-value, the higher is the fit quality.

	$B^\pm \to \pi^\pm D^0(K^\pm\pi^\mp)$			$B^\pm \to K^\pm D^0(K^\pm\pi^\mp)$		
	MonteCarlo	Data	Background	MonteCarlo	Data	Background
Events						
Generated/Produced	1.53×10^6	419×10^3	-	1.51×10^6	32×10^3	-
Selected	67122	22687	2574	65900	4091	990
Multiple Candidates						
Genuines	2	0	0	0	0	0
Overlaps	4	1	2	0	14	5
Clones	832	259	27	989	43	8

Table 4.3: Classification of multiple candidates for Right Sign analyses in three categories, see the text for definitions. The number of generated MC events is an output of the MC generator. The number of event produced at LHCb is an estimation calculated as $2 \times \sigma \times B_F \times \int \mathcal{L}\,\mathrm{d}t$, where σ is $b\bar{b}$-production cross section in the LHCb acceptance, B_F is the PDG [24] branching ratio for the considered decay chain and $\int \mathcal{L}dt$ is the LHCb integrated luminosity. The factor 2 indicates that both b and $\bar{b}$ can contribute to the decay chain. It has to be remarked that the event selection, at this stage, does not rely on a tight the B mass window cut. The B mass for selected events is only required to be higer than 4780 MeV/c^2

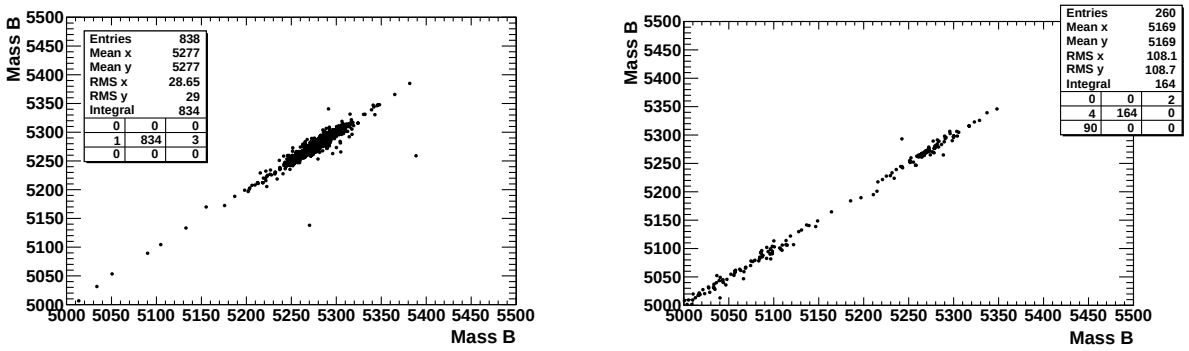

Figure 4.5: Scatter plot of the reconstructed B masses for each pair of multiple candidates in a MC simulation (left) and in the data sample (right). The masses are expressed in MeV/c^2.

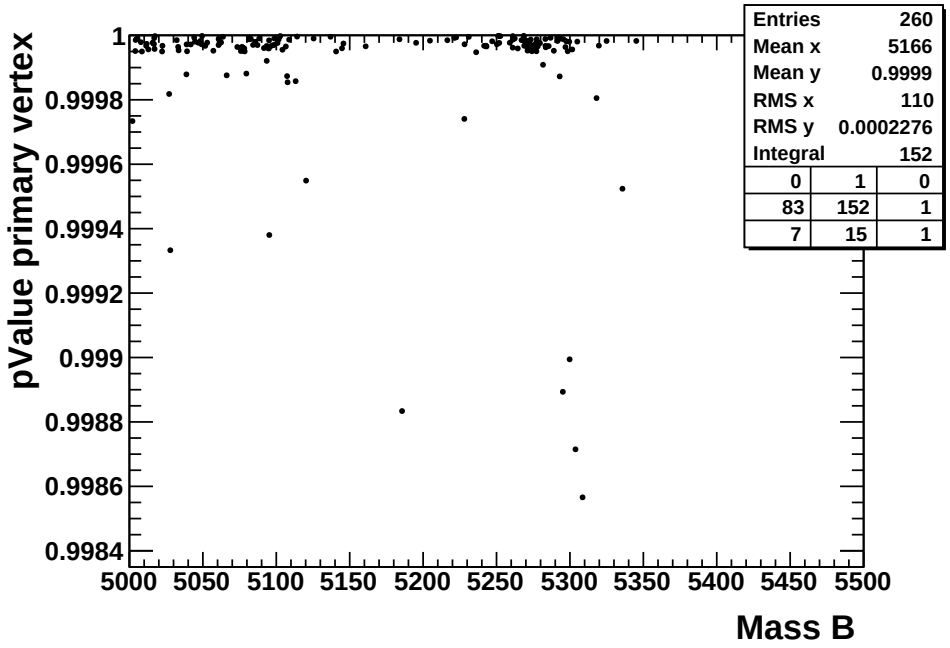

Figure 4.6: Scatter plot of the B mass against the p-value associated to the reconstruction of the B decay vertex for candidates in multiple candidate events (mostly clones). The correlation parameter is $\sim 1\%$.

includes information on the reconstruction of the D and B, so that the highest p value is expected to be associated to the best reconstructed candidate.

This *"taking the best"* method can *a priori* introduce a bias in the final fit, but it has been shown that there is no significant correlation between the vertex reconstruction p-value and the reconstructed mass of the B meson. The correlation parameter between the two variables is about 1%. The scatter-plot of B meson mass against the quality parameter for candidates in multiple candidate events is shown in figure 4.6.

4.2.6 Signal and background studies.

In order to model the probability density function (pdf) of the reconstructed B mass, Monte Carlo simulation is used. It is a good practice to give parametric expression to pdf whenever it is possible, in order to allow parameters to be adapted to real data in the fitting algorithm. In particular, the mean value of the pdf and the standard deviation can be slightly different in Monte Carlo and data because of systematic calibration errors and non-perfect resolution reproduction in Monte Carlo, respectively.

To represent the signal peak, a non-Gaussian pdf has been used because a radiative low-mass

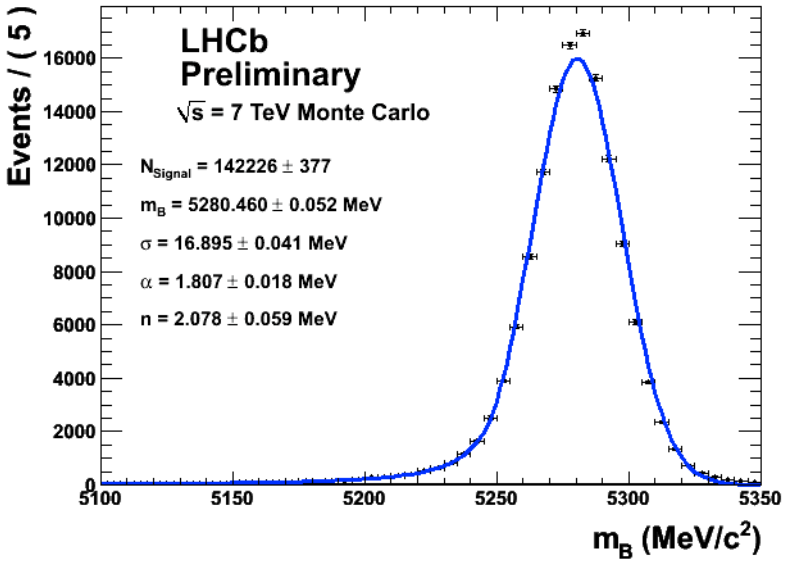

Figure 4.7: Single Crystal ball distribution (blue solid line) fitting the MC simulated B mass distribution for $B^{\pm} \to D^0\pi^{\pm}$ decays with $D^0 \to K^{\pm}\pi^{\mp}$ (black points with error bars).

tail is present. Hence a more complex pdf parametric expression has to be provided. A possible choice, giving good results with a limited number of parameters, is to fit the signal distribution with a Crystal Ball distribution. The Crystal Ball pdf $\mathcal{C}(m)$ has four parameters: the peak value m_0, the width of the central Gaussian σ, and the tail parameters α and n. It is defined as

$$\mathcal{C}(m) \equiv \begin{cases} \exp(-\frac{t^2}{2}) & (t \geq -|\alpha|) \\ \frac{A}{(B-t)^n} & (t < -|\alpha|) \end{cases} \qquad \text{with} \begin{cases} A = \left(\frac{n}{|\alpha|}\right)^n \exp(-\frac{1}{2}|\alpha|^2) \\ B = \left(\frac{n}{|\alpha|} - |\alpha|\right) \\ t = \text{sign}(\alpha)\frac{m-m_0}{\sigma} \end{cases} \tag{4.2}$$

In figure 4.7 the MC distribution of the reconstructed B mass for $B^{\pm} \to D^0\pi^{\pm}$ decays with D^0 forced to decay to $K^{\pm}\pi^{\mp}$ (favored channel) is shown. The superposed blue line is the fitted Crystal Ball pdf. Since the agreement is not perfect, the collaboration has studied more complex parametric pdf to represent the signal. At the time of writing the best result has been obtained with a double Crystal Ball, *i.e.* a Crystal Ball with two tails, but further improvements are possible.

When the fit algorithm is applied to the data sample, the peak value and the width are free parameters, while the tail parameters are fixed to the values resulting from the fit to MC samples.

The most important source of background is the mis-identification (misID) of the bachelor track. Considering the $B \to DK$ channel, $B \to D\pi$ decays with the pion identified as a kaon are a source of background in the reconstructed B mass signal range.

In the case of a two body decay (at rest) of a particle of mass M_{parent} to two particles of mass m_1 and m_2 with momentum $p_{\text{daughters}}$, if the daughter particle of mass m_1 is mis-identified as a particle of mass $\overline{m}_1$, the displacement in the reconstructed mass of the parent particle is given by the expression

$$\delta M \simeq \frac{\sqrt{m_2^2 + p_{\text{daughters}}^2}}{M}\left(\sqrt{\overline{m}_1^2 + p_{\text{daughters}}^2} - \sqrt{m_1^2 + p_{\text{daughters}}^2}\right) \tag{4.3}$$

where

$$p_{\text{daughters}} = \sqrt{\left(\frac{M_{\text{parent}}^2 + m_1^2 - m_2^2}{2M_{\text{parent}}}\right)^2 - m_1^2} \tag{4.4}$$

For a B meson decaying to DK and reconstructed as $D\pi$ the shift in the mean value of the reconstructed mass is about 30 MeV/c^2 towards lower mass values. The mass profile of this background

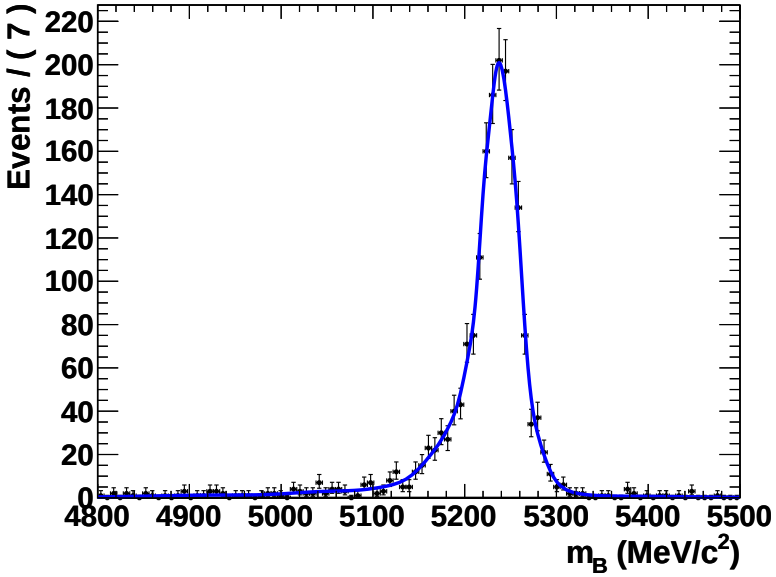

Figure 4.8: Non parametric probability density function (solid blue line) for the contamination from $B \to DK$ decays identified as $B \to D\pi$ (MC simulated and represented as black dots with error bars).

source has been studied using Monte Carlo simulations and reproduced with a non-parametric pdf [20]. The Monte Carlo simulation of $B \to DK$ decays reconstructed as $B \to D\pi$ is shown in figure 4.8. The peak shift towards lower masses is ~ 40 MeV/c^2, slightly larger than expected but still consistent.

The same procedure is used to reproduce low mass background samples. After having noticed a difference between the Monte Carlo and data samples as a shift of the three peak values (signal peak and low mass structure) approximated with three local Gaussian fits, an equivalent shift (4 MeV/c^2) has been applied to the MC sample to correct this aspect. Since the pdf is non-parametric, it is impossible to leave this shift as a free parameter as it has been done for the signal pdf.

I have also explored an alternative technique, using numerical integration to convolute a 2 free-parameter Gaussian with the non parametric fit function. The convolution Gaussian introduces in the fit a translation and a spread of the pdf depending on the gaussian mean value and standard deviation, respectively. These parameters have been let free for fitting to avoid limitations imposed by the non-parametric nature of the function. However, executing a numerical integration for each fit attempt requires a CPU time which makes the method not worth, thus the fixed shift has been adopted.

Finally, also the background in D mass sidebands is modelled using non-parametric pdf, which reproduces combinatorial background. An example for the $B^{\pm} \to D^0\pi^{\pm}$ is shown in figure 4.9. It is interesting to remark the peak centered at the B mass. It constitutes a non flat background in the signal region due to charmless three body B decays $B^{\pm} \to \pi^{\pm}\pi^{\mp}K^{\pm}$. As these decays do not pass through a D state the invariant mass of each pair of particles is not fixed nor consistent with the D nominal mass. Hence, events of this kind can be selected in the sidebands.

4.2.7 Fit to the data sample

The fit has been implemented using the RooFit [21] package as an unbinned maximum likelihood fit. This method considers a set of N measured quantities $\mathbf{x} = (x_1,\ x_2,\ ...,\ x_n)$ described by a joint probability density function $f(\boldsymbol{x};\boldsymbol{\theta})$ where $\boldsymbol{\theta} = (\theta_1,\ \theta_2,\ ...,\ \theta_N)$ is a set of n parameters whose values are unknown. Considering the fit of the reconstructed B mass distribution, x_i represents the mass reconstructed for i-th selected event while θ_j is the j-th free parameter of the fit: the peak value and the width of the signal pdf; the number of signal, contamination, sidebands and low-mass background events, evaluated as the normalization of the underlaying pdf. The pdf's involved in

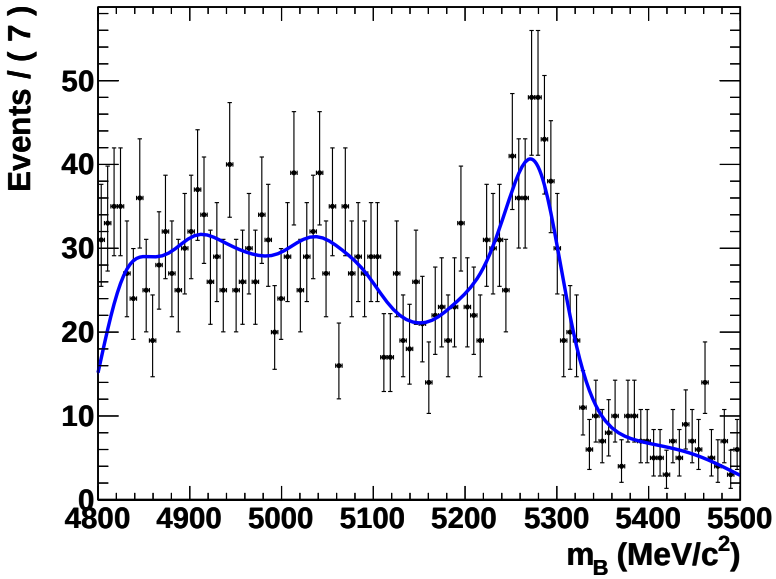

Figure 4.9: Non parametric distribution function fitting (blue solid line) the sideband background. The peak centered at the nominal B mass is due to charmless three body B decays $B^{\pm} \to \pi^{\pm}\pi^{\mp}K^{\pm}$ (black points with error bars).

the fit are described in the previous section. Furthermore a Gaussian function is introduced in the fit to take into account a smooth combinatorics background visible in the lowest mass region, but not fully characterized.

The likelihood function is given by the probability density function evaluated with the data $\boldsymbol{x}$, but viewed as a function of the parameters, *i.e.* $L(\boldsymbol{\theta}) = f(\boldsymbol{x}, \boldsymbol{\theta})$. If, as in our case with x_i being the reconstructed B mass in the i-th event, the measurements x_i are statistically independent and each one follows the pdf $f(x; \boldsymbol{\theta})$ then the likelihood function can be written as

$$L(\boldsymbol{\theta}) = \prod_{i=1}^{N} f(x_i, \boldsymbol{\theta}) \tag{4.5}$$

The combination $\hat{\boldsymbol{\theta}}$ which maximizes the likelihood is considered to represent the best estimation of the value of $\boldsymbol{\theta}$ parameters; in the particular case of the reconstructed B mass, we are interested in the estimation of the signal yield.

Usually it is preferred to maximize the logarithmic likelihood $\ln L$ or LL, by solving the system of simultaneous equation

$$\frac{\partial \ln L}{\partial \theta_i} = 0, \qquad \text{for } i = 1, ..., n \tag{4.6}$$

The RooFit package offers a simple tool to fit a data set with a defined pdf, without writing the minimization algorithm.

The combinatorial background is estimated using the reconstructed B mass in the sidebands data sample. The study of sidebands can also be used to normalize the number of expected combinatorics events in the signal region. This strategy has been adopted when the contamination from $B \to D\pi$ decays identified as $B \to DK$ is not present or can be neglected.

The low-mass structure is modeled as a superposition of different background channels whose relative normalization is an input parameter for the fit. The global normalization of the low mass structure, instead, is a free parameter of the fit.

The estimation of the relative normalization of the low mass channels is structured in two steps: the evaluation of the reconstruction efficiency of each channel from Monte-Carlo and the estimation of the number of events produced at LHCb based on the available integrated luminosity ($\int \mathcal{L} \mathrm{d}t \simeq 37$ pb^{-1}), cross section information [34] and branching ratios [24].

$\mathbf{B} \to \mathbf{D}\pi$ Channel	Generated [kEvents]	MC selected [events]	Efficiency [$\times 10^{-3}$]	B. R. [$\times 10^{-3}$]	Exp. Production [$\times 10^{6}$]	Exp. events [$\times 10^{3}$]	% events
$B^+ \to D^0 K^*$	100	70	0.7	0.53	0.435	0.30	0.060
$B^0 \to D^0 \rho^0$	500	11682	23.4	0.32	0.262	6.13	1.2
$B^0 \to D^{*+} \pi$	1031	74769	72.5	2.76	2.26	164	32
$B^+ \to D^{*0} K^+$	1052	1874	1.78	0.421	0.345	0.61	0.12
$B^0 \to D^{*+} K^-$	1044	1716	1.64	0.214	0.176	0.28	0.057
$B^+ \to D^{*0} \pi$	1033	81238	78.6	5.19	4.26	334	66
					SUM:	506.2	100

Table 4.4: Table of generated and reconstructed Monte Carlo events for the low mass background channels in the $B \to D\pi$ analysis. The aim is to calculate the relative weight (% events) of the different channels composing the low mass background pdf.

$\mathbf{B} \to \mathbf{DK}$ Channel	Generated [kEvents]	MC selected [events]	Efficiency [$\times 10^{-3}$]	B. R. [$\times 10^{-3}$]	Exp. Production [$\times 10^{6}$]	Exp. events [$\times 10^{3}$]	% events
$B^+ \to D^0 K^*$	100	3345	0.34	0.53	0.435	14.5	19.5
$B^0 \to D^0 \rho^0$	500	483	0.97	0.32	0.262	0.253	0.34
$B^0 \to D^{*+} \pi$	1031	2968	2.9	2.76	2.26	6.52	8.74
$B^+ \to D^{*0} K^+$	1052	82868	79	0.421	0.345	27.19	36.4
$B^0 \to D^{*+} K^-$	1044	78626	75	0.214	0.176	13.2	17.75
$B^+ \to D^{*0} \pi$	1033	3100	3.0	5.19	4.26	12.7	17.15
					SUM:	74.5	100

Table 4.5: Table of generated and reconstructed Monte Carlo events for the low mass background channels in the $B \to DK$ analysis.

The expected number of produced events is estimated as

$$\mathcal{N}_{events} = \int \mathcal{L} \times \sigma_{b\bar{b}} \times 2 \times f_u \times \mathcal{B}r(B \to DX) \times \mathcal{B}r(D \to K\pi) \tag{4.7}$$

f_u is the fragmentation function, *i.e.* the probability for a b quark to produce a $B^{\pm}$ (composed of a b and a u (anti-) quark) rather than a B_d^0 ($\bar{b}u$) or a B_s^0 ($\bar{b}s$). The fragmentation fractions f_d, f_u and f_s are approximately constant as a function of the energy ($\sqrt{s}$), and $f_d \simeq f_u \simeq 40\%$. The factor 2 in equation 4.7 is due to the observation that either the b or the $\bar{b}$ can hadronize and decay in the analyzed channel.

The fit of the channel $B \to Dh$ with $D \to K\pi$ is given in figure 4.10. The fit on $B \to D\pi$ and $B \to DK$ CP-even channels ($D^0 \to K^+K^-$ or $D^0 \to \pi^+\pi^-$) are represented in figure 4.11 and 4.12, respectively.

4.2.8 Relative efficiencies cross check

In the analysis described above I have assumed that the relative efficiencies for the different low-mass background channels are well reproduced in MC simulations. This assumption can be verified considering the ratio $\mathcal{R}_\epsilon$ between the efficiencies obtained reconstructing the signal and various low-mass background channels. If the relative efficiencies are well reproduced in MC, this ratio should be consistent between Data and Monte Carlo samples. For the data sample $\mathcal{R}_\epsilon^D$ is defined as the ratio between the signal and background yields calculated through the fit. For Monte Carlo, $\mathcal{R}_\epsilon^{MC}$ is calculated from the expected yields, namely

$$\mathcal{R}_\epsilon^{MC} = \frac{N_B \times Br(\text{low-mass channel}) \times \epsilon_{\text{low-mass channel}}}{N_{B^\pm} \times Br(\text{signal}) \times \epsilon_{\text{signal}}} \tag{4.8}$$

where N_B is the number of parent B mesons produced (which can be B^0 or $B^\pm$ according to the considered low-mass channel) and ϵ is the global efficiency estimated with MC. This normalization is required to compare MC and data sample. Since the strong interaction is blind to the electric charge, N_{B^0} is considered to equal $N_{B^\pm}$. The uncertainty on $\mathcal{R}_\epsilon^{MC}$ is dominated by the error on the $B^\pm$ decays branching ratios, the statistical error on the efficiency is an order of magnitude smaller

Low Mass Background	$B^{\pm} \to D^0\pi^{\pm}$ analysis $\mathcal{R}_\epsilon^{MC}$ (%)	$\mathcal{R}_\epsilon^{D}$ (%)	$B^{\pm} \to D^0K^{\pm}$ analysis $\mathcal{R}_\epsilon^{MC}$ (%)	$\mathcal{R}_\epsilon^{D}$ (%)
$B^{\pm} \to D^0K^{*\pm}$	0.09 ± 0.01		48 ± 8	
$\overline{(-)}{B}^0 \to D^0\rho^0$	1.6 ± 0.3		0.53 ± 0.13	
$\overline{(-)}{B}^0 \to D^{*\pm}\pi^{\mp}$	43 ± 3		13 ± 1.8	
$B^{\pm} \to D^{*0}K^{\pm}$	0.19 ± 0.02		88 ± 15	
$\overline{(-)}{B}^0 \to D^{*\pm}K^{\mp}$	0.09 ± 0.01		43 ± 7	
$B^{\pm} \to D^{*0}\pi^{\pm}$	90 ± 7		25 ± 4	
Total	135 ± 11	125 ± 4	218 ± 36	188 ± 30

Table 4.6: Comparison between the efficiency ratios R_ϵ evaluated in Monte Carlo and Data samples.

Channel	**Yield**
$B^{\pm} \to D^0\pi^{\pm}$ with $D^0 \to K^{\pm}\pi^{\mp}$	5158±86
$B^{\pm} \to D^0\pi^{\pm}$ with $D^0 \to K^+K^-$	286 ±20
$B^{\pm} \to D^0\pi^{\pm}$ with $D^0 \to \pi^+\pi^-$	121 ±14
$B^{\pm} \to D^0K^{\pm}$ with $D^0 \to K^{\pm}\pi^{\mp}$	391 ±26
$B^{\pm} \to D^0K^{\pm}$ with $D^0 \to K^+K^-$	36 ± 8
$B^{\pm} \to D^0K^{\pm}$ with $D^0 \to \pi^+\pi^-$	10 ± 7

Table 4.7: Number of events obtained by the fit for the six channels analysed. The integrated luminosity is 37 pb^{-1} and the uncertainties are statistical only.

and is neglected. The uncertainty on $\mathcal{R}_\epsilon^D$ is obtained from the uncertainty on fit parameter. The comparison of the ratio $\mathcal{R}_\epsilon$ in the two samples is given in table 4.6.

The agreement between Data and Monte Carlo is fairly good, even if R_ϵ^D is slightly lower than the Monte Carlo expectation. This can be due either to an over-estimation of the low-mass background yield, or to an under-estimation of the number of recorded signal events. As mentioned before, this preliminary analysis is conservative in the estimation of the signal yield, thus this result should not be surprising.

This Low-Mass Background/Signal relative efficiency cross check can be very useful when different fit strategies are considered.

4.2.9 Considerations about the efficiency

The equation 4.7 can be used to estimate the number of expected signal events produced in 37 $pb^{-1}$of integrated luminosity. The efficiency can thus be evaluated as the ratio between the number, evaluated through the fit procedure, of reconstructed events, and the expected number of produced events. In table 4.8 the number of events generated and reconstructed in Monte Carlo simulations, as well as produced and reconstructed in data, are summarized for both $B \to D\pi$ and $B \to DK$ channels. The ratio between the reconstruction efficiency in Monte Carlo and in data is expected to be unity if the analysis is equivalent for Monte Carlo and Data samples, however it is 3.5 for $B \to D\pi$ channel and 3.6 for the $B \to DK$, which indicates that something is not completely understood. Even if the same selection cuts have been applied to both MC and data samples, it is possible that the disagreement between data and Monte Carlo distributions analyzed previously introduces a difference in the efficiency. Another possible source is the fit, but is unlikely that the procedure may introduce an error as large as a factor 3.

Another possible explanation is a difference between the phase space for MC particle generation and that for the measured cross-section used in the production yield estimation. Indeed, while the cross-section used in the evaluation of *produced* data events is measured for b-hadron production in the pseudo-rapidity region $2 < \eta < 6$, events *generated* by the MC are required to have all b-hadron daughter particles in the geometrical acceptance of the detector. The difference between these two conditions can cause a disagreement between data and MC.

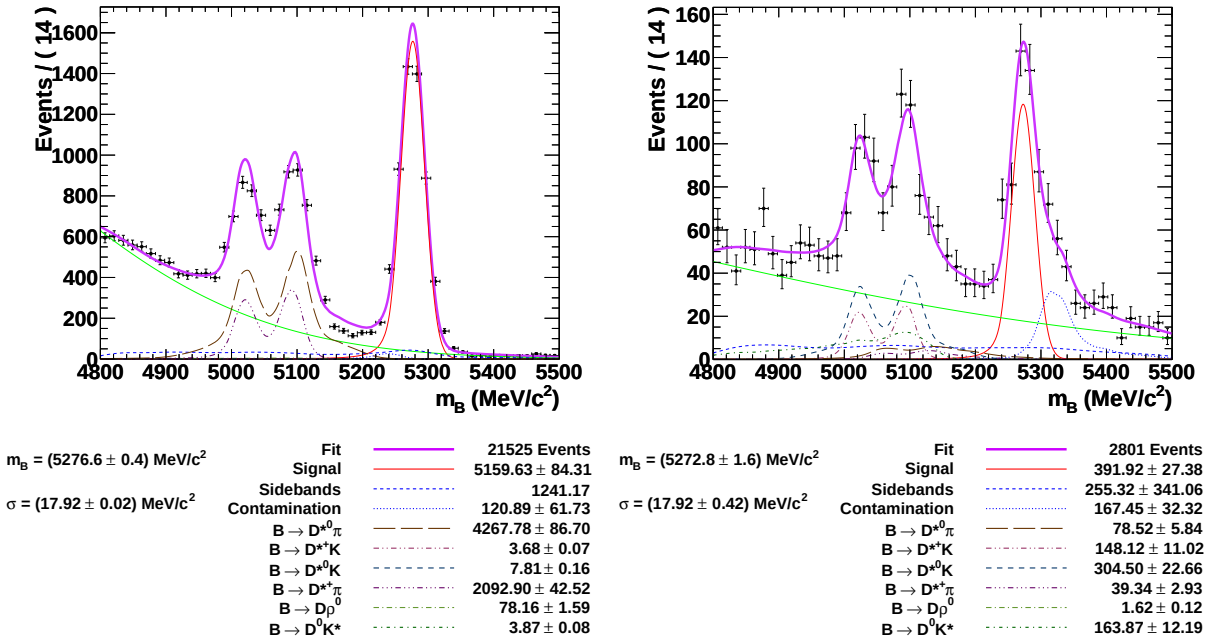

Figure 4.10: Fit of the B mass pdf of the channels $B \to D\pi$ (left) and $B \to DK$ (right), with $D \to K\pi$. The legend reports the number of events for the signal, sidebands and contamination components. The contribution to the low mass region from channels containing D^* is sizable.

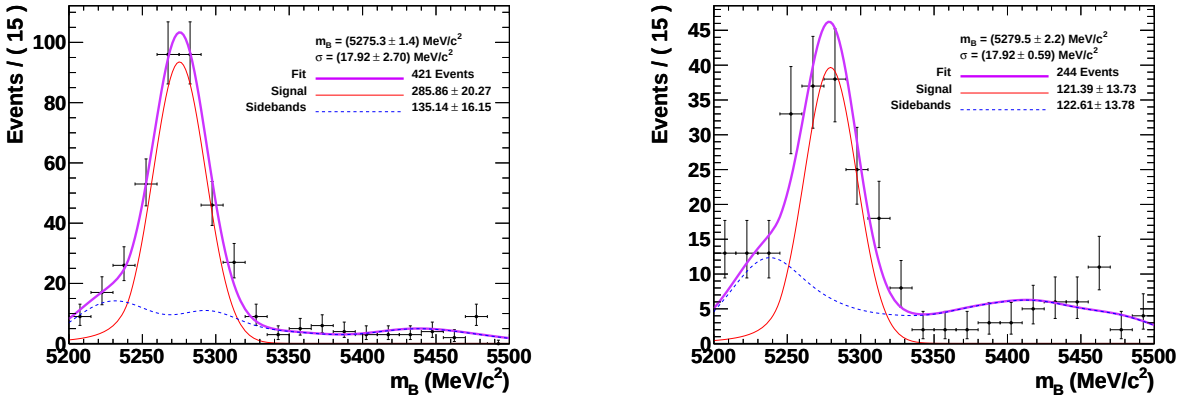

Figure 4.11: Fit of the reconstructed B mass for the favoured CP-even modes: $B^\pm \to D^0\pi^\pm$ with $D \to K^+K^-$ (left) and $D \to \pi^+\pi^-$ (right). The low mass region has not been reconstructed because the MC for the background channels is not yet available.

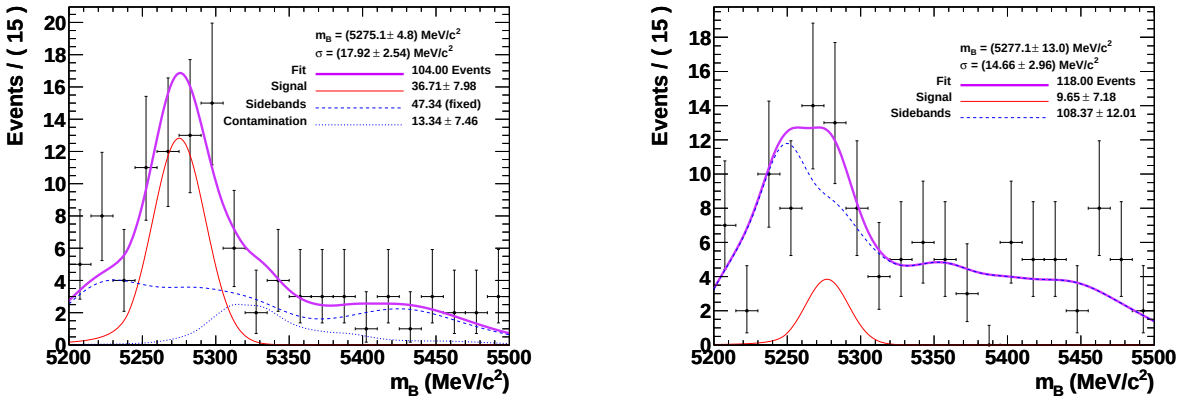

Figure 4.12: Fit of the reconstructed B mass for the suppressed CP-even modes: $B^\pm \to D^0K^\pm$ with $D^0 \to K^+K^-$ (left) and $D^0 \to \pi^+\pi^-$ (right). The low mass region has not been reconstructed because the MC for the background channels is not yet available.

	Monte Carlo			Real Data (from Fit)			
	Generated	Reconstructed	ϵ_{MC} (%)	Produced	Reconstructed	ϵ_D(%)	ϵ_{MC}/ϵ_D
$B \to D\pi$	1.5×10^6	66053 ± 257	4.33	$(420 \pm 79) \times 10^3$	5158 ± 84	1.23 ± 0.23	3.5
$B \to DK$	1.5×10^6	66861 ± 259	4.38	$(32 \pm 7) \times 10^3$	391 ± 46	1.23 ± 0.29	3.6

Table 4.8: Comparison between the reconstruction efficiencies in Monte Carlo and data. The ratio ϵ_{MC}/ϵ_D, different from the unity, suggests that something is not entirely understood in the selection chain or in the MC generation.

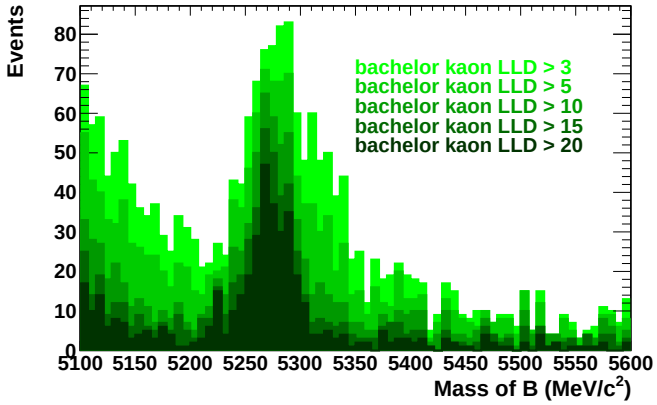

Figure 4.13: B mass distribution changing the PID threshold. The mass peak shifts evidently towards lower values.

4.2.10 Conclusions on $B^{\pm} \to D^0 h^{\pm}$ channels

Even if the final fit seems to well reproduce the data sample, there are still some factors not well under control. The reconstructed B mass in the DK channel is shifted towards lower values by about 6 MeV, which may be symptomatic of a bad representation of the contamination. Changing the PID threshold one can observe that the peak shifts, which is evidence of a correlation between the PID cut and the B mass distribution. A possible explanation of such a correlation could be that the misidentification through RICH detectors is less efficient for high energy particles. A harder cut on the PID can thus reduce the number of higher energy kaons, biasing the reconstructed mass distribution. The peak shift towards lower values is represented in figure 4.13.

The reconstruction efficiency of Monte Carlo simulation and data samples are quite different, the cause can be that the phase space of generated and produced b-hadrons is not the same, or some reconstruction and selection step not sufficiently well understood. Finally the selections are not sufficiently optimised to make the measurement of the suppressed channels precise enough, multivariate analysis will be attempted in the future to enhance signal selection and background rejection.

Extrapolating the observed ~ 46 $B^{\pm} \to D^0 K^{\pm}$ CP-even events (36 from $D^0 \to K^+K^-$ and 10 from $D^0 \to \pi^+\pi^-$, see table 4.7) to a luminosity of 1 fb^{-1} expected for the end of 2011, a CP-even yield of ~ 1300 events is expected to be available, corresponding to 2.8 times the statistics of *BABAR* (477 events), anticipating a doubled precision on $\mathcal{A}_{CP+}$ and $\mathcal{R}_{CP+}$. However, while the *BABAR* yield has been obtained with highly optimized multivariate analyses, the LHCb yield is estimated with a fairly optimized, cut based analysis. Indeed, the aim of preliminary analyses is to understand and describe properly each step, from the trigger to the background contribution in the final fit. The future employment of optimized multivariate analysis techniques at LHCb will increase significantly the selection efficiency. Then the CP-even yield expected for the end of 2011 will further increase beyond this first, rough, 1300 events extrapolation.

Chapter 5

Preliminary tests on $B^{\pm} \to D^{*0}h^{\pm}$ channels

As discussed in the theoretical introduction, B decays to a D^{*0} resonance can add important constraints [33] to the measurement of γ, offering additional observables for both GLW and ADS methods. The $D^*(2007)^0$ resonance, commonly referred to as D^{*0}, decays to $D^0\gamma$ with a branching fraction of about 38.1% or to $D^0\pi^0$ with a branching fraction of 61.9%. π^0's decay to two photons with a branching ratio of 99.8%.

For many aspects, the study of these channels is similar to the analysis presented in the previous chapter, however the difficulty of measuring low energy photons in the final state at LHCb makes the analysis more challenging. The LHC environment is in fact overwhelmed by low transverse momentum (p_T, the component of the momentum p orthogonal to the beam axis) photons originated from many minimum bias[1] π^0's.

This chapter summarizes the original contribution of my work in the LHCb collaboration.

5.1 Selections

Trigger and stripping algorithms are the same used for the D^0 analysis; as we have seen on figure 4.10, the $D^{*0}h^{\pm}$ signal is a contamination for $D^0h^{\pm}$, when the soft π^0 or photon is lost. The selected charged tracks and photon(s) are therefore used to reconstruct and filter $D^{*0} \to D^0(h_1h_2)\pi^0/\gamma$. Also the same selection thresholds have been used, adding some cut over variables related to the neutral particle (the photon or the neutral pion). In particular two cuts have been added: a mass window on the the reconstructed D^{*0} and a combined cut on kinematics and helicity structure, furthermore the collaboration prescriptions on the neutral particle identification have been adopted.

As before, the background sample has been obtained from D mass sidebands, imposing the additional condition that the mass of the reconstructed D^{*0} is outside the signal box (defined below).

5.1.1 Neutral particle identification confidence level

The collaboration experts for the electromagnetic calorimeter particle identification have defined a variable called *Particle Confidence Level* (PCL) which represents the confidence level on a specific particle identification hypothesis. For example, when for a neutral particle the photon hypothesis is considered, the associated PCL assumes a value in the range $0 \div 1$, depending on the probability that the particle is really a photon. The PCL is only defined for merged neutral pion[2] and photon candidates, it is obtained from the so called *neutral PID likelihood*, based on ECAL cluster information: the preshower (PS) energy, the cluster energy sharing, and the track matching. Usually the threshold suggested to identify photons is PCL > 0.4. The calorimeter PCL variable

[1] Minimum bias events are due to the many proton-proton collision giving rise to uninteresting, low angle decay chains.

[2] A π^0 is referred to as *merged* if the two produced photons are too close to be distinguishable by the calorimeter.

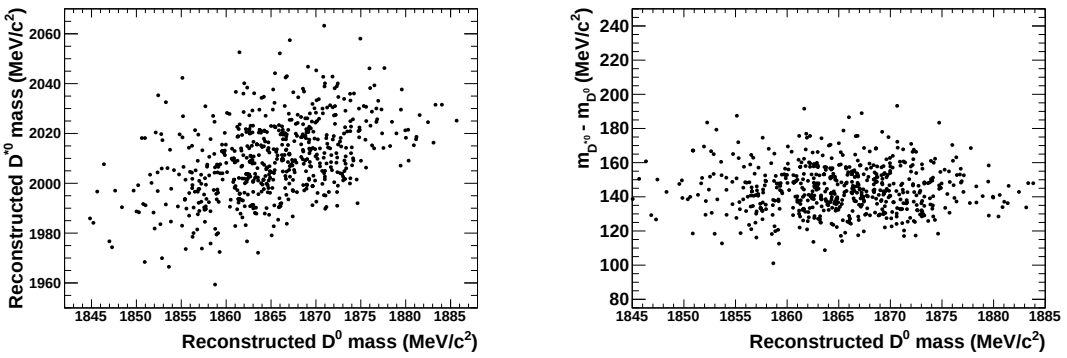

Figure 5.1: At left, scatter plot of the correlation between the mass reconstructed for D^0 and D^{*0} candidates in the MC sample of $B^{\pm} \to D^{*0}\pi^{\pm}$ with $D^{*0} \to D^0\pi^0$ decays. At right, the correlation of the reconstructed mass difference $(m_{D^{*0}} - m_{D^0})$ with the reconstructed D^0 mass.

is often considered to be something internal to the LHCb particle identification libraries handled by calorimetry experts so that in the preliminary analysis it has not been further investigated. However it is a key variable in the reconstruction of $B^{\pm} \to D^{*0}h^{\pm}$ channels, so that a future development of the analysis algorithm will optimize neutral particle identification as all the other variables.

5.1.2 D^{*0} mass window selection

An important cut regarding the D^{*0} resonance considers the difference between the reconstructed masses for D^{*0} and D^0. To cut on this variable is conceptually similar to cut on the D^{*0} mass, but subtracting the D^0 mass makes the distribution peak sharper, the selection can thus be tighter. Indeed an error on the determination of the D^0 mass is automatically propagated to the mass of its parent particle D^{*0}, and nearly cancels in the subtraction. The correlation between the two reconstructed masses is shown in figure 5.1.

The distribution observed in Monte Carlo simulation with D^{*0} decays reconstructed as $D^0\gamma$ is given in figure 5.2 (left). The expected peak value at 142.12 MeV/c^2 is approached by the measured (139.9 ± 0.9) MeV/c^2, with a resolution $\sigma = (13.5 \pm 0.5)$ MeV/c^2. The left peak is due to the loss of a photon produced in the $D^{*0} \to D^0\pi^0$ decays with $\pi^0 \to \gamma\gamma$, which makes the event to be reconstructed as a decay to $D^0\gamma$. The energy of the missing photon is not included in the invariant mass of the D^{*0}-decay products, shifting the peak towards lower values. We are, in fact, using a MC sample where $D^{*0} \to D^0\pi^0$ and $D^{*0} \to D^0\gamma$ are mixed according to their relative branching ratios, to accurately model the cross-feed between the two modes. Indeed the same peak is not visible in figure 5.3 (left), representing the distribution in the same variable for D^{*0} reconstructed as $D^0\pi^0$.

The superposed fit models the peak as a Gaussian. The selection cut is fixed at two standard deviations ($\pm 2\sigma$) from the central value, and it is shown as vertical lines in the figure 5.2 (left). An analogous procedure has been adopted to choose the selection cut for the channel $D^{*0} \to D^0\pi^0$ (figure 5.3, left), where the $D^0\gamma$ decays only contributes as combinatorial background. As previously, the expected peak value is well approximated by the MC peak value of (143.6 ± 0.7) MeV/c^2 with a resolution $\sigma = (13.26 \pm 0.57)$ MeV/c^2. In figure 5.2 and 5.3, at right, the difference between the reconstructed D^{*0} and D^0 masses in data are shown for $D^{*0} \to D^0\gamma$ and $D^0\pi^0$ channels, respectively.

One can observe that, even if the event yield is slightly higher in the $D^{*0} \to D^0\gamma$ plot than in $D^{*0} \to D^0\pi^0$, the purity of the signal is higher in the latter. Indeed the photon channel suffers from a more important combinatorial background since there is no invariant-mass condition, as opposed to the neutral pion channel where two photons, consistent with a π^0 decay, are required as π^0 daughters. Furthermore the higher branching ratio of π^0 channel makes the channel easier to identify.

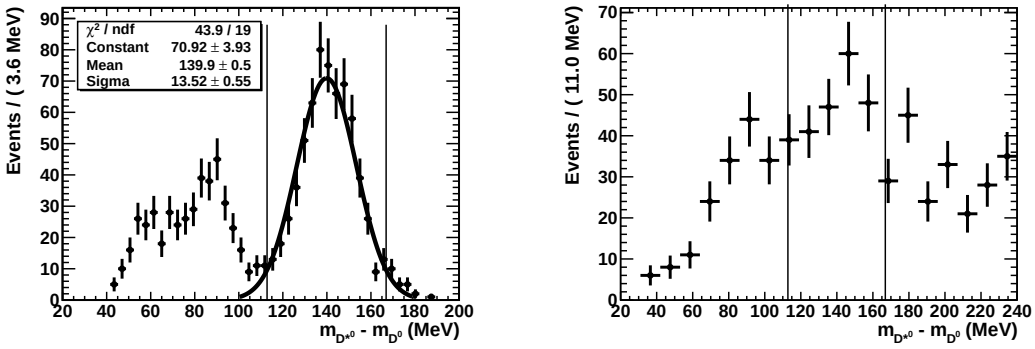

Figure 5.2: Difference between the reconstructed D^{*0} (decaying to $\boldsymbol{D^0\gamma}$) and D^0 masses in Monte Carlo (left) and data (right). The Gaussian fit superposed to MC histogram has been used to optimize the selection defining a symmetric window of ± 30 MeV/c^2 (corresponding to $\pm 2\sigma$) centered on the peak value at 140 MeV/c^2.

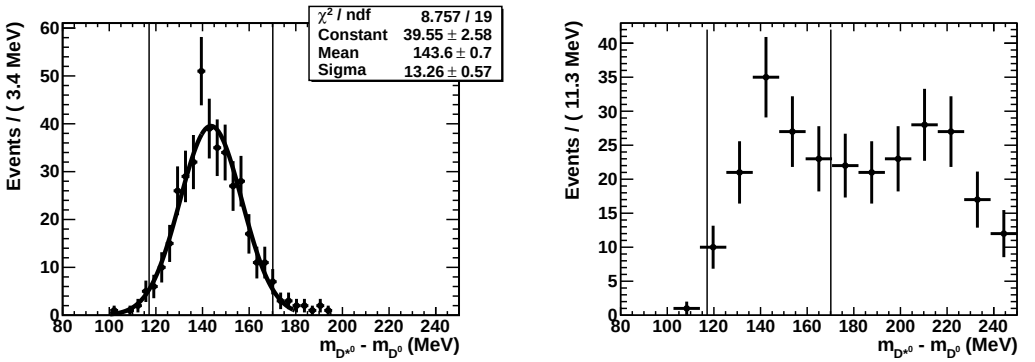

Figure 5.3: Difference between the reconstructed D^{*0} (decaying to $\boldsymbol{D^0\pi^0}$) and D^0 masses in Monte Carlo (left) and data (right). The Gaussian fit superposed to MC histogram has been used to optimize the selection defining a symmetric window of ± 30 MeV/c^2 (corresponding to $\pm 2\sigma$) centered on the peak value at 140 MeV/c^2. The right-side background is probably due to minimum bias π^0 consistent with the hypothesis of a $D^{*0} \to D^0\pi^0$, but with higher energy orby the combination of a $D^{*0} \to D^0\gamma$ with a random photon.

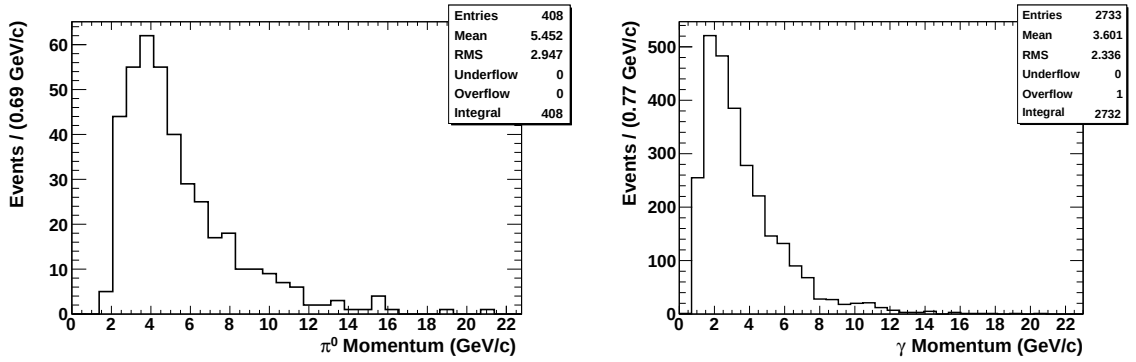

Figure 5.4: Momentum spectra for the pion (left) and the photon (right) of the well reconstructed MC-generated events.

5.1.3 Kinematic selection

Since the mass difference between the D^{*0} and the D^0 meson ($m_{D^{*0}} - m_{D^0} = 2007 - 1865 = 142$ MeV/c^2) is much smaller than the energy scale of the B decay process, these neutral particle (γ or π^0) emitted in the D^{*0} decay is considered to have relatively low energy. The momentum spectra for the neutral particles are shown in figure 5.4. Considering the short D^{*0} and π^0 lifetimes it should not surprise that the kinematics of the decay is analogous to a radiative B decay, with one or two photons in the final state (see figure 5.5). As a consequence the event selection can not rely on cuts on the D^{*0} decay vertex quality nor on D^{*0} flight distance.

Beside charged tracks variables (for which the same criteria as for $B^{\pm} \to D^0 h^{\pm}$ have been used) and the D^{*0} mass, other discriminant variables have been identified and used to define a Fisher discriminant, a linear combination of variables maximizing the separation between the signal and background pdfs. Before discussing the application to D^* channels I briefly introduce this technique.

Fisher discriminant

The Fisher discriminant is a technique which is comprised in a large category of analysis techniques called MultiVariate Analyses (MVAs). The common starting point is the idea of an algorithm which takes an event characterized by a set of variables and classifies the event in a category. Usually the categories are *signal* and *background*, but advanced MVA techniques allows to use more than two categories classifying events in more complex structures. To classify an event, MVAs need to be trained over a sample where the classification is known. The main three classes of MVA techniques are the Fisher discriminant (Fd), the Neural Network (NN) and the (Boosted) Decision

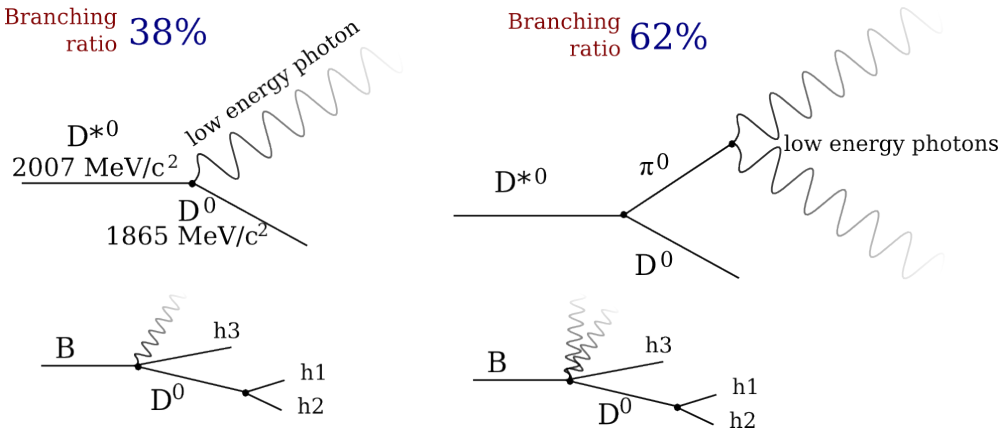

Figure 5.5: Schematic drawing of the D^{*0} decays (top), and of the full $B \to D^{*0}h$ decay chain (bottom). Among the intermediate particles, only the D^0 has sufficient lifetime to make its own flight distance detectable.

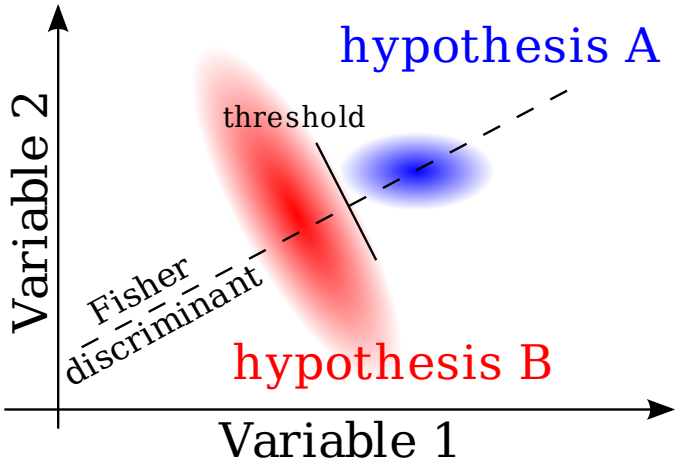

Figure 5.6: A schematic representation of the Fisher discriminant technique in a two-dimensional space.

Tree ((B)DT). Neutral networks and Decision Trees are non-linear techniques which can improve the selection efficiency if compared to the linear Fisher discriminant. However the difficulty of estimating systematics and the long time required for the training often makes the Fisher discriminant favored and more reliable.

The idea of the Fisher discrimination is to maximize the separation between the distributions associated to two hypotheses choosing a linear combination of the discriminant variables. In figure 5.6 a schematic representation of a Fisher discriminant in a two-dimensional variable space is given.

In a multi-dimensional space of variables v_1, v_2 ... v_N, naming $\boldsymbol{\mu}_A$ and $\boldsymbol{\mu}_B$ the mean value of the distribution, and V_A and V_B the covariance matrices for the distribution of hypotheses A and B respectively, one can define the Fisher discriminant variable as the linear combination

$$F_d = a_1 v_1 + a_2 v_2 + ... + a_N v_N \tag{5.1}$$

where $\boldsymbol{a} = (a_1, a_2, ..., a_N)$ is the vector of the Fisher discriminant parameters.

The mean values of distributions associated with the hypotheses A and B, with respect to the Fisher discriminant are

$$\tau_A = \boldsymbol{a} \cdot \boldsymbol{\mu}_A \qquad \tau_B = \boldsymbol{a} \cdot \boldsymbol{\mu}_B \tag{5.2}$$

while the variances of the two distributions will be

$$\Sigma_A^2 = \boldsymbol{a}^T V_A \boldsymbol{a} \qquad \Sigma_B^2 = \boldsymbol{a}^T V_B \boldsymbol{a} \tag{5.3}$$

to maximize the separation between the two distribution one tries to maximize the expression

$$J(\boldsymbol{a}) = \frac{(\tau_A - \tau_B)^2}{\Sigma_A^2 + \Sigma_B^2} = \frac{a_i a_j (\boldsymbol{\mu}_A - \boldsymbol{\mu}_B)_i (\boldsymbol{\mu}_A - \boldsymbol{\mu}_B)_j}{\boldsymbol{a}^T (V_A - V_B) \boldsymbol{a}} \tag{5.4}$$

Imposing the purposely chosen normalization condition $\boldsymbol{a}^T (V_A + V_B) \boldsymbol{a} = \mathbf{1}$, one defines a Lagrangian multiplier problem with Lagrangian

$$\mathcal{L}_F = -\frac{1}{2} \boldsymbol{a}^T B \boldsymbol{a} + \frac{1}{2} \lambda (\boldsymbol{a}^T W \boldsymbol{a} - \mathbf{1}) \qquad \text{with} \begin{cases} B_{ij} = (\boldsymbol{\mu}_A - \boldsymbol{\mu}_B)_i (\boldsymbol{\mu}_A - \boldsymbol{\mu}_B)_j \\ W_{ij} = (V_{A,ij} + V_{B,ij}) \end{cases} \tag{5.5}$$

where λ is an additive scalar variable introduced to impose the normalization constraint. The null derivative minimization condition is equivalent to

$$\lambda \boldsymbol{a} = W^{-1} B \boldsymbol{a} = W^{-1} (\boldsymbol{\mu}_A - \boldsymbol{\mu}_B) \;\; [(\boldsymbol{\mu}_A - \boldsymbol{\mu}_B) \cdot \boldsymbol{a}] = W^{-1} (\boldsymbol{\mu}_A - \boldsymbol{\mu}_B) \xi \tag{5.6}$$

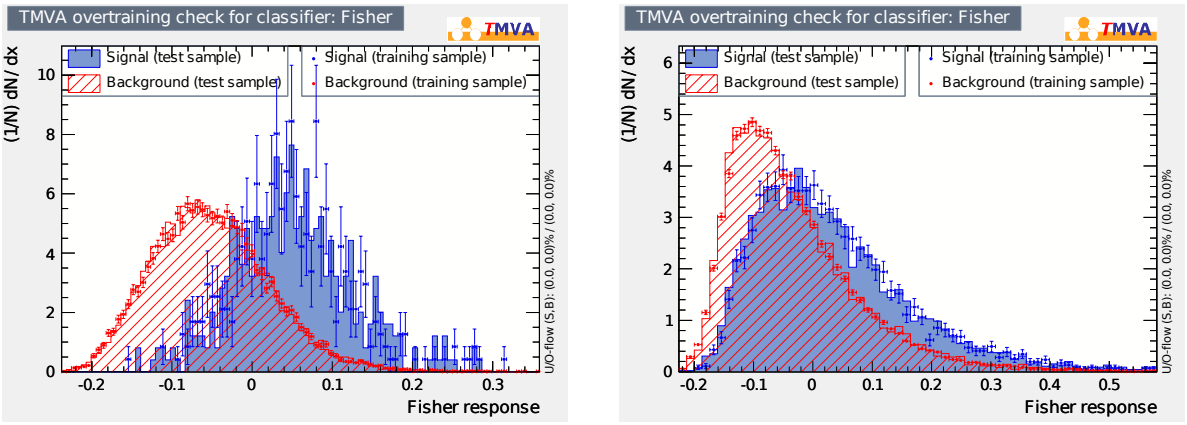

Figure 5.7: Fisher discriminant response for $B^{\pm} \to D^{*0}\pi^{\pm}$ channel analysis, with D^{*0} decaying to $D^0\pi^0$ (left) and $D^0\gamma$ (right). See the text for the list of discriminant variables.

where $\xi = (\boldsymbol{\mu}_A - \boldsymbol{\mu}_B) \cdot \boldsymbol{a}$ is another scalar constant. One can thus conclude that

$$\boldsymbol{a} \propto W^{-1}(\boldsymbol{\mu}_A - \boldsymbol{\mu}_B) \tag{5.7}$$

which is univocally defined imposing the conventional normalization constraint $\boldsymbol{a}^T\boldsymbol{a} = \mathbf{1}$. In conclusion, given the distribution associated to two hypotheses by in a set of variables $\boldsymbol{v}$, the set of parameters $\boldsymbol{a}$ which defines the variable F_d as a linear combination of v_i, maximizing the separation between the two hypothesis can be directly calculated (equation 5.7).

Application to the $B^{\pm} \to D^{*0}\pi^{\pm}$ channel

The Fisher discriminant has been applied to the D^* channel using *T*MVA, a common framework for many different Multi Variate Analyses. Once the problem is set, changing from one technique to another is as simple as modifying a line in the input option file. This framework does not require to really understand the more advanced MVA procedures, which is at the same time the power and the weakness of the tool.

The included variables are:

- the total and transverse momentum of the neutral particle (the neutral pion or the photon from the D^{*0} decays), the D^0 meson, and the bachelor track (the charged particle in the B decay);
- the mass of the neutral pion (in the $D^{*0} \to D^0\pi^0$ channel only); and
- the absolute value of the cosine of the angle θ between the flight directions of B and D^0 mesons in the D^{*0} frame. This helicity angle variable will be discussed in some detail in the next paragraph.

The Fisher discriminant response is shown in figure 5.7 for D^{*0} decaying to $D^0\gamma$ at left, and to $D^0\pi^0$ at right. One can observe that the separation between background and signal is larger for $D^0\pi^0$ channel than for the $D^0\gamma$ one. This is mainly due to the fact that the most discriminating variable is the helicity angle, that, as described below, is much more powerful in the $D^0\pi^0$ case.

The helicity angle

The B decay to $D^{*0}h^{\pm}$, where h is a pseudo-scalar meson, is the decay of a scalar particle to a vectorial and a (pseudo-) scalar particle: $S \to VS$.

In the D^{*0} frame, the momentum of the B meson is

$$\boldsymbol{p}_B = \boldsymbol{p}_{D^*} + \boldsymbol{p}_h = \boldsymbol{p}_h \tag{5.8}$$

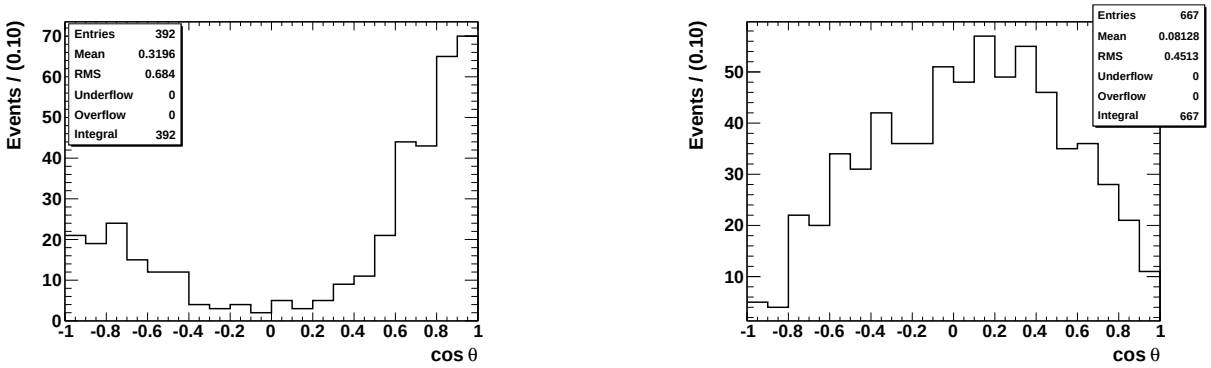

Figure 5.8: Distribution of well reconstructed truth-matched MC events in $\cos\theta$ for $D^{*0} \to D^0\pi^0$ (left) and $D^{*0} \to D^0\gamma$ (right) channels in $B^\pm \to D^{*0}\pi^\pm$ candidate events. θ is defined as the angle between flight directions of B and D^0 mesons in the D^{*0} frame.

where $\boldsymbol{p}_{D^*}$ is zero because of the reference system choice. The classical relation $\boldsymbol{L} = \boldsymbol{r} \times \boldsymbol{p}$ imposes the orbital angular momentum of the initial B state to be orthogonal to $\boldsymbol{p_B}$, namely $\boldsymbol{L_B} \perp \boldsymbol{p_B}$ Since B has zero spin, $\boldsymbol{J_B} = \boldsymbol{L_B}$, hence $\boldsymbol{J_B} \perp \boldsymbol{p_B}$. Analogously, for the pseudo-scalar meson h, one has $\boldsymbol{L_h} \perp \boldsymbol{p_h}$, which can be written as $\boldsymbol{J_B} \perp \boldsymbol{p_B}$. Considering that D^{*0} is at rest, $\boldsymbol{L_{D^*}}$ is null, hence $\boldsymbol{S_{D^*}} = \boldsymbol{J_{D^*}} = (\boldsymbol{J_B} - \boldsymbol{J_h})$ where the second equality is due to angular momentum conservation.

Since both $\boldsymbol{J_B}$ and $\boldsymbol{J_h}$ are orthogonal to $\boldsymbol{p_B}$, also their combination $\boldsymbol{S_{D^*}}$ is orthogonal to $\boldsymbol{p_B}$. Choosing a z axis parallel to $\boldsymbol{p_B}$ one has $S_z = 0$, which implies that D^* is represented by a state

$$|J = 1, J_z = 0\rangle = |S = 1, S_z = 0\rangle|L = 0, L_z = 0\rangle \tag{5.9}$$

The $D^{*0} \to D^0\pi^0$ decay final state has zero spin $S = 0$, because both π^0 and D^0 are pseudo-scalar mesons, but for angular momentum conservation it has to have angular momentum $L = 1$. Hence, it can be represented as

$$|S = 0, S_z = 0\rangle|L = 1, L_z = 0\rangle \tag{5.10}$$

Since the spin momentum is null, no angular momentum coupling is required and one can state

$$\langle\theta, \phi|J = 1, J_z = 0\rangle = \langle\theta, \phi|L = 1, L_z = 0\rangle|S = 0, S_z = 0\rangle = Y_1^0(\theta, \phi)|S = 0, S_z = 0\rangle \tag{5.11}$$

where θ is the polar angle between a daughter particle and the z-axis and ϕ is the azimuthal angle. This means that the decay amplitude is proportional to $\cos\theta$ and the decay probability distribution is proportional to $\cos^2\theta$.

The case of $V \to VS$ decay with $D^{*0} \to \gamma D^0$ is more complex because the photon has spin-1 and, since it is massless, the polarization $|S = 0, S_z = 0\rangle$ does not exist. However, P-parity conservation in the electro-magnetic decay excludes the contribution of even-L solutions. The parity of D^{*0} is indeed -1, while in the final state the parity is $(-1)^L$ since both D^0 and γ have a negative intrinsic parity eigenvalue. With $L = 1$ one gets

$$|J = 1, J_z = 0\rangle_{L=1} = \frac{1}{\sqrt{2}}|S = 1, S_z = -1\rangle|L = 1, L_z = 1\rangle - \frac{1}{\sqrt{2}}|S = 1, S_z = 1\rangle|L = 1, L_z = -1\rangle \tag{5.12}$$

which, in terms of spherical harmonics can be written as

$$\langle\theta, \phi|J = 1, J_z = 0\rangle \propto \frac{1}{\sqrt{2}}Y_1^1(\theta, \phi)|S = 1, S_z = -1\rangle - \frac{1}{\sqrt{2}}Y_1^{-1}(\theta, \phi)|S = 1, S_z = 1\rangle \tag{5.13}$$

It is therefore easy to state that the decay probability $P(\theta)$ is proportional to $\sin^2\theta$.

The two distributions obtained with well reconstructed PID truth-matched Monte Carlo are given in figure 5.8.

These two distributions are suppressed in the left region, possibly because of the geometrical acceptance of the detector or of some correlation with other cuts, but the expected shapes are

Channel with	B mass range ($\mathrm{MeV/c^2}$)	$(m_{D^{*0}} - m_{D^0})$ range ($\mathrm{MeV/c^2}$)
$D^*0 \to D^0\pi^0$	$5263 \div 5295$	$118 \div 162$
$D^*0 \to D^0\gamma$	$5254 \div 5386$	$110 \div 170$

Table 5.1: Tighter selection cuts applied to the data sample to reproduce the helicity angular distribution shown in figure 5.9

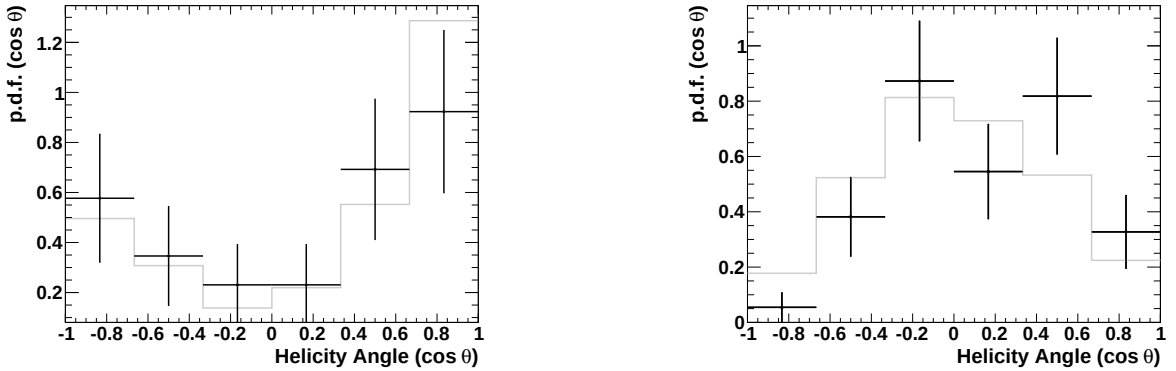

Figure 5.9: Normalized $\cos\theta$ distribution of tightly selected $B^{\pm} \to D^{*0}\pi^{\pm}$ data events for $D^{*0} \to D^0\pi^0$ (left) and $D^{*0} \to D^0\gamma$ (right) channels. D^0 is reconstructed as $D^0 \to K^{\pm}\pi^{\mp}$. The gray solid line represents the MC simulation expectation for the signal only.

qualitatively reproduced. This confirms the expectations and shows that the detector acceptance and the analysis cuts do not affect the distribution in the helicity angle sufficiently to make the selection useless or even harmful.

The same plots for data require tighter selections to improve the purity of the signal, else it is difficult to distinguish the broad structures represented in figure 5.8 over a non-negligible background. The plots have been obtained imposing the selection cuts listed in table 5.1, and corresponding to a ± 16 $\mathrm{MeV/c^2}$ cut on the B meson mass peak. In figure 5.9 the resulting $\cos\theta$ distributions are shown. The black point representing data are superposed to a solid gray line indicating the MC expectation for each bin. The agreement is good for $D^{*0} \to D^0\pi^0$ decays, while for $D^{*0} \to D^0\gamma$ the agreement is less convincing, probably because the its sample is less pure, as it will be discussed below.

To evaluate whether this kinematic variable is really discriminant between the background and the signal, in figure 5.10 the distributions in $|\cos\theta|$ for the samples used to train the Fisher discriminant are shown, it is evident that the discrimination can better rely on this variable for the $D^{*0} \to D^0\pi^0$ than for $D^{*0} \to D^0\gamma$.

It is important to remark that the discriminant variable to be used in the Fisher discriminant can not be simply $\cos\theta$: the absolute value is essential. Indeed the Fisher discriminant algorithm needs to rely on the concept of mean value and of standard deviation of the hypothesis distributions, a double peak distribution is considered by the Fisher algorithm as a single peak structure with a centered mean value and a large standard deviation. The absolute value operation allows to transform the double-peak structure into a single peak distribution, much more useful for a linear algorithm such as a Fisher discriminant. Neural networks and BDTs are not affected by this limitation, but we still do not control sufficiently the whole analysis to adopt such black-box methods.

5.2 Multiple Candidates

The problem of multiple candidates is more important in the analyses including D^{*0} for two reasons. First, there is one more particle involved in the decay, so that the number of possible combinations increases, and - most important - that particle is neutral and detected as low energy photon(s) in

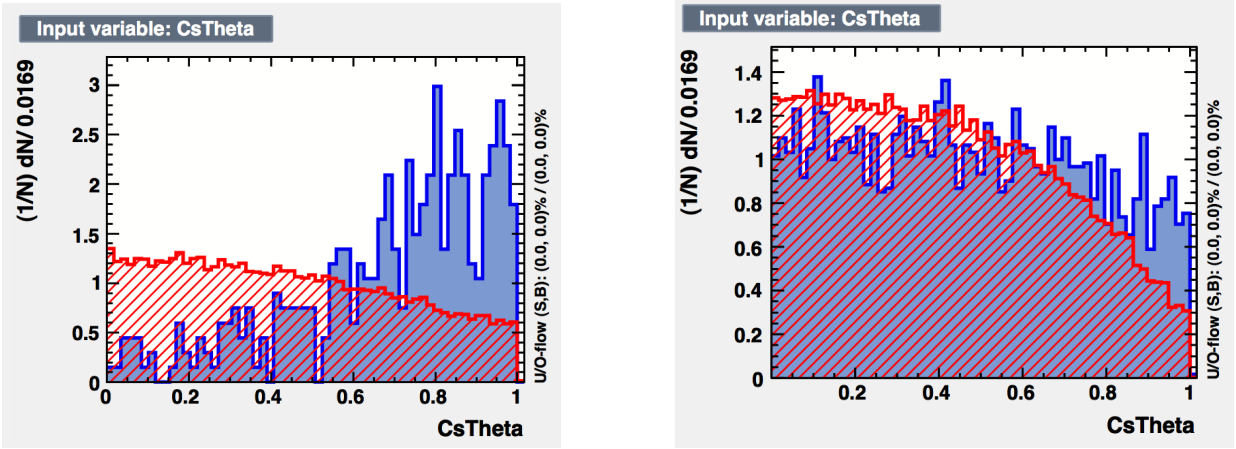

Figure 5.10: Comparison between the distributions in $|\cos\theta|$ for $B^{\pm} \to D^{*0}\pi^{\pm}$ candidate events. The red striped histogram represents background from sidebands while the blue full one is obtained with a MC simulation of $B^{\pm} \to D^{*0}\pi^{\pm}$ decays. It is evident that the difference is much more relevant for the $D^{*0} \to D^0\pi^0$ channel (left) than for $D^{*0} \to D^0\gamma$ (right).

the electromagnetic calorimeter. Because of the high photon rate detected by the ECAL, it is likely to select many photons for the same event, generating more *overlap* candidates. The candidates sharing the three charged tracks, but with a different photon or neutral pion are classified as *neutral overlap*. The classification is reported in table 5.2. If compared to the classification of charged track analysis reported in table 4.3, the D^{*0} channels present, as expected, a much larger number of overlaps. In almost all the cases, this is due to multiple neutral particles giving candidates surviving all the selections.

This kind of multiple candidates is more harmful for the analysis than clones. The difference between the reconstructed B mass for two overlap candidates can be considerably high. The scatter plot for the reconstructed masses of each pair of multiple candidates is shown in figure 5.11. Red dots represent clones, while the black ones are overlap candidates. While the mass correlation is high in clones (they give almost the same B mass), so that it is not really important to choose the better, black points are spread almost randomly on the B mass - B mass plane. This is true for $D^{*0} \to D^0\pi^0$ more than for $D^{*0} \to D^0\gamma$, but even for the latter channel the distribution spread is much higher than that of clones (see figure 4.5).

It should not surprise that the number of multiple events in $D^{*0} \to D^0\pi^0$ channel is much smaller than in $D^{*0} \to D^0\gamma$. Again, this is due to the constraint on the $\gamma\gamma$ invariant mass in the π^0 reconstruction, which sensibly reduces the combinatorial background.

The conclusion about multiple candidates is that, as expected, the problem is more important for channels containing a D^{*0} than for channels containing charged tracks only, described in the previous chapter. More attention has to be payed to the method used to select the best candidate because, besides being more useful since the reconstructed B masses for different neutral overlap candidates are different (as opposed of charged clones, constituting the majority of multiple candidates for $B \to Dh$ channels) it is more difficult. Indeed, while for charged tracks information from many sub detectors is available, for photons (as well as for π^0's), the information comes only from the ECAL, and the momentum direction determination is not as good as for charged tracks. The only other variable characterizing photons is the energy, for which the correlation with the reconstructed mass is evident. The challenge is thus to define a procedure to select the best one among the multiple neutral candidates in a single event, which is not based on the quality of vertex fit, because the determination of the photon or π^0 momentum is not precise enough, nor on the photon energy because any correlation with the B mass distribution should be avoided not to bias the resulting number of events.

Analogous problems in the collaboration have been solved with a random selection of a candidate in any multiple candidate event. This method excludes correlations with any other parameter and can be iterated more times with different random seeds to study the systematic uncertainty on the

$D^0 \to K^\pm\pi^\mp$	$B^\pm \to \pi^\pm D^{*0}(D^0\gamma)$		$B^\pm \to \pi^\pm D^{*0}(D^0\pi^0)$	
	MonteCarlo	Data	MonteCarlo	Data
Events				
Generated or Produced	393×10^3	119×10^3	639×10^3	193×10^3
Selected	2840	1355	1066	365
Multiple Candidates				
Genuines	0	0	0	0
Overlaps	788	297	188	33
of which neutral overlaps	788	297	188	33
Clones	45	1	11	1

Table 5.2: Summary table of multiple candidate classification for D^{*0} analyses. Background is not considered because the total number of sidebands events surviving all the selection is too small to be meaningful. The number of generated MC events is an output of the MC generator. The number of event produced at LHCb is an estimation calculated as $2 \times \sigma \times B_F \times \int \mathcal{L}$, where σ is $b\bar{b}$-production cross section in the LHCb acceptance, known with a 19% uncertainty, B_F is the PDG [24] branching ratio for the considered decay chain and $\int \mathcal{L}$ is the LHCb integrated luminosity. The factor 2 indicates that both b and $\bar{b}$ can contribute to the decay chain.

number of events obtained from the fit.

For this preliminary analysis, the B DIRA parameter has been used to select the best candidate. The B DIRA parameter is defined in the previous chapter as the cosine of the angle between the reconstructed B momentum and the B flight direction, based on the reconstructed position of the primary vertex and of the secondary B decay vertex. In $B^\pm \to D^{*0}\pi^\pm \to (D^0\gamma)\pi^\pm$ decays, this angle is sensitive to the choice of the photon because a change in the photon slightly changes the reconstructed B momentum, and the B DIRA is supposed to approach zero when the best photon is chosen. The correlation between the B mass and the B DIRA parameter is negligible.

Using a Monte Carlo sample, the best photon choice efficiency has been estimated. It is defined as the ratio between the number of multiple candidate events where the right photon has been chosen, and the number of multiple candidate events where one of the selected photons has been tagged by the Monte Carlo as the right one.

The same method is applicable for D^{*0} decays to $D^0\pi^0$ to select the best π^0 when more candidates are present in a single event.

This choice efficiency is $(46 \pm 6)\%$ for channels with D^{*0} decaying to $D^0\pi^0$ and $(60 \pm 4)\%$ for channels with $D^{*0} \to D^0\gamma$. As a comparison, a random selection of the candidate gives a selection efficiency of $\sim 30\%$ for channels with D^{*0} decaying to $D^0\pi^0$ and $\sim 40\%$ for channels with $D^{*0} \to D^0\gamma$. In order to understand this result, it is useful to remind that there is a significant fraction of multiple candidate events with more than two candidates. These efficiencies could probably be improved adding the information on the particle identification, selecting the event whose photon has the highest Particle Identification Confidence Level (PCL), or combining the B DIRA and PCL parameters in a likelihood. However, as mentioned before the PCL parameter has not been included in this preliminary analysis, so that the multiple candidate selection can not rely on it.

5.3 Signal estimation

The invariant mass distribution of data candidates passing all the selections is represented in figure 5.12. The vertical lines indicate the boundaries of the signal box, estimated from MC simulations as a symmetric interval $\pm 3\sigma$ centered on the peak value. The unbinned maximum likelihood fit pdf is composed of a Gaussian to model the signal and of a polynomial pdf to model the background. The polynomial pdf is then used to estimate the expected background in the signal box.

For $D^{*0} \to D^0\gamma$ the total number of events in the signal box is 335, with an expected background of 269 ± 12 events. The signal yield estimated through the fit is

$$S = \text{Yield}(\text{D}^{*0} \to \text{D}^0\gamma) = 62 \pm 21 \tag{5.14}$$

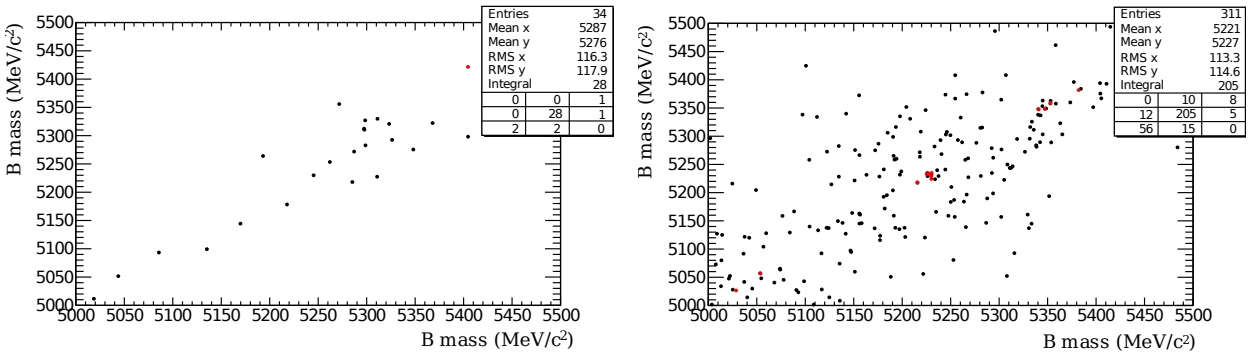

Figure 5.11: Reconstructed B mass for each couple of multiple candidates in $B^{\pm} \to D^{*0}\pi^{\pm}$ data sample (channel with $D^{*0} \to D^0\gamma$ decays at left and with $D^{*0} \to D^0\pi^0$ at right). Red dots are clone candidates, in black the overlaps.

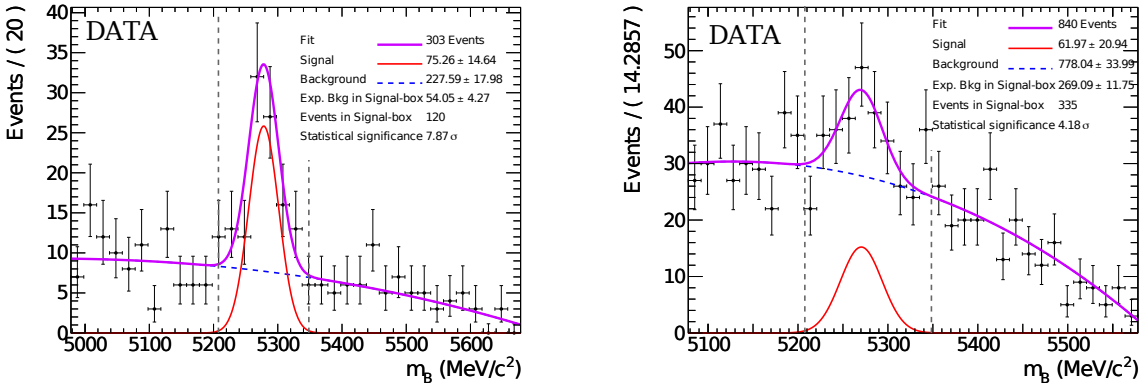

Figure 5.12: Reconstructed B mass distribution for $B^{\pm} \to D^{*0}\ \pi^{\pm}$ candidate events with $D^{*0} \to D^0\pi^0$ (left) and $D^{*0} \to D^0\gamma$ (right), with $D^0 \to K\pi$.

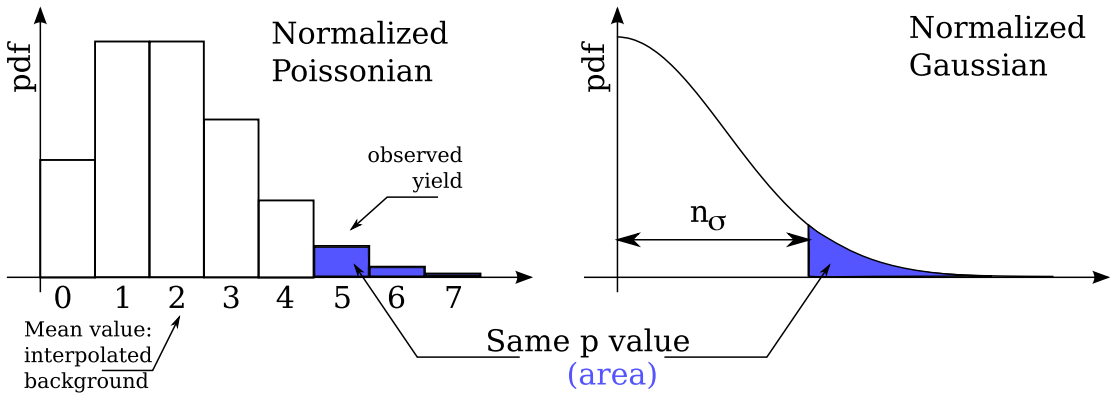

Figure 5.13: Graphical representation of the procedure to estimate the statistical significance of the signal peak.

with a purity of 19%.

For the channel $D^{*0} \to D^0\pi^0$ the signal is more significant, thanks to a better background rejection and to the higher branching ratio. The total number of events in the signal box is 120, with an expected background of 54 ± 5. The number of signal evens estimated through the fit is

$$S = \text{Yield}(\text{D}^{*0} \to \text{D}^0\pi^0) = 75 \pm 15 \tag{5.15}$$

with a purity of 63%.

5.3.1 Statistical significance

The statistical significance of the signal is evaluated using the fit to estimate the expected background. The polynomial function used to model the background is integrated over the signal box to estimate the number of background events expected in the region. Then one considers that if there were no signal, the statistics of this region would follow a Poissonian distribution and the best approximation for the mean value of this Poissonian is given by the expected background yield E_B estimated through the polynomial fit.

Hence, one assumes that the probability of measuring a background yield Y_B is

$$P(Y_B) = e^{-E_B}\,\frac{{E_B}^{Y_B}}{Y_B!} \tag{5.16}$$

The probability of measuring at least the observed event yield Y_S in the signal box, if it were given by a statistical fluctuation of the background, without signal contributions, is called the Poissonian p value

$$p = P(Y_B \geq Y_S) = \sum_{n=Y_S}^{+\infty} e^{-E_B}\frac{{E_B}^n}{n!} \tag{5.17}$$

To express this probability as a statistical separation between the signal and the background in terms of normal distribution standard deviations, one considers the value n_σ that reproduces the same p value in a normalized single-tail Gaussian distribution, with zero mean value and unity standard deviation (figure 5.13). Namely,

$$n_\sigma : \quad \frac{2}{\sqrt{2\pi}}\int_{n_\sigma}^{+\infty} \exp\left(-\frac{x^2}{2}\right)\mathrm{d}x = p \tag{5.18}$$

Defining the complementary error function

$$\text{Erfc}(x) = \frac{2}{\sqrt{\pi}}\int_x^{+\infty} e^{-t^2}\mathrm{d}t \tag{5.19}$$

one can write the statistical separation between the observed yield in the signal box and the expected background as

$$n_\sigma = \sqrt{2}\ \mathrm{Erfc}^{-1}\left(\frac{p}{2}\right) \tag{5.20}$$

where Erfc^{-1} indicates the inverse function of Erfc (*i.e.* $\mathrm{Erfc}[\mathrm{Erfc}^{-1}(x)] = x$) and the factor $1/2$ is due to the single tail Gaussian hypothesis considered in the calculation, while $\sqrt{2}$ appears because the Gaussian distribution used to define the inverse error function has $\sigma^2 = \frac{1}{2}$.

Using the `TMath::ErfcInverse` ROOT [40] method it is easy to calculate the statistical significance, or separation, for $D^{*0} \to D^0\gamma$ and $D^{*0} \to D^0\pi^0$ channels.

The statistical significance of the B decay through $D^{*0} \to D^0\gamma$ is of 4.18 σ, while for the B decay through $D^{*0} \to D^0\pi^0$ it is 7.87 σ.

This means that, in both channels, the probability that the signal is due to a statistical fluctuation is less than 1/10 000; furthermore, considering that the peak is centered on B mass value, where it is expected, the reliability of the observation increases.

5.4 Conclusions on $B^\pm \to D^{*0}\pi^\pm$ channels

The results described in the previous paragraph indicate that the current performances of the LHCb detector and analysis packages are not sufficient to include D^{*0} channels in an ADS analysis.

- In the previous chapter we analysed the suppressed $B^\pm \to D^0_{CP}K^\pm$ decays (the ones used to measure the angle γ), and the favored $B^\pm \to D^0\pi^\pm$ ones. The ratio between suppressed and favored channel yields is expected to be the same in the $B^\pm \to D^{*0}h^\pm$ channels. Namely,

$$\frac{\mathrm{Yield}(B^\pm \to D^{*0}_{CP}K^\pm)_{\mathrm{suppr}}}{\mathrm{Yield}(B^\pm \to D^{*0}\pi^\pm)_{\mathrm{fav}}} \approx \frac{\mathrm{Yield}(B^\pm \to D^0_{CP}K^\pm)_{\mathrm{suppr}}}{\mathrm{Yield}(B^\pm \to D^0\pi^\pm)_{\mathrm{fav}}} \tag{5.21}$$

- In this chapter, we studied favored decays $B^\pm \to D^{*0}\pi^\pm$. The measured yield can be compared to that of favored $B^\pm \to D^0\pi^\pm$ decays studied in chapter 4.2.10. The ratio between the number of selected events is

$$\frac{\mathrm{Yield}(B^\pm \to D^{*0}\pi^\pm)_{\mathrm{fav}}}{\mathrm{Yield}(B^\pm \to D^0\pi^\pm)_{\mathrm{fav}}} \sim \frac{1}{40} \tag{5.22}$$

- In order to collect for the $B^\pm \to D^{*0}h^\pm$ channels the same statistics as the one already collected in 2010 for $B^\pm \to D^0h^\pm$ channels, we need to reach an integrated luminosity forty times higher: 37 $\mathrm{pb}^{-1}\times$ 40 $\approx$ 1.5 fb^{-1}, which is expected for middle 2012. With such a statistics

$$\mathrm{Yield}(B^\pm \to D^{*0}_{CP}K^\pm, 1.5\ \mathrm{fb}^{-1}) \approx \mathrm{Yield}(B^\pm \to D^0_{CP}K^\pm, 37\ \mathrm{pb}^{-1}) \tag{5.23}$$

  the latter yield corresponds to the plots shown in figure 4.12. Even with the larger statistics expected for the end of 2012, before the technical stop foreseen in 2013, the statistical significance of the signal is not sufficient to achieve a precise measurement of γ.

In table 5.3 these considerations are supported by figures. Based on the measured yield ratios, the expected number of selected events for suppressed D^{*0} channels is estimated. The ratio between integrated luminosities is exploited to estimate the expected yields at the end of 2012, before the one-year long technical stop. An expected yield of 30 events will not be sufficient to measure a GLW asymmetry with useful statistical significance. The 2 fb^{-1} integrated luminosity expected for the end of 2012 won't be sufficient to achieve any ADS measurement using D^{*0} channels, for which an even smaller statistics is expected as the relevant branching ratio is about an order of magnitude lower.

Even if the results are not encouraging, there are a few opportunities to improve the reconstruction efficiency which will be studied by the collaboration. Besides an effort in calorimetry which

	LHCb — 37 pb^{-1} (2010)			**LHCb — 2 fb^{-1} (2012)**		
	N_{RS} $(D\pi)$	$N_{RS}(DK)$	N_{CP+}	N_{RS} $(D\pi)$	N_{RS} (DK)	N_{CP+}
D^0	**5091**	**422**	**46**	275k	23k	2484
$D^{*0} \to D^0\gamma$	**62**	5.1	0.6	3348	275	32.4
$D^{*0} \to D^0\pi^0$	**75**	6.3	0.7	4050	340	37.8

Table 5.3: Summary of the yields obtained in the analysis (bold) and extrapolated to most suppressed channels (not observed in the present 37 pb^{-1}data sample) and to the total statistics expected before the technical stop in 2013. The expected yield for D^{*0} channels is not sufficient to contribute significantly to the γ measurement.

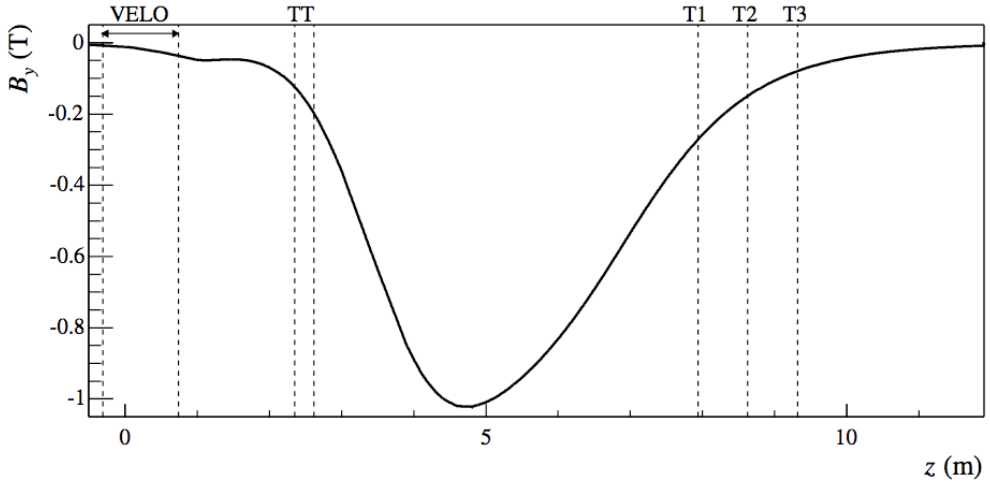

Figure 5.14: Magnetic field as a function of the distance from the interaction point. The tracking detectors positions are shown.

could improve significantly the reconstruction efficiency of low energy photons, alternative techniques can be explored. Currently a promising one is the study of low energy photons converting in the tracking material. In figure 5.14 the magnetic field as a function of the distance from the interaction point z is shown. The conversion in VELO and Trigger Traker are useless for the study of low-energy photons, because the low energy electron and positron produced in the conversion would be ejected from the geometrical acceptance by the strong magnetic field in the magnet region. However, for conversions in T1, T2, and even in T3 with improvements in the software, the low momentum of the produced leptons can allow to obtain separated tracks with the weak bending power of the magnetic field in that region. This study could allow to add an important statistics in particular for the $D^{*0} \to D^0\gamma$ decays. For $D^{*0} \to D^0\pi^0$ decays it would be necessary to combine photons in the calorimeter and photons detected as e^+e^- pairs produced in the tracking system. This combination requires a major effort and will be faced only if the technique gives good results with the $D^{*0} \to D^0\gamma$ channel analysis.

An effort in the low-energy reconstruction efficiency of the ECAL would also be useful for other analyses, from the GGSZ Dalitz plot analysis, to add the $B^\pm \to D^0K^\pm$ channel with $D^0 \to K\pi\pi^0$, to the charm physics program of LHCb.

Conclusion

Among the three angles of the CKM-unitarity triangle, γ remains the least experimentally constrained. The world average for this CP-violating parameter is $\left(71^{+21}_{-25}\right)^{\circ}$, if one only considers direct measurements. A precise measurement of this angle is one the of main aims of the LHCb experiment at CERN, indeed there are two reasons which made it desirable. The first one is that γ is one of the eighteen (twenty-one considering massive neutrinos) arbitrary parameters of the Standard Model; the second, more important, is that the angle γ can be measured via both tree- and loop-level b-decays. While the latter are sensitive to possible New Physics (NP) contributions, tree-level processes are considered to be immune. A comparison between the measured value for γ achieved with these two types of decays allows to test the CKM mechanism, looking for NP.

There are a few different techniques to measure γ using tree-only b-decays. The most promising ones at LHCb are the GLW and ADS methods, called after the authors of the original papers, Gronau-London-Wyler and Atwood-Dunietz-Soni, respectively. These two methods search for $B^{\pm} \to \overset{(-)}{D}{}^0 K^{\pm}$ decays with D^0 and $\bar{D}^0$ decaying to a common final state. The measurement of γ relies on the interference between the two decay chains. The GLW method exploits D decays to CP eigenstates: K^+K^- and $\pi^+\pi^-$ are typical CP-even eigenstates and have been considered at LHCb. CP-odd eigenstates will be (perhaps) considered in future, since they are more difficult to reconstruct at hadronic machines. The ADS methods relies on "Wrong Sign", Doubly Cabibbo Suppressed $B^{\pm} \to \overset{(-)}{D}{}^0 K^{\pm} \to (\pi^{\pm}K^{\mp})K^{\pm}$ decays.

The preliminary analyses, relayed in this thesis, are based on the 2010 LHCb data set, with an integrated luminosity of 37 pb^{-1}. This data set is considered to be too small to observe ADS-related decays, so that only the GLW method has been exploited. Hence the following decay chains have been reconstructed:

- $B^{\pm} \to \overset{(-)}{D}{}^0 K^{\pm} \to (K^+K^-)K^{\pm}$ and $B^{\pm} \to \overset{(-)}{D}{}^0 K^{\pm} \to (\pi^+\pi^-)K^{\pm}$, because from the interference between D^0 and $\bar{D}^0$ channels it is possible to extract γ.

- $B^{\pm} \to \overset{(-)}{D}{}^0 \pi^{\pm} \to (K^+K^-)\pi^{\pm}$ and $B^{\pm} \to \overset{(-)}{D}{}^0 \pi^{\pm} \to (\pi^+\pi^-)\pi^{\pm}$, called the normalization channels, which are useful to study systematics and analysis techniques. Indeed, while the branching ratio is much higher, which means much more statistics, the analysis of these channels is very similar to that for signal channels. Only the Particle Identification (PID) selection for the charged meson from the B decay is different.

- $B^{\pm} \to \overset{(-)}{D}{}^0 h^{\pm} \to (K^{\pm}\pi^{\mp})h^{\pm}$, where h can be a pion or a kaon, called "Right Sign" events, which are Cabibbo Favored and constitute the brighter source of $B^{\pm} \to D^0 h^{\pm}$ with $D^0 \to h^{\pm}h^{\mp}$ decays, so that they are useful to study efficiencies and to test analysis programs.

I have repeated the official analysis of LHCb obtaining consistent values for the event yields, then I have used the same software utilities and the acquired knowledge to face a preliminary study of $B^{\pm} \to \overset{(-)}{D}{}^{*0} h^{\pm}$ channels. These channels have contributed to the measurement of γ at the b-factories with about a half of the statistics; furthermore, analyzing $B \to Dh$ channels, one observes that $B^{\pm} \to \overset{(-)}{D}{}^{*0} h^{\pm}$ decays constitute an important background, meaning that in the same data sample containing $B^{\pm} \to \overset{(-)}{D}{}^0 h^{\pm}$ there are $B^{\pm} \to \overset{(-)}{D}{}^{*0} h^{\pm}$, too. However, the calorimetric efficiency for the reconstruction of low-energy photons involved in $\overset{(-)}{D}{}^{*0} \to \overset{(-)}{D}{}^0 \gamma$ and $\overset{(-)}{D}{}^0 \pi^0$ decays is sufficiently low to make the measurement challenging.

The original contribution of this work is the analysis of the Cabibbo Favored decays

$$B^{\pm} \to \overset{(-)}{D}{}^{*0} h^{\pm} \to (\overset{(-)}{D}{}^{0}\gamma) h^{\pm} \quad \text{and} \quad B^{\pm} \to \overset{(-)}{D}{}^{*0} h^{\pm} \to (\overset{(-)}{D}{}^{0}\pi^{0}) h^{\pm}\,, \tag{5.24}$$

with $\overset{(-)}{D}{}^{0} \to K^{\pm}\pi^{\mp}$, to compare them with the $B^{\pm} \to \overset{(-)}{D}{}^{0}\pi^{\pm}$ Cabibbo Favored decays, and to enquire whether D^{*0} channels can significantly contribute to the measurement of γ at LHCb, or not.

The measured yields for $B^{\pm} \to \overset{(-)}{D}{}^{*0}\pi^{\pm} \to (\overset{(-)}{D}{}^{0}X)\pi^{\pm}$ and $\overset{(-)}{D}{}^{0} \to K^{\pm}\pi^{\pm}$ channels are:

- for $\overset{(-)}{D}{}^{*0} \to D^{0}\gamma$, 62 ± 21 events, with a statistical significance of 4.18 σ;
- for $\overset{(-)}{D}{}^{*0} \to D^{0}\pi^{0}$, 75 ± 15 events, with a statistical significance of 7.87 σ.

These values can be used to extrapolate the yields expected before the LHC technical stop in 2013, as reported in table 5.3. The extrapolated values are too small to have $B^{\pm} \to \overset{(-)}{D}{}^{*0}K^{\pm}$ channels significantly contributing to the measurement of γ. However, the first measurement of $B^{\pm} \to \overset{(-)}{D}{}^{*0}\pi^{\pm}$ channels and the observation of the partially reconstructed channel as background for $B^{\pm} \to D^{0}\pi^{\pm}$ channels (see figure 4.10) is a first step towards a search of alternative analysis techniques, or calorimetric efficiency enhancement, which could make this channel really useful. Possible improvements are:

- a fine work on Electromagnetic calorimeter reconstruction software to enhance the reconstruction efficiency of low energy photons, which are of marginal interest for most of the studies performed by the LHCb collaboration.
- Using low energy photon conversion $\gamma \to e^{+}e^{-}$ in the tracking system. The high efficiency in the charged tracks reconstruction can balance the low probability for a conversion.
- An improved fit of the low mass region in the reconstructed $B^{\pm} \to \overset{(-)}{D}{}^{0}h^{\pm}$ mass distribution to extract the pdf component due to $B^{\pm} \to \overset{(-)}{D}{}^{*0}h^{\pm}$ channels. Even if the event yields obtained with this technique are one or two orders of magnitude higher than those obtained with fully reconstructed $B^{\pm} \to \overset{(-)}{D}{}^{*0}h$ events, the important role of Monte Carlo simulation in the fit has discouraged studies in this direction in the past, and even today major improvements in the accuracy of Monte Carlo simulation would be required to undertake this way.

Acknowledgements

There are many people that have offered an indispensable help in this work of thesis, and much more if one considers the five-year pathway that this thesis is concluding. I want to start with my advisor Andrea Bizzeti, not only for the patient and careful work during this document redaction, and before during the training period at LAPP, but also for his care in my education and training since when we have met, three years ago, for a small exercise on nuclear α decays. Anna Franchini, president of the Physics course in Modena, has to be acknowledged and thanked for the hard work she has done and the excellent results she is keeping to achieve in the five-year organization, listening to each student requirement, need or gripe and becoming the reference point of anybody in the Physics department. Among the students, I want to thank Krivjo Xheka, Marco Medici, Alberto Spagni, Daniele Pinotti, Ilaria Valenti and Andrea Beggi which shared with me most of the lectures, but also Elena Cipressi, Francesca Gherpelli, Mirko Franchini, Caludia Benedetti, Giulio Guzzinati, Andrea Cappelli and Gianluca Santoni who "living" in the Physics department have shared with me many afternoons and adventures... It is also thank to Gianluca that I have spent the fifth year in France, in Grenoble before, and then in Annecy. From the French experience I want to cite Élodie Tiouchichine and Ivo Naranjo, a sort of new family, sharing with me too many evenings studying Quantum Field Theory or cooking, or - more often - both.

Getting back to this thesis, I want to thank Vincent Tisserand, Marie Noëlle and Daniel Decamp for the patient help offered during my training period in Annecy. Aurélien Barrau, responsible for the French Master, has been a reference point for the whole year. Even if his aims and strategies are often difficult to interpret, it is thank to him that almost anybody attending his master has obtained the scholarship he hoped to.

To my family, and in particular to my brothers Fabio and Biagio, I have dedicated this thesis.

Bibliography

[1] Nicola Cabibbo, Phys. Rev. Lett. **10**, 531 (1963)

[2] M. Kobayashi and T. Maskawa, Prog. Th. Phys. **49**, 652 (1973)

[3] J. Zupan, arXiv:hep-ph/1101.0134v1 (2010)

[4] M. Gronau and D. London, Phys. Lett. B **253**, 483 (1991); M. Gronau and D. Wyler, Phys. Lett. B **265**, 172 (1991).

[5] D.Atwood, I.Dunietz and A. Soni, Phys. Rev. Lett. **78**, 3257 (1997) and Phys. Rev. D **63** 036005 (2001).

[6] C.S. Wu *et al.*, Phys. Rev. **105**, 1413 (1957)

[7] J.H. Christenson *et al*, Phys. Rev. Lett. **13**, 138 (1964)

[8] K. Abe *et al.* (Belle Collaboration), Phys. Rev. Lett. **86**, 2509 (2001)

[9] P. del Amo Sanchez *et al.* (Babar Collaboration), Phys. Rev. Lett. **86**, 2515 (2001)

[10] A. Angelopoulos et al. (CPLEAR collaboration), Phys. Lett. B **444**, 43 (1998).

[11] J. Charles *et al.* (CKMfitter group), Eur. Phys. J. **C 41** 1-131 (2005).

[12] A.A. Alves Jr. *et al* (LHCb Collaboration), JINST **3**, S08005 (2008) – `http://iopscience.iop.org/1748-022`

[13] K. Abe *et al.* (Belle Collaboration), Phys. Rev. D73:051106 (2006)

[14] P. del Amo Sanchez *et al.* (Babar Collaboration), Phys. Rev. D **82**, 072004 (2010)

[15] T. Aaltonen *et al.* (CDF Collaboration), Phys. Rev. D **81**, 031105 (2010).

[16] Y. Hoiri *et al.* (Belle Collaboration), arXiv:1103.5951v2

[17] P. del amo Sanchez, *et al.* (Babar Collaboration), Phys. Rev. D **82**, 072006 (2010)

[18] Paola Squillacioti for the CDF collaboration, *Tevatron time-integrated γ measurement and prospects.* Talk at CKM2010, September, 6th-10th, 2010. arXiv:hep-ex/1012.1781v1

[19] Heavy Flavor Averaging Group (HFAG) – `http://www.slac.stanford.edu/xorg/hfag/`

[20] Kyle S. Cranmer, arXiv:hep-ex/0011057v1.

[21] Wouter Verkerke, David Kirkby, arXiv:physics/0306116v1.

[22] A. Giri, Yu. Grossman, A. Soffer and J. Zupan, Phys. Rev. D **68**, 054018 (2003).

[23] Michael Klasen, Mécanique Quantique Relativiste - Théories de Jauge, Dunod, Paris (2009)

[24] K. Nakamura et al. (Particle Data Group), J. Phys. G **37**, 075021 (2010)

[25] CKM Fitter – http://ckmfitter.in2p3.fr/

[26] L.Wolfenstein, Phys. Rev. Lett. **51**, 1945 (1983); L.L. Chau and W. Y. Keung, Phys. Rev. Lett. **53**, 1802 (1984); B. Winsetein and L. Wolfenstein, Rev. Mod. Phys. **65**, 1113 (1993); A.J. Buras, M.E. Lautenbacher, G. Ostermaier, Phys. Rev. D **50**, 3433 (1994); K. Anikeev *et al.*, arXiv:hep-ph/0201071 (2002).

[27] UTFit – http://www.utfit.org/UTfit/

[28] Glennys R. Farrar, M. E. Shaposhnikov, Phys. Rev. D, **50 (2)**, 774 (1994)

[29] R. Aaij *et al* (LHCb collaboration) - LHCb-PUB-2009-029

[30] Gustavo Castelo Branco, Luis Lavoura, Joao Paulo Silva, CP Violation, Clarendon Press, Oxford (1999).

[31] M. Gronau, Phys. Lett. B 557, 198 (2003)

[32] Asner *et al.*, Fit results for D^0-$\bar{D}^0$ mixing
`http://www.slac.stanford.edu/xorg/hfag/charm/CHARM10/results_mix+cpv.html`

[33] A. Bondar and T. Gershon, Phys. Rev. D **70**, 091503 (2004).

[34] R. Aaij *et al* (LHCb collaboration),Phys, Lett. B **694**, 209 (2010).

[35] D. Asner *et al.*, arXiv:1010.1589

[36] J. Nardulli *et al.*, LHCb-INT-2010-041

[37] Worldwide LHC Computing Grid – http://lcg.web.cern.ch/lcg/

[38] P. Koppenburg, LHCb-INT-2011-009

[39] Matt Needham, LHCb-2008-002, 2008.

[40] CERN ROOT libraries – http://cern.ch/root

[41] J.T. Mościcki *et al.*, arXiv:0902.2685v1

Appendix A

Appendix – MonteCarlo Validation

Comparison between the normalised probability density functions between Monte Carlo simulation (red solid line) and data (blue points).

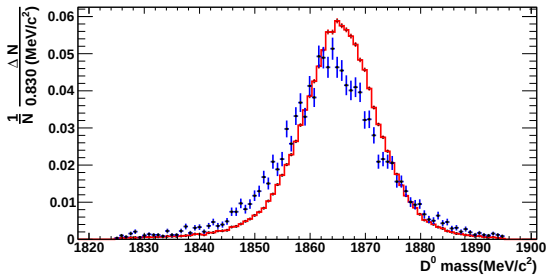

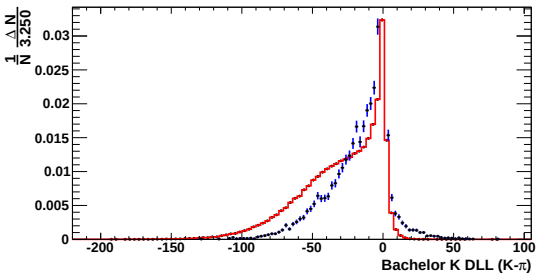

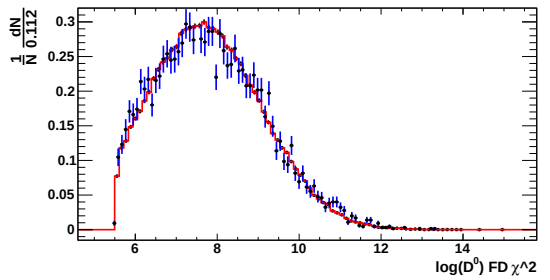

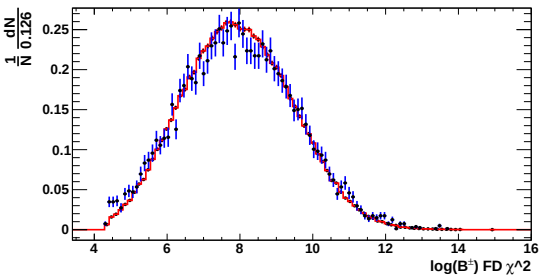

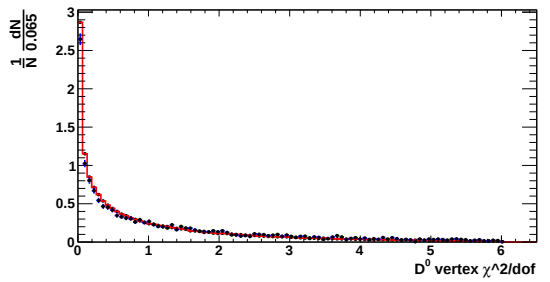

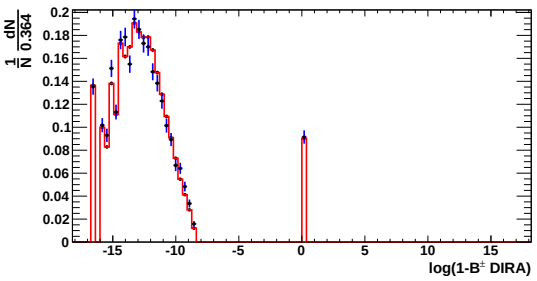

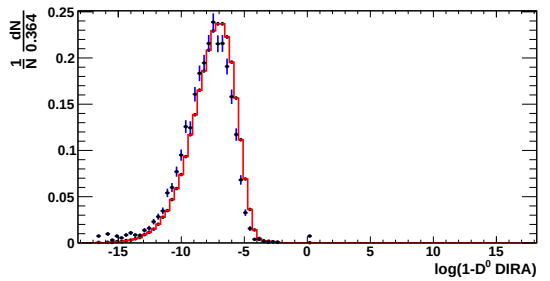

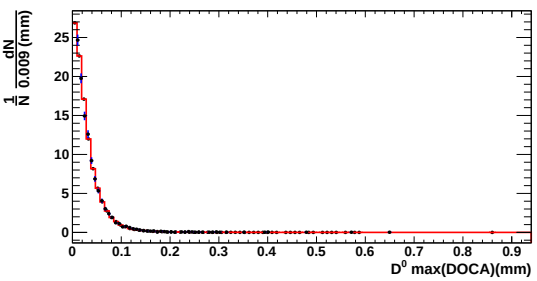

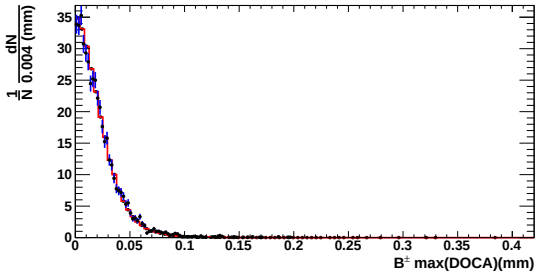
$\frac{1}{N}\frac{dN}{0.004\ (mm)}$
$B^{\pm}$ max(DOCA)(mm)

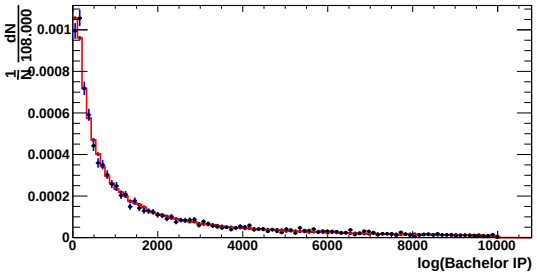
$\frac{1}{N}\frac{dN}{108.000}$
log(Bachelor IP)

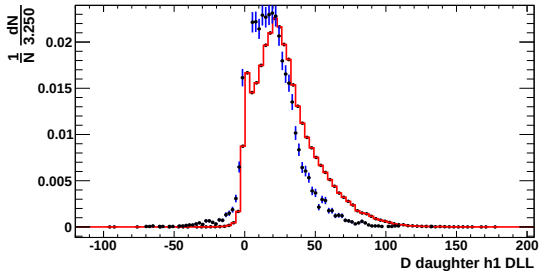
$\frac{1}{N}\frac{dN}{3.250}$
D daughter h1 DLL

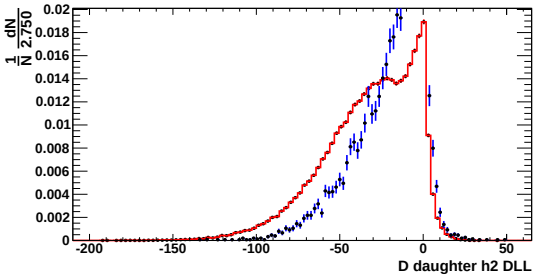
$\frac{1}{N}\frac{dN}{2.750}$
D daughter h2 DLL

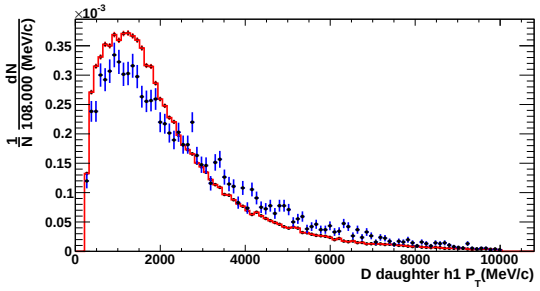
$\times 10^{-3}$
$\frac{1}{N}\frac{dN}{108.000\ (MeV/c)}$
D daughter h1 P_T(MeV/c)

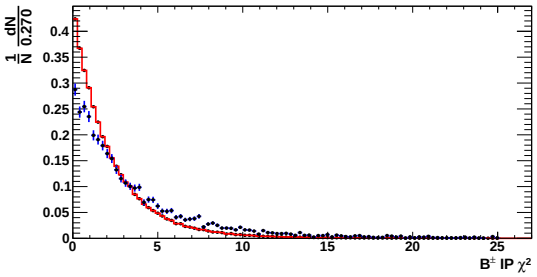
$\frac{1}{N}\frac{dN}{0.270}$
$B^{\pm}$ IP χ^2

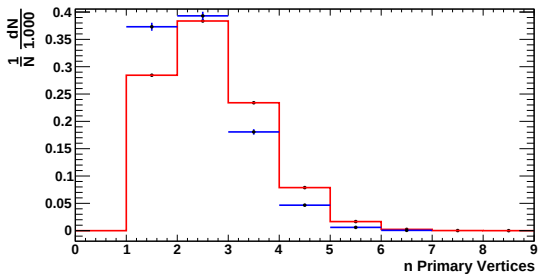
$\frac{1}{N}\frac{dN}{1.000}$
n Primary Vertices

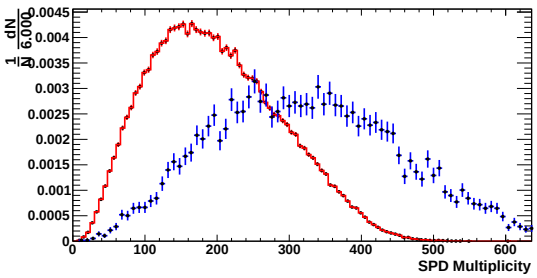
$\frac{1}{N}\frac{dN}{6.000}$
SPD Multiplicity

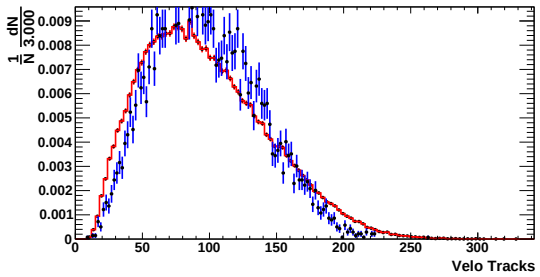
$\frac{1}{N}\frac{dN}{3.000}$
Velo Tracks

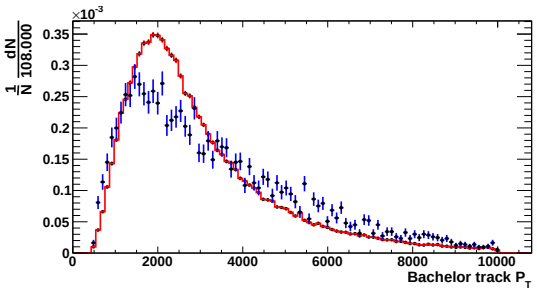
$\times 10^{-3}$
$\frac{1}{N}\frac{dN}{108.000}$
Bachelor track P_T

Appendix B

Appendix – Leaf End-user Analysis Framework (LEAF)

Leaf is a framework currently used to implement analyses of charmed B decay channels, but easily extensible for other kinds of analysis. It provides two complementary ways to implement the analysis: option input files and open classes which can be modified to add algorithms or to define the fit process. The idea is to provide a single stable executable package which can be run for different analyses according to the configuration (or option) file passed as argument. This architecture is particularly useful to run the program in parallel sessions with job managers such as ganga [41], which also provides easy access to the LCG [37].

The option files. Option or configuration input files are XML files which contains:

- The Document Type Definition (DTD), a summary of all the tags usable in the XML structure. The DTD is normally optional in XML, but since constancy check trig almost the totality of errors in options file writing, leaf requires any XML option file to begin with a DTD section.
- The path for input data files, *i.e.* root files containing data ranged in root trees.
- The name and path of the tree inside the root file structure
- The output data file path and filename. The output file includes a root tree with the final data sample and some customized variables to apply final studies of correlation and special fits.
- The list of selections to apply. Selections can be applied to trees selections or to the so called *leaf variables*, user defined algorithms, written in C++ and compiled with the framework. There are two categories of cuts: preselections and selections. The former is intended to make trivial selection which are not in study, as for example to select the mass hypothesis of the particles or to impose the Monte Carlo truth-match conditions. The latter are the selections to study. It is also possible to speed up the program defining the option JUSTFILLOUTPUTREE, which treats all the selections as preselections.

  The selections have to be specified in a very rudimental form:

  $$\texttt{VARIABLE} \quad \{<, >, ==, <=, >=\} \quad \text{value} \tag{B.1}$$

  No additional function (such as absolute values, algebraic operations, square roots, ...) is available. More conditions can be chained is a single condition using $**$ and $++$ tokens, as `AND` and `OR` operators, respectively.
- The histograms to show. Many histograms for each selection can be shown and saved in the output file. Histogram are classified according to the plot variable, the selection and the *level*. If the declared variable to plot is `CUT_VARIABLE`, the current cut variable is plot. The level is an integer number between 0 and 5 establishing when the histogram is filled.

- Level 0 – The histogram contains all the events coherent with the current analysis (as defined in the PRESELECTION section of the input file)
- Level 1 – The histogram contains all the events surviving all the selection but the one in analysis.
- Level 2 – The histogram contains all the events surviving the current selection.
- Level 3 – The histogram contains all the events surviving all the selections.
- Level 4 – The histogram contains all the events surviving all the selections defined in option file before the current one.
- Level 5 – The histogram contains all the events at level 4 selection, surviving the current analysis.

Histograms are stored in the output root files to make easy to retrieving and plotting them properly. To make human-friendly to read them, they are also ranged in a html file saved in the output directory.

- The path for a html output log, reporting the efficiencies associated to each cut.
- The fit function(s) to apply to the final sample. Fit functions are user-defined functions identified by a string, which can be used in the option file to recall them.

An example of a option file is given in the following pages.

```
<?xml version="1.0" encoding="UTF-8"?>
<!-- This is the configuration file for LEAF End-user Analysis Framework-->
<!DOCTYPE LEAF[
 <!ELEMENT LEAF (ANALYSISNAME, EVENTLIMIT?, FINALIZEONLY?, JUSTFILLOUTPUTTREE?, INPUT, CUTOUTPUT,
          OUTPUTDIRECTORY, TREESTRUCTURE , SELECTIONSHISTOGRAMS, ANALYSISSELECTION,
            SELECTIONS, EFFICIENCY, FITTER)>
<!ELEMENT INPUT (FILE+)>
<!ELEMENT FILE (#PCDATA)>
<!ELEMENT CUTOUTPUT (FILE, OUTPUTVARIABLE*)>
<!ELEMENT SELECTIONSHISTOGRAMS (HISTOGRAM+)>
<!ELEMENT HISTOGRAM ( (LEAFVARIABLE? , INTEGERS?, VARIABLENAME, MIN?,MAX?,NBIN?, XAXIS?, YAXIS?, XLABEL?,
          LEVEL+ ))>
<!ELEMENT OUTPUTVARIABLE (INTEGERS?, VARIABLENAME)>
<!ELEMENT VARIABLENAME (#PCDATA)>
<!ELEMENT MIN (#PCDATA)>
<!ELEMENT MAX (#PCDATA)>
<!ELEMENT NBIN (#PCDATA)>
<!ELEMENT XAXIS (#PCDATA)>
<!ELEMENT YAXIS (#PCDATA)>
<!ELEMENT LEVEL (#PCDATA)>
<!ELEMENT SELECTIONS (CUT+)>
<!ELEMENT ANALYSISSELECTION (CUT+)>
<!ELEMENT CUT (INTEGERS?, LEAFVARIABLE?, CONDITION, MIN?, MAX?, NBIN?, XAXIS?, YAXIS?)>
<!ELEMENT CONDITION (#PCDATA)>
<!ELEMENT EFFICIENCY (FILE, COMMENTS)>
<!ELEMENT COMMENTS (#PCDATA)>
<!ELEMENT FITTER (FITFUNCTION*)>
<!ELEMENT FITFUNCTION (ARGS, NAME)>
<!ELEMENT ARGS (#PCDATA)>
<!ELEMENT NAME (#PCDATA)>
<!ELEMENT OUTPUTDIRECTORY (#PCDATA)>
<!ELEMENT TREESTRUCTURE (#PCDATA)>
<!ELEMENT EVENTLIMIT (#PCDATA)>
<!ELEMENT INTEGERS EMPTY>
<!ELEMENT FINALIZEONLY EMPTY>
<!ELEMENT JUSTFILLOUTPUTTREE EMPTY>
<!ELEMENT LEAFVARIABLE EMPTY>
<!ELEMENT ANALYSISNAME (#PCDATA)>
<!ELEMENT XLABEL (#PCDATA)>
]>

<LEAF>
<!-- The name of the analysis used to title the html page-->
        <ANALYSISNAME>B2DKpipi/data</ANALYSISNAME>

<!-- Flag indicating that a quick execution is required without plotting-->
        <JUSTFILLOUTPUTTREE/>
<!-- Event limit set to 50000 preselected events -->
        <EVENTLIMIT>50000</EVENTLIMIT>
<!-- Finalization only can be used to calculate efficiencies and to apply the fit starting from the output file.
        It is useful to refine fit functions -->
<!--    <FINALIZEONLY/> -->

<!-- List of the input files -->
        <INPUT>
                <FILE>/path/to/file1.root</FILE>
                <FILE>/path/to/file2.root</FILE>
<!--             ...     -->
        </INPUT>

        <CUTOUTPUT>
<!--    Output root file -->
                <FILE>/lapp_data/lhcb/anderlini/Analysis/leaf/v10/B2DKpipi/B2DKpipi-data.root</FILE>

<!-- Variables to add to the output tree, the reconstructed B and D masses are automatically added  -->
                <OUTPUTVARIABLE>
                        <INTEGERS/>
                                <!-- integers means that the variable is an integer, by default it is a float.-->
                        <VARIABLENAME>h1_D_TRACK_Key</VARIABLENAME>
                </OUTPUTVARIABLE>
                <OUTPUTVARIABLE>
                        <INTEGERS/>
                        <VARIABLENAME>h2_D_TRACK_Key</VARIABLENAME>
                </OUTPUTVARIABLE>
                <OUTPUTVARIABLE>
                        <INTEGERS/>
                        <VARIABLENAME>h3bach_TRACK_Key</VARIABLENAME>
                </OUTPUTVARIABLE>
        </CUTOUTPUT>
<!-- Output directory where histogram files are placed. -->
        <OUTPUTDIRECTORY>/path/to/a/directory/</OUTPUTDIRECTORY>

<!-- Path to the tree in the input file -->
        <TREESTRUCTURE>TDir_B2Dh3_h1h2/B2Dh3_h1h2</TREESTRUCTURE>

        <SELECTIONSHISTOGRAMS>
                <HISTOGRAM>
                        <VARIABLENAME>Bu_MM</VARIABLENAME>
                        <MIN>5100</MIN><MAX>5830</MAX><NBIN>60</NBIN>
                        <XAXIS>Mass of B^{#pm}</XAXIS>\
                        <YAXIS>Events / (11.8 MeV/c^{2})</YAXIS>
        <!-- Histogram levels to plot superposed -->
                        <LEVEL>0</LEVEL>
                        <LEVEL>2</LEVEL>
                </HISTOGRAM>
                <HISTOGRAM>
                        <VARIABLENAME>Bu_MM</VARIABLENAME>
                        <MIN>5100</MIN><MAX>5830</MAX><NBIN>60</NBIN>
                        <XAXIS>Mass of B^{#pm}</XAXIS>
                        <YAXIS>Events / (11.8 MeV/c^{2})</YAXIS>
                        <LEVEL>1</LEVEL>
                        <LEVEL>3</LEVEL>
                </HISTOGRAM>
```

```
<!--                          ...      -->
        </SELECTIONSHISTOGRAMS>

        <!-- Preselection -->
        <ANALYSISSELECTION>
                <CUT>
                        <LEAFVARIABLE/> <!-- This identifies the variable as a user defined leaf variable -->
                        <CONDITION>LEAF_SELECTANALYSIS == 13.</CONDITION>
        <!-- in this case in verfies the mass hypothesis for an analysis called 13 -->
                </CUT>
        </ANALYSISSELECTION>

        <!-- Selection -->
        <SELECTIONS>
                <CUT>
                        <CONDITION>h1_D_PT > 330. ** h2_D_PT > 330. </CONDITION>
                        <MIN>0</MIN><MAX>1000</MAX><NBIN>100</NBIN>
                        <XAXIS>D^{0} bachelor p_{T} (MeV)</XAXIS>
                        <YAXIS>Events </YAXIS>
                </CUT>
<!--             ...                 -->
        </SELECTIONS>

<!-- Efficiency output file and caption of the output table-->
        <EFFICIENCY>
                <FILE>efficiencies.html</FILE>
                <COMMENTS>Efficiency calculated in certain conditions</COMMENTS>
        </EFFICIENCY>

<!-- Fitter function definition -->
        <FITTER>
                <FITFUNCTION>
                        <NAME>Some_func_ID</NAME>
                        <ARGS>A string passed to the function, containing parameters or whatever else</ARGS>
        </FITTER>
</LEAF>
```